ABSTRACT

Title of Dissertation : **ACTIVE MICRORING AND MICRODISK OPTICAL RESONATORS ON INDIUM PHOSPHIDE**

Kuldeep Amarnath

Doctor of Philosophy, 2006

Dissertation Directed By: **Professor Ping-Tong Ho**

Electrical and Computer Engineering

Photonic or optical logic holds the promise of ultra-fast logic circuits with capability for speeds beyond what is possible using conventional silicon electronics. However, the jump from theory to practice has a high barrier set by critical issues such as integration, scalability and power requirements. Optical micro-resonator based schemes have the potential of addressing some of these issues. This thesis focuses on the development of active InGaAsP/InP microdisk and microring optical resonators to lower that barrier a little.

Microrings and disks provide a compact and cascadable device platform to achieve resonance enhancement of optical non-linearity. By incorporating gain in such devices, the optical power needed for carrying out switching can be greatly reduced. Electrically pumped microring and microdisk resonators are fabricated on indium phosphide in both vertically and laterally coupled bus-waveguide configurations. The gain saturation non-linearity is used to demonstrate all-optical switching and bistable operation at optical powers more than two orders of magnitude lower compared to passive devices. The shift in the ring/disk resonances caused by the refractive index change due to a pump beam is used to switch a weaker probe beam tuned to one of the resonances. The non-linear response and switching mechanism is modeled numerically. A novel pseudodisk configuration that combines the best of microdisks and microrings is used to minimize device heating and surface recombination as well as provide near single-mode operation.

Additionally, optical amplifiers based on microrings are also developed for cascading passive optical gates. Optical amplification up to 10 db in pulsed mode has been observed for 20 μm radius microrings.

The control of surface recombination on the microring sidewalls is critical to avoid carrier loss and device heating. A sulfur passivation scheme is used to reduce the surface recombination velocity. The lateral carrier transport and surface recombination in microrings is analyzed by an ambipolar diffusion model.

ACTIVE MICRORING AND MICRODISK OPTICAL RESONATORS ON INDIUM PHOSPHIDE

By

Kuldeep Amarnath

Dissertation submitted to the Faculty of the Graduate School of the
University of Maryland, College Park, in partial fulfillment
of the requirements for the degree of
Doctor of Philosophy
2006

Advisory Committee:

Professor Ping-Tong Ho, Chair
Professor Julius Goldhar
Professor Christopher Davis
Professor Mario Dagenais
Professor Wendell T. Hill III
Dr. Kenneth J. Ritter

DEDICATION

To my parents N. Amarnath and M. Yamuna

and to Ranjani

for their love, patience and encouragement.

ACKNOWLEDGEMENTS

I owe the most gratitude to my advisor, Prof. Ping-Tong Ho, who has been a very patient and encouraging teacher during the course of my research. His keen insight and experience in optical devices has helped me avoid many a pitfall.

I am equally grateful to Prof. Julius Goldhar for the many stimulating discussions that have uplifted me from my gloom after endless hours in the clean-room and seemingly insurmountable challenges. I have always looked forward to his candor and humor filled take on research.

I would also like to thank members of the LPS staff, many of whom have been extremely helpful and instrumental in the completion of this thesis. I am grateful to Dr. Chris Richardson for the many useful discussions, Dr. S. Kanakaraju for the epitaxial growth and Dr. Tie-Nan Ding for help with simulations.

I am also very grateful to the clean-room staff: Toby Olver, Steve Brown, Lisa Lucas and Sal Martinez, whose support went a long way in my processing experience. I will miss the wit and banter filled conversations with Toby and others. This thesis was completed in spite of the best efforts of Russell Frizzell, who taught me a lot of things that I couldn't possibly learn in any school.

I am thankful to Dr. Rohit Grover, who has been an invaluable friend and mentor through my graduate school years. I also owe my gratitude to my friends and colleagues: Dr. Vien Van, Dr. Tarek Ibrahim, Wei-Yen Chen, Li-Chiang Kuo, Dr. Marcel Pruessner and Dr. Simarjeet Saini amongst many others.

Finally, I would like to express my deepest appreciation for the love, support and encouragement of my parents and Ranjani. I am indebted to them.

TABLE OF CONTENTS

Chapter 1

INTRODUCTION

The last few decades have seen the birth of electronics and its continuous miniaturization and increase in speed and complexity spurred by the increasing demand of its applications. Over the last few years, however, it has become increasingly hard to push the limits on speed and size of electronic devices as we near the physical limits inherent to electronic processing. Speed is determined by the size of devices and carrier mobility; smaller devices mean lower capacitance and shorter interconnects. However, there is a limit to how small a device can be and still exhibit the desired behavior before running into effects from non-uniform scaling and quantum effects.

An alternative approach to signal processing that is being explored over the last decade has been the use of photons. Using light to do the jobs that traditional electronics has been doing so far has certain advantages. The shortest light pulses that can be generated now are in the range of attoseconds [8], much shorter than anything comparable in electronics. Light, with a frequency ~ 10^{15} Hz, can be used as a carrier for signals that are much faster than what is possible by electronics. An optical waveguide can transport multiple signal streams in parallel using different wavelengths, something not possible on electronic interconnects. Also, multiple light beams can criss-cross without affecting each other provided there is no non-linearity in the medium at the crossing point. To be truly comparable to electronics, there has to be not only non-linear

photonic devices but such non-linear processes should exhibit time-scales that are faster than what is achievable through electronics [9].

However, there are two hurdles that need to be overcome before practical implementation of all-optical signal processing using such non-linear processes can be achieved: miniaturization and power reduction. Typically, optical non-linear processes are observed only at high intensities. One way to reduce the input power requirement is to use resonators, which provide intensity amplification at the cost of bandwidth. If the processing needs to be done for signals over a narrow range of wavelengths, then optical resonators provide a method for reducing power. However, implementing optical signal processing by bulk optics becomes difficult due to the complexity involved and this is where microresonators provide a very practical solution.

Optical microresonator devices provide a very useful platform on which various signal processing functions can be achieved in a much smaller volume compared to bulk optics and with much smaller power. Microring and microdisk resonators, first proposed by Marcatilli [10], are a subset of these microresonators that are uniquely suited for large scale integration of such functions. They have the advantage of being completely planar devices with input and output waveguides lying in the same plane thus allowing easy cascading of many such devices on a wafer [11-13]. Their versatility is apparent in the multitude of functions, such as optical channel add-drop filters, multiplexers and demultiplexers [14-16], high order filters [17-21], wavelength-selective reflectors [22-24], lasers [25-27], and modulators [28-30], that have been demonstrated using microrings and microdisks over the last few years. Besides variety in function, they have been implemented in a wide range of materials such as glass [31, 32], polymer [33, 34],

silicon [35], and III-V's such as indium phosphide and gallium arsenide[36, 37].

1.1 Dissertation Goals

Most of the microring and microdisk devices demonstrated so far have been for linear applications. Recently, there have been demonstrations of all-optical switching based on non-linear effects in passive gallium arsenide and indium phosphide microrings, where a high power pump beam is used to switch a lower power probe beam [38-40]. These devices have been used to implement optical logic gates [41]. However it is difficult to cascade passive devices to form photonic circuits due to 1) insertion losses associated with each stage, 2) lack of tunability for the ring resonators 3) high optical powers needed for switching and 4) due to the fact that the low power probe beam of the preceding stage has to form the high power pump beam for the succeeding stage.

The goal and novelty of this research is to develop electrically pumped microrings and microdisks based on indium phosphide for non-linear all-optical switches that overcome the limitations of passive devices and hence provide fully cascadable functional blocks for photonic circuits. This includes the development of an electrically pumped microring amplifier, which can compensate for insertion losses and boosts optical power between stages and also to use the enhanced non-linearity due to gain within the microring to effect non-linear all-optical switching at lower optical powers compared to passive devices.

1.2 Theory of Microrings

1.2.1 What is a microring resonator?

A microring is an optical waveguide that forms a ring shaped structure as shown

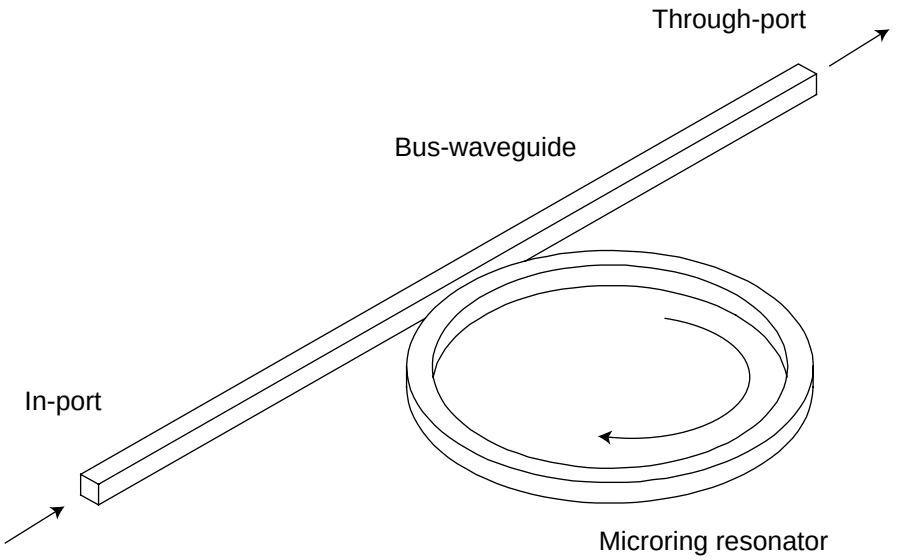

Figure 1.1: Schematic of a ring resonator. Light couples in and out of the resonator through the bus-waveguide.

in figure 1.1 and whose circumference is in the range of tens or hundreds of microns. Light can be coupled into and out of this structure by placing another waveguide (bus-waveguide) in close proximity to the ring structure. This occurs due to evanescent coupling between the two waveguides, when the tails of the optical modes in the two waveguides overlap each other and power is transferred from one mode to another [42]. Due to the closed loop structure, it behaves as a resonator and only light of certain frequencies can build up in intensity within the structure. The resonance frequencies are determined by the condition that the round-trip optical path length be equal to an integral number of wavelengths, i.e.

$$m \cdot \lambda_m = 2\pi R \cdot n_{eff} \tag{1.1}$$

Here, λ_m is the wavelength of the m'th longitudinal mode, R is the radius of the ring and n_{eff} is the effective index of the optical mode in the ring waveguide. At resonance, the

intensity in the ring can be many times higher than that in the waveguide.

1.2.2 The coupling region

Many important properties of the ring-resonator structure are determined by the geometry of the coupling region and hence it is useful to study the coupling region independently. Consider the structure shown in fig. 1.2, where two waveguides 'A' and 'B' form a coupled waveguide structure. The coupling region can be seen as a four port network and its transfer function can be described by a 2x2 matrix **M**, if two ports are designated as inputs and the other two as outputs. Writing the electric field as $\widetilde{E} \cdot e^{j\omega t}$, where $\widetilde{E}$ is a complex number, the fields at the various ports are related as:

$$\begin{bmatrix} \widetilde{E}_{2A} \\ \widetilde{E}_{2B} \end{bmatrix} = \begin{bmatrix} m_{11} & m_{12} \\ m_{21} & m_{22} \end{bmatrix} \cdot \begin{bmatrix} \widetilde{E}_{1A} \\ \widetilde{E}_{1B} \end{bmatrix} \tag{1.2}$$

The subscripts *A, B* and *1, 2* represent the two waveguides and ports respectively and m_{ij} are complex numbers. The transfer matrix can be simplified based on constraints derived from power conservation and coupled mode theory [43, 44].

The first constraint is that of power conservation. If there is no loss in the coupling region, then input power is equal to the output power:

$$\widetilde{\mathbf{E}}_{\mathbf{1}}{}^{\mathbf{T}} \cdot \widetilde{\mathbf{E}}_{\mathbf{1}}^{*} = \widetilde{\mathbf{E}}_{\mathbf{2}}{}^{\mathbf{T}} \cdot \widetilde{\mathbf{E}}_{\mathbf{2}}^{*} = \left[\mathbf{M} \cdot \widetilde{\mathbf{E}}_{\mathbf{1}}\right]^{\mathbf{T}} \cdot \mathbf{M}^{*} \cdot \widetilde{\mathbf{E}}_{\mathbf{1}}^{*} = \widetilde{\mathbf{E}}_{\mathbf{1}}{}^{\mathbf{T}} \cdot \left[\mathbf{M}^{\mathbf{T}} \cdot \mathbf{M}^{*}\right] \cdot \widetilde{\mathbf{E}}_{\mathbf{1}}^{*} \tag{1.3}$$

Thus,

$$\mathbf{M}^{*\mathbf{T}} \cdot \mathbf{M} = \mathbf{I} \tag{1.4}$$

or the matrix **M** is unitary. Writing out eqn. (1.4) in terms of the matrix components results in:

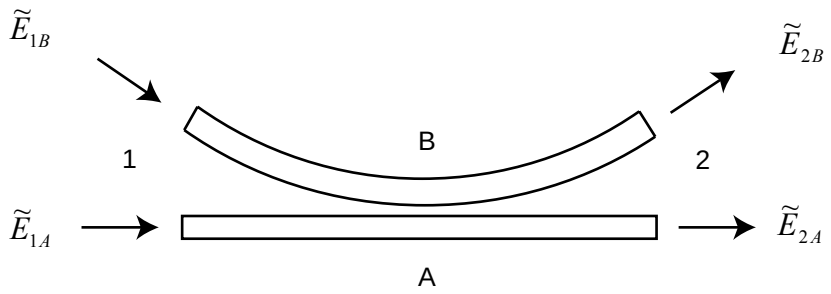

Figure 1.2: Schematic of coupling between two waveguides A and B. 1 and 2 are the input and output ports respectively.

$$\begin{aligned} |m_{11}|^2 + |m_{21}|^2 &= 1 \\ |m_{22}|^2 + |m_{12}|^2 &= 1 \\ m_{11}^* m_{12} + m_{21}^* m_{22} &= 0 \end{aligned} \tag{1.5}$$

For any unitary matrix, |det(**M**)| = 1. However, a stronger constraint can be derived using coupled mode theory for two co-propagating waveguides, which shows that the matrix **M** is a special unitary matrix, i.e. det(**M**) = 1.

$$m_{11} m_{22} - m_{12} m_{21} = 1 \tag{1.6}$$

From eqns. (1.5) and (1.6), it can be shown that:

$$\begin{aligned} m_{11} &= m_{22}^* \\ m_{12} &= -m_{21}^* \\ |m_{11}|^2 + |m_{12}|^2 &= 1 \end{aligned} \tag{1.7}$$

Thus, the transfer or coupling matrix can be written as:

$$\mathbf{M} = \begin{bmatrix} \widetilde{\tau} & \widetilde{\kappa} \\ -\widetilde{\kappa}^* & \widetilde{\tau}^* \end{bmatrix} \tag{1.8}$$

Here, $\widetilde{\tau}$ is the effective field transmission coefficient and $\widetilde{\kappa}$ the effective field coupling

coefficient. Power conservation is denoted by the last line in eqn. (1.7), i.e. $|\tilde{\tau}|^2 + |\tilde{\kappa}|^2 = 1$.

Next, we assume that the coupling region has zero physical length, i.e. a wave that is traveling in waveguide A from port 1 to 2 undergoes no phase change due to propagation distance between the input and output. This implies that $\tilde{\tau}$ can be represented by a single real number τ, henceforth called the field transmission coefficient. Moreover, from coupled mode theory, we know that the coupled power undergoes a phase change of $\pi/2$ from one waveguide to another. Hence, $\tilde{\kappa}$ can be written as $-j\kappa$, where κ is real number, henceforth called the field coupling coefficient. Thus, the transfer matrix for the coupling region shown in fig. 1.2 can be written as:

$$\mathbf{M} = \begin{bmatrix} \tau & -j\kappa \\ -j\kappa & \tau \end{bmatrix} \tag{1.9}$$

1.2.3 Intensity in the resonator and the transfer function

Using the coupling matrix derived in the previous section, the expressions for the transfer function of a ring or disk resonator and the intensity in the resonator can be derived. Consider the scheme of a single waveguide coupled to a single resonator as shown in fig. 1.3. Light enters the coupling region through the waveguide at port 2A and a part of the power couples into the ring at port 2B. It then traverses the circumference of the resonator and re-enters the coupling region through port 1B. Thus the electric field at port 2B can be written as:

$$\tilde{E}_{R2} = -j\kappa \cdot \tilde{E}_{in} + \tau \cdot \tilde{E}_{R1} \tag{1.10}$$

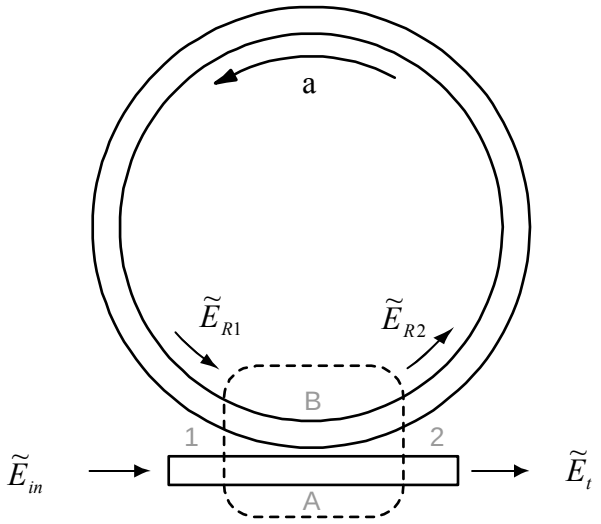

Figure 1.3: Schematic showing electric fields in an all-pass filter: a single ring coupled to a single bus-waveguide.

where

$$\tilde{E}_{R1} = a\tilde{E}_{R2}\exp(-j\beta L) \tag{1.11}$$

Here, '*a*' is the loss or gain factor associated with one round-trip, β is the propagation coefficient of the optical mode and L is the round-trip length. From eqns. (1.10) and (1.11), the electric field at port 1B can be expressed in terms of the input field as:

$$\tilde{E}_{R2} = \tilde{E}_{in} \cdot \frac{-j\kappa}{1 - a\tau\exp(-j\beta L)} \tag{1.12}$$

Thus, the intensity in the ring is given by the expression:

$$I_R = I_{in} \cdot \frac{\kappa^2}{1 + a^2\tau^2 - 2a\tau\cos(\beta L)} \tag{1.13}$$

The electric field at the through-port (2A) is given by:

$$\tilde{E}_t = \tau\tilde{E}_{in} - j\kappa\tilde{E}_{R1} \tag{1.14}$$

Using eqns. (1.11) and (1.12) in (1.14), the transmitted field can be expressed in terms of the incident field as:

$$\widetilde{E}_t = \widetilde{E}_{in} \cdot \frac{\tau - a\exp(-j\beta L)}{1 - a\tau\exp(-j\beta L)} \tag{1.15}$$

Thus the transmitted intensity is given by:

$$I_t = I_{in} \cdot \frac{\tau^2 + a^2 - 2a\tau\cos(\beta L)}{1 + a^2\tau^2 - 2a\tau\cos(\beta L)} \tag{1.16}$$

Equations (1.16) and (1.13) quantify the intensity response of a microring or microdisk resonator coupled to a single waveguide. The intensity gain in the ring and transfer function are plotted as a function of wavelength in figure 1.4 for a typical indium phosphide passive ring resonator of radius 10 microns with the various parameters as indicated. At resonance, the intensity in the ring can be many times that of the input waveguide, while the transmitted power is at a minimum. The transfer characteristics are similar to a notch-filter. A related quantity is the field enhancement at resonance, or FE, and is given by:

$$\left|\frac{\widetilde{E}_R}{\widetilde{E}_{in}}\right| = \frac{\kappa}{1 - a\tau} \tag{1.17}$$

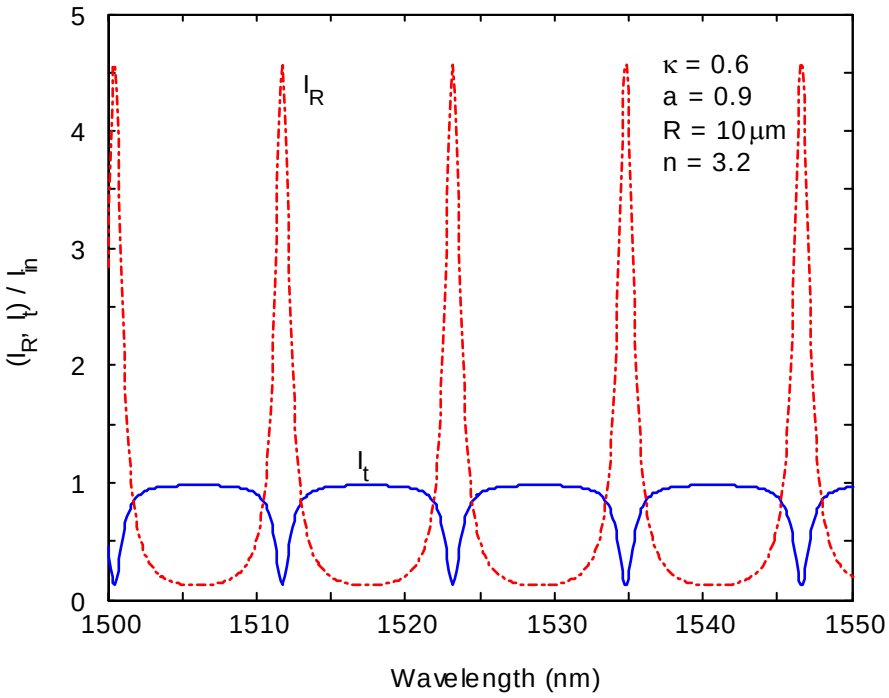

Figure 1.4: Plot of normalized intensity in the ring and at the through-port as function of wavelength for a typical indium phosphide microring resonator.

It is worth examining the factors that determine the various parameters mentioned above. The coupling matrix parameters, κ and τ, are mostly determined by the geometry of the coupling region, such as gap between ring and waveguide and the mode mismatch due to waveguide asymmetry. There is an exponential drop of coupled power with gap-distance. There is a slow variation with wavelength that is negligible for the typical bandwidths encountered in these resonators. On the other hand, there is significant dependence on polarization.

The round-trip loss factor, '*a*', is determined by the various loss mechanisms present such as scattering from side-wall roughness, bending losses, free-carrier absorption, and leakage to substrate [45]. If there is a gain medium, such as pumped quantum wells within the ring, then '*a*' can be greater than one. The effect of '*a*' on ring

characteristics is examined in more detail in a later section.

1.2.4 Phase response of a single microring

The phase characteristics of the notch-filter, i.e. a single ring coupled to a single waveguide, can be derived from eqn. (1.15), i.e.

$$\Phi(\lambda) = \mathrm{Arg}\left(\frac{\tau\text{-}a\exp(-j\beta(\lambda)L)}{1 - a\tau\exp(-j\beta(\lambda)L)} \right) \tag{1.18}$$

Here, $\beta(\lambda) = 2\pi n_{eff} / \lambda$, where n_{eff} is the effective index. This can be simplified to:

$$\Phi(\lambda) = \tan^{-1}\left(\frac{a\kappa^2 \sin(\beta L)}{\tau(1+a^2) - a(1+\tau^2)\cos(\beta L)} \right) \tag{1.19}$$

For small deviations from resonance, the phase response is essentially linear with respect to the round-trip phase. The phase response is plotted as a function of round-trip phase, $\phi = \mathrm{mod}(\beta L, 2\pi)$, in figure 1.5 for a range of ring parameters. Note the sharp variation just around resonance ($\varphi = 0$). By operating the ring resonator at or near resonance, the output phase (and intensity) can be made very sensitive to small changes in the effective index.

1.2.5 Critical coupling

For fixed loss in the ring, the intensity enhancement in the ring at resonance is a function of the coupling constant. As the coupling increases, the intensity in the ring reaches a maximum and decreases beyond. The value of κ at which the intensity reaches the maximum can be found by differentiating eqn. 1.17 and equating to zero. This condition is known as critical coupling and the value of the coupling constant is given by:

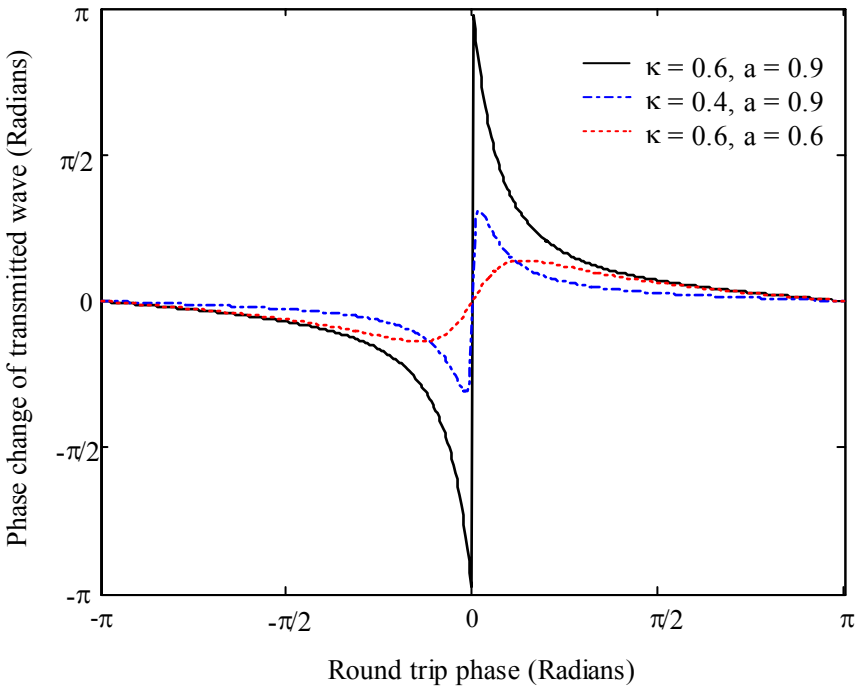

Figure 1.5: Phase response of an all-pass microring resonator for different values of the ring constants. The x-axis denotes the change in round-trip phase as the wavelength or effective index

$$\kappa_C = \sqrt{1-a^2} \tag{1.20}$$

At critical coupling, the transmitted intensity drops to zero at resonance and all the incident power is absorbed in the ring. Figure 1.6 shows a plot of the intensity enhancement in the ring as a function of κ for various values of a. The locus of the maxima of all such curves is given by the equation:

$$\frac{I_R}{I_{in}} = \frac{1}{\kappa^2} \tag{1.21}$$

1.2.6 Loss and gain in the ring

While the coupling constant is determined entirely by the geometry, the loss in the

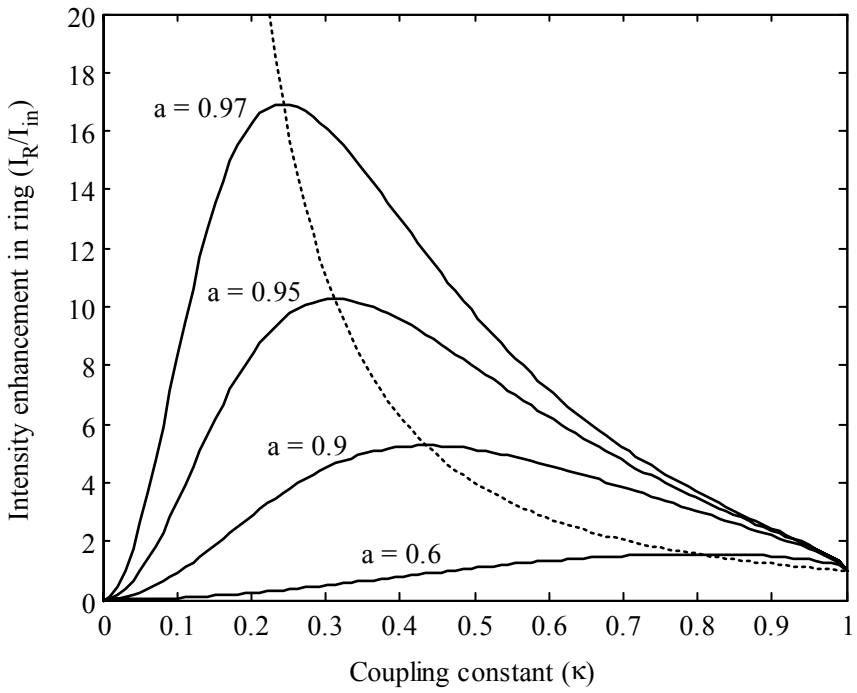

Figure 1.6: Plot of intensity enhancement within the ring resonator as a function of the coupling constant for different values of round-trip loss. The locus of all the peaks is indicated by a dashed curve.

ring is determined by both fixed and variable factors, especially if there is an active region in the optical core. Changing the carrier density in the active region, either by optical pumping or electrical injection changes the gain or loss for the optical mode. The loss/gain in the ring can also be dependent on the intensity in the ring due to optical non-linear effects such as absorption saturation, Kerr effect or gain saturation.

The fixed sources of loss are due to [45]:

- Scattering from sidewall roughness.
- Radiation losses due to bending in waveguide.
- Leakage to substrate.
- Free carrier absorption.

The index contrast in semiconductor microrings is fairly high and hence the bending losses are insignificant for radii larger than 1 micron, provided there is no leakage to substrate. The bending losses can be estimated by solving the wave equations after conformal mapping and by Wenzel-Kramers-Brillouin (WKB) approximations [46-48]. However, the loss is insignificant compared to scattering losses and/or active-region absorption and hence can be neglected for radii larger than 1-2 microns in semiconductor microrings and microdisks.

The scattering losses due to surface roughness at the core-clad interface can be estimated using Tien's expression based on the Rayleigh scattering criterion [49], although more complex formulae exist [50, 51], which require knowledge of periodicity in the surface roughness. The scattering loss, as estimated in [49], is given by:

$$\alpha_{sc} = 2\sigma^2 (n_{eff}^2 - n_0^2) k_0^2 \frac{k_x}{\beta} E_s^2 \tag{1.22}$$

Here, σ is the RMS surface roughness, n_{eff} is the effective index of the optical mode, n_0 is the cladding index, k_0 is the free-space propagation vector, k_x is the transverse component of the propagation vector in the waveguide, β is the longitudinal component, and E_s is the electric field at the surface, where the field integral is normalized to unity.

Free-carrier absorption loss occurs in semiconductor resonators that have dopants, such as in active structures [52, 53]. The absorption results in the free carrier transition to higher levels in the conduction or valence bands that then decay non-radiatively back to the ground state. The absorption cross-section is seen to be much higher for holes than for electrons [54]. Typical values for absorption in indium phosphide are 5 cm^{-1} for n-dopant density of 10^{18} cm^{-3} and 25 cm^{-1} for p-dopant density of $7x10^{17}$ cm^{-3}.

Another fixed source of loss is the mode mismatch between straight and curved waveguide regions in race-track shaped micro-resonators [45]. More generally, there is a mode-mismatch loss whenever there is a discontinuity in the radius of curvature of the waveguides and/or the propagation constant. This can be alleviated to some extent by off-setting the straight-sections to obtain better overlap.

The net loss is the sum of all the individual loss/gain coefficients. The loss coefficient is related to the round-trip loss/gain factor 'a' as indicated below. Here, T is the field transmission factor for mode mismatches at discontinuities in the waveguide.

$$\alpha_{tot} = \alpha_{scat} + \alpha_{bend} + \alpha_{carr} + \alpha_{act} \tag{1.23}$$

$$a = T \exp(\alpha_{tot} L/2) \tag{1.24}$$

The α_{act} term in eqn. (1.23) refers to the variable loss/gain contribution from an active region in the core. By injecting carriers into an optical gain producing region within the microresonator, such as a quantum well, the net loss can be tuned to the desired value simply by varying the current or optical pump intensity. Increasing the current to a high enough value can provide sufficient gain to offset all other losses and make the ring transparent. Increasing the current even higher results in net amplification of the transmitted signal. Lasing occurs when the round-trip amplification if sufficient to overcome the static and coupling losses in the micro-resonator. These characteristics are examined in more detail in the chapter on microring amplifiers and lasers.

1.2.7 Resonator bandwidth, free spectral range and finesse

The bandwidth of a microring or microdisk resonator corresponds to the width of the resonances shown in figure 1.4. Its practical significance is that it limits the data-rate

that the ring resonator can handle for a carrier signal at the wavelength corresponding to the resonance. It also determines how selective a micro-resonator can be when operating on a particular channel (wavelength) among many closely spaced channels. It is indirectly related to the intensity enhancement in the resonator. There is a trade-off between resonator bandwidth and intensity gain; higher bandwidths mean lower intensity gain and vice-versa. The bandwidth can be calculated from the ring parameters by equating the RHS of eqn. (1.13) to half the maximum. This results in:

$$\cos(\delta\phi) = \frac{4a\tau - a^2\tau^2 - 1}{2a\tau}. \tag{1.25}$$

Here,

$$\delta\phi = \delta(\beta L) = \delta\left(\frac{2\pi n_{eff} L}{\lambda}\right) = \frac{-2\pi n_{eff} L}{\lambda^2} \cdot \delta\lambda . \tag{1.26}$$

For small bandwidths, $\cos(\delta\phi) \approx 1 - \frac{1}{2}(\delta\phi)^2$. Thus, from eqns. (1.25) and (1.26), the full-width at half maximum can be calculated:

$$\delta\lambda_{FWHM} = 2\delta\lambda \approx \frac{\lambda^2}{\pi n_{eff} L} \cdot \frac{1 - a\tau}{\sqrt{a\tau}}. \tag{1.27}$$

Another quantity that characterizes a microresonator is the free spectral range or FSR. It refers to the wavelength span between two consecutive resonances. For two consecutive resonances, the longitudinal mode number changes by unity.

$$m \cdot \lambda_m = L \cdot n_{eff} = (m-1) \cdot (\lambda_m + \Delta\lambda) \tag{1.28}$$

Re-arranging eqn. (1.28) and assuming $\Delta\lambda << \lambda$ ($m >> 1$), gives the expression for the FSR.

$$\Delta\lambda = \frac{\lambda_m(\lambda_m + \Delta\lambda)}{L \cdot n_{eff}} \approx \frac{\lambda^2}{L \cdot n_{eff}} \tag{1.29}$$

Thus, a small round-trip length implies a large free spectral range.

The FSR, together with the bandwidth, determines how many channels can be operated on without overlapping between them. A large FSR combined with a small bandwidth means a higher number of channels can be accommodated. A figure of merit which quantifies this capability is the finesse, *F*. It is defined as the ratio of the FSR to the FWHM.

$$F = \frac{1 - a\tau}{\pi\sqrt{a\tau}} \tag{1.30}$$

The finesse, limited by the approximations used to derive FSR and FWHM, is independent of the geometric dimensions of the resonator, wavelength or effective index and hence is an ideal quantity for comparing different resonators. It is dependent only on the loss and the coupling constant.

1.2.8 The Q factor and the cavity photon lifetime

The Q or quality factor of a resonator measures the ability of a resonator to store energy. It is defined as the ratio of the stored energy to the energy lost per oscillation. By loss it is meant either absorption in the ring or coupling out to the bus waveguide.

$$Q = \frac{\text{energy in ring}}{\text{power lost} / \omega} \tag{1.31}$$

Alternatively, it can be shown that this definition is equivalent to the ratio of the resonance wavelength to the bandwidth.

$$Q = \frac{\lambda_m}{\delta\lambda_{FWHM}} = \frac{\pi n_{eff} L}{\lambda_m} \cdot \frac{\sqrt{a\tau}}{1 - a\tau} \tag{1.32}$$

Unlike the finesse, F, the Q-factor is dependent on the resonator dimensions as well as the wavelength.

A related quantity is the cavity photon lifetime, τ_{ph}. It refers to the average time a photon stays in the cavity before being absorbed or coupled out. It is determined by the bandwidth of the resonance as:

$$\tau_{ph} = \frac{1}{\delta f_{FWHM}} = \frac{\pi n_{eff} L}{c} \cdot \frac{\sqrt{a\tau}}{1 - a\tau} \tag{1.33}$$

The cavity photon lifetime imposes a fundamental limit on the speed of modulations to the carrier signal. Any modulation to the carrier signal that is faster than the cavity photon lifetime is attenuated and/or lost at the output port. The physical significance is this ultimately limits how fast all-optical signal processing can be done using these microresonators. To give an estimate of this limit, the cavity photon lifetime of a 10 micron radius semiconductor microring, with a coupling constant κ = 0.3, and no loss, is about 40 ps.

1.2.9 Optical channel dropping filters

So far, the theory has been developed for a single microring or disk coupled to a single bus-waveguide. This is known as the all-pass or notch filter configuration. Frequently, structures with two buses coupled to a single resonator are encountered as shown in figure 1.7 [55]. The analysis of this structure is fairly easy for single input schemes, where only one port is the input and the rest are all outputs. The change required is intuitively obvious in that the round-trip loss now needs to account for the

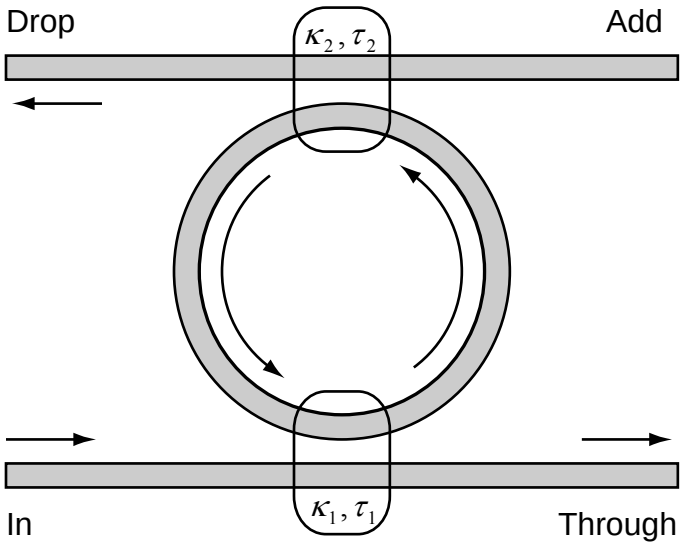

Figure 1.7: Schematic of an optical channel dropping filter configuration. A single microring is coupled to two bus waveguides.

coupling out of energy through the second coupling region. Thus, the necessary substitution is:

$$a \rightarrow a\tau_2 \tag{1.34}$$

Using the above substitution in the expressions for intensity in the ring and at the through-port gives:

$$I_R = I_{in} \cdot \frac{\kappa_1^2}{1 + a^2\tau_1^2\tau_2^2 - 2a\tau_1\tau_2\cos(\beta L)} \tag{1.35}$$

$$I_t = I_{in} \cdot \frac{\tau_1^2 + a^2\tau_2^2 - 2a\tau_1\tau_2\cos(\beta L)}{1 + a^2\tau_1^2\tau_2^2 - 2a\tau_1\tau_2\cos(\beta L)} \tag{1.36}$$

The intensity at the drop-port is proportional to the intensity in the ring at the second coupling region:

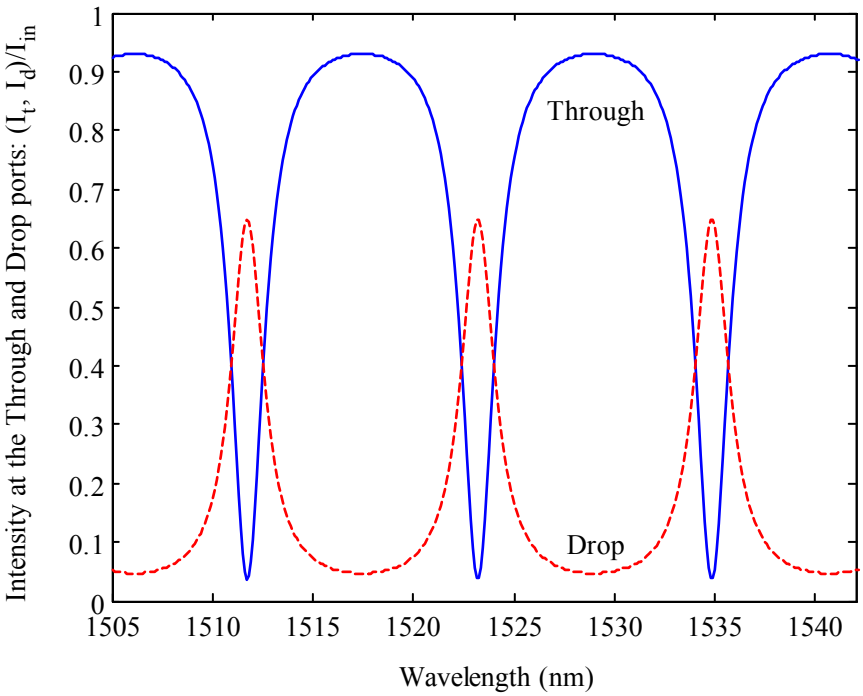

Figure 1.8: Outputs from an add-drop type of microring device. The blue curve is the intensity at the through-port and the red curve is the intensity at the drop port.

$$I_{drop} = I_{in} \cdot \frac{a\kappa_2^2\kappa_1^2}{1 + a^2\tau_1^2\tau_2^2 - 2a\tau_1\tau_2\cos(\beta L)} \tag{1.37}$$

Here, the subscripts refer to the two coupling regions. Figure 1.8 shows a plot of the intensity at the through-port and drop-port for an optical channel dropping filter (OCDF) type of microresonator. Note how the channels that are dropped from the through-port appear at the drop-port. Likewise, any channels that are present at the port marked add-port are added to the output at the through-port.

1.3 Coupling Schemes

1.3.1 Lateral coupling

There are two ways to couple light from the bus-waveguide to the microring or

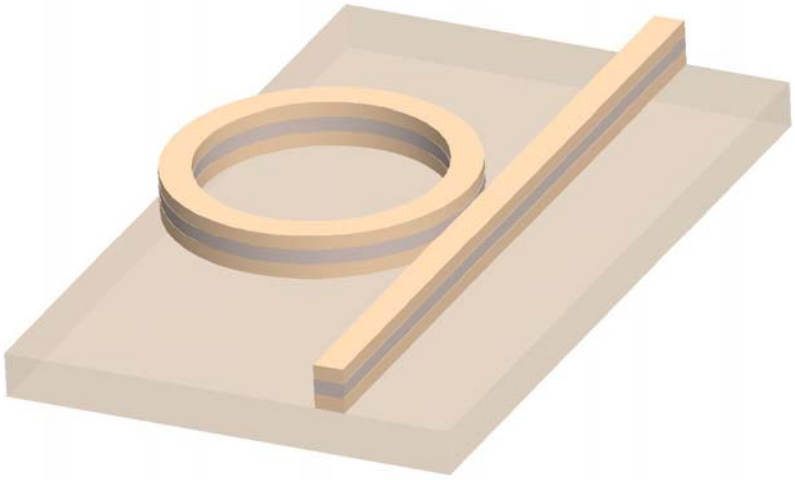

Figure 1.9: Schematic of a laterally coupled ring resonator. The ring and bus waveguides are located in the same plane.

microdisk. Traditionally, lateral coupling, where the bus-waveguide is in the same plane as the microring, was used due to the ease of fabrication and simpler layer structure [14, 56]. This is illustrated in figure 1.9. In this scheme, the optical core material for the ring and bus is identical. The coupling constant is determined by the etched gap between the bus-waveguide and the ring. As the coupling strength has an exponential dependence on the gap, it makes the scheme very sensitive to the lithography and etch processes that define the gap. For high index contrast systems, such as semiconductors, the gap thickness has to be in the range of 100 nm for significant coupling, thus requiring e-beam lithography. Also, it is typically difficult to separate the passive and active regions as there is only one optical core. It is advantageous in terms of processing complexity as the both and ring features are defined in one lithography step and on one side of the wafer only. Also, there is more efficient transport of heat to the substrate from the ring.

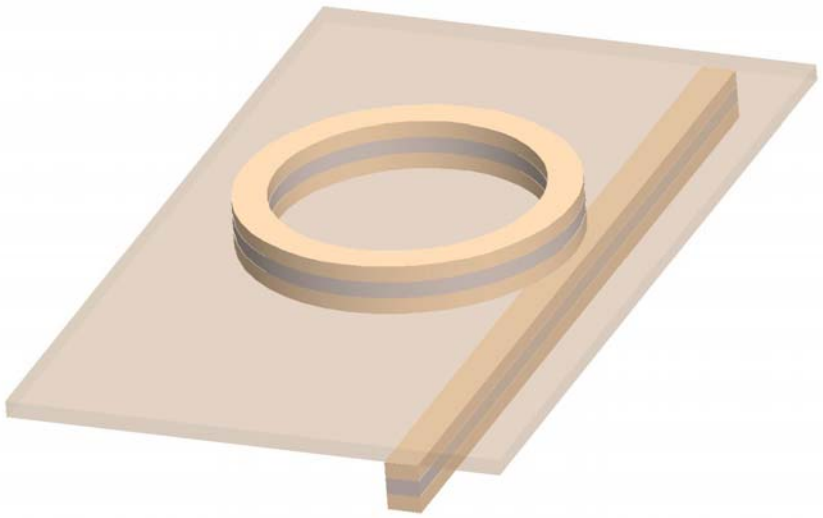

Figure 1.10: Schematic of a vertically coupled ring resonator. The ring and bus waveguides are on different layers.

1.3.2 Vertical coupling

As the functions got more complicated a vertical coupling scheme is desirable, where the bus-waveguide is in a plane vertically offset from the microring [32, 57]. Vertical coupling, though harder to fabricate, provides for two optical cores with the ring and bus using different levels. The ring level optical core can contain active regions for controlling gain or loss while the bus level can have a passive core for low loss transport. This is illustrated in figure 1.10. The coupling strength is determined by the thickness of the layer between the ring and bus optical cores. This thickness is determined by epitaxy and hence can be precisely controlled and in a repeatable manner [58]. The disadvantage is that fabrication is complicated. The bus and ring features need to be defined in separate lithography steps and also double-sided processing becomes necessary. Double-sided processing involves flip-transfer of the semiconductor epitaxial layers (epi-layer) to a

carrier substrate so that the bottom side of the layer stack is accessible for further processing. Depending on the kind of bonding used for epi-layer transfer, heat transfer from the epi-layers to the carrier substrate might not be as good as in lateral coupling.

1.4 Outline

This chapter developed some of the introductory theory of microrings and the motivation and goals for the research. The next chapter will develop the theory for non-linear interactions in microrings, especially active devices. In chapter three, the fabrication process for microrings and microdisks is described in detail. Chapter four describes the need and method of surface passivation in active microrings. Chapters five and six present the results from microring amplifiers and lasers and measurements of non-linear optical processes in microdisks respectively. Chapter seven concludes this thesis with a discussion on the limitations and outlook for the devices developed here.

Chapter 2

OPTICAL NON-LINEARITY IN SEMICONDUCTORS

The last chapter discussed some of the basic concepts regarding microring and microdisk resonators. This chapter will examine optical non-linear processes, especially gain and absorption saturation effects in semiconductors. It will also study the enhancement of non-linear optical processes by incorporating them in microring and disk resonators.

2.1 Non-linear Susceptibility

The interaction of an EM wave with a non-magnetic medium is determined by the susceptibility, or equivalently the refractive index or dielectric constant, of the medium. Specifically, the polarization per unit volume is proportional to the applied electric field and is given by

$$P = \varepsilon_0 \chi E \tag{2.1}$$

Here, ε_o is permittivity of vacuum and χ is the susceptibility of the medium and is a dimensionless number. For small enough electric fields, the susceptibility of the medium is a constant and the medium is said to exhibit linear behavior. However, at high enough electric fields, this is no longer true and the susceptibility becomes dependent on the electric field. This can be expressed in equation form as

$$P = \varepsilon_0 \left(\chi^{(1)} + \chi^{(2)} E + \chi^{(3)} E^2 + \cdots \right) E \tag{2.2}$$

Here $\chi^{(1)}$ is the linear susceptibility while $\chi^{(2)}$ and $\chi^{(3)}$ are the second and third order susceptibilities respectively. For most materials, the non-linear polarization response is a consequence of the non-parabolic nature of the electron potential around the nucleus [59]. In semiconductors, the non-linear response can also be due to phenomena related to the band-structure such as two-photon absorption, gain and absorption saturation. Strictly speaking, susceptibility coefficients given above need to be represented using tensors as the polarization direction need not be in the direction of the applied field. This is the consequence of a non-symmetric electron potential around the nucleus. Generally, the susceptibility coefficients are a function of the frequency of the incident electric fields besides having complex values (absorption / gain change). The susceptibility coefficient is related to the refractive index and absorption coefficient as

$$\begin{aligned} n &= \mathrm{Re}(\sqrt{1+\chi}) \\ \alpha &= \frac{4\pi}{\lambda} \mathrm{Im}(\sqrt{1+\chi}) \end{aligned} \tag{2.3}$$

The second-order susceptibility coefficient $\chi^{(2)}$ is non-zero only in non-centrosymmetric media [59]. The resulting polarization, $P^{(2)}$, does not have any frequency component that is identical to the incident monochromatic electric field. The second-order susceptibility results in phenomena such as optical rectification [60], second-harmonic generation [61], optical parametric amplification [62], or more generally, sum and difference frequency generation, and the Pockel electro-optic effect .

2.2 The Optical Kerr-effect

The third-order susceptibility coefficient $\chi^{(3)}$ is non-zero in all media. For a

monochromatic incident EM wave, the resulting polarization, $P^{(3)}$, has a component at the same frequency as the incident wave besides the third harmonic. Assuming an incident electric field $E(\omega) = E_0\cos(\omega t)$, the third order polarization is given by:

$$\begin{aligned} P^{(3)} &= \varepsilon_0 \chi^{(3)} \left(E_0 \cos(\omega t)\right)^3 \\ &= \frac{1}{4}\varepsilon_0 \chi^{(3)} E_0^3 \cos(3\omega t) + \frac{3}{4}\varepsilon_0 \chi^{(3)} E_0^3 \cos(\omega t) \end{aligned} \tag{2.4}$$

The first term represents third harmonic generation while the second term describes an additional contribution at the frequency of the incident wave. Thus,

$$P(\omega) = \varepsilon_0 \left[\chi^{(1)} + \frac{3}{4}\chi^{(3)} I(\omega) \right] E(\omega) \tag{2.5}$$

This manifests as an intensity dependent refractive index and absorption coefficient given by:

$$n = n_0 + n_2 I \tag{2.6}$$

$$\alpha = \alpha_0 + \alpha_2 I \tag{2.7}$$

Assuming $\chi^{(3)} I << n_o^2$, n_2 and α_2 can be calculated from eqns. (2.3) and (2.5) as:

$$n_2 = \frac{3}{8}\frac{\mathrm{Re}\left[\chi^{(3)}\right]}{n_0^2} \tag{2.8}$$

$$\alpha_2 = \frac{3\pi}{2}\frac{\mathrm{Im}\left[\chi^{(3)}\right]}{\lambda n_0^2} \tag{2.9}$$

The third order susceptibility results in phenomena such as third harmonic generation, intensity dependent refractive index, four-wave mixing and self-focusing.

The source of non-linear susceptibility in semiconductors can be due to atomic

polarization, or phenomena related to the band-structure such as two-photon absorption, absorption saturation and gain saturation. Other sources of non-linear susceptibility include thermal effects and electrostriction but they are much slower compared to electronic polarization or band-structure phenomena and hence will not be considered. The rest of this chapter will examine the strength of each of these phenomena and compare the relative merits of each. The non-linearity might affect the real part of the susceptibility (refractive index) or the imaginary part (absorption) or both. In the case of changes to refractive index, the effect is to change the optical phase of the incident wave, but this can be effectively converted to an intensity modification though the use of some kind of interference device like a resonator or interferometer. Ultimately, it is intensity modulation that is detected at a photo-detector.

2.3 Two-Photon Absorption

Two-photon absorption (TPA) is a non-parametric process by which a semiconductor absorbs two photons simultaneously with energies below the band-gap, but whose sum is larger than the band-gap, and creates an electron-hole pair [7, 63, 64]. The TPA generated electron hole pairs results in a modification of the refractive index primarily through two effects: the shift in the plasma frequency of the free carriers and change in absorption at the band-edges [7]. When the incident light is monochromatic the photon energy needs to be at least half the band-gap for TPA to take place.

Since TPA needs two photons for pair creation it follows that carrier generation is proportional to the square of the optical intensity. Thus, the carrier rate-equation can be expressed as:

$$\frac{dN}{dt} = \frac{\alpha_2 I^2}{2\hbar\omega} - \frac{N}{\tau_c} \tag{2.10}$$

Here, α_2 is the two-photon absorption coefficient and τ_c is the carrier-lifetime. At steady-state, the excess carrier density is given by:

$$\Delta N = \frac{\alpha_2 \tau_c I^2}{2\hbar\omega} \tag{2.11}$$

The effect of the excess carriers on refractive index is determined by the shift in the plasma frequency as well as the change in absorption at the band-edge and can be approximated as:

$$\Delta n = -\sigma_n \Delta N = -\frac{\sigma_n \alpha_2 \tau_c I^2}{2\hbar\omega} \tag{2.12}$$

Here σ_n is the refractive volume of the semiconductor. Thus, the refractive index can be written as:

$$n = n_0 - \frac{\sigma_n \alpha_2 \tau_c I^2}{2\hbar\omega} \tag{2.13}$$

The attenuation of an incident wave due to TPA has two components besides the linear term. Besides the actual two-photon absorption, there is additional attenuation due to free-carrier absorption from the generated electron-hole pairs.

$$\begin{aligned} \frac{dI}{dz} &= -\alpha_0 I - \alpha_2 I^2 - \sigma_{FC}(\Delta N) I \\ &= -\alpha_0 I - \alpha_2 I^2 - \frac{\sigma_{FC} \alpha_2 \tau_c I^3}{2\hbar\omega} \end{aligned} \tag{2.14}$$

Here, the first term represents linear absorption such as due to scattering, the second term is the two-photon absorption and the last term represents free-carrier absorption. σ_{FC} is

the free-carrier absorption coefficient, which is usually much higher for holes than for electrons. Thus the net absorption coefficient can be written as:

$$\alpha = \alpha_0 + \alpha_2 I + \frac{\sigma_{FC}\alpha_2\tau_c I^2}{2\hbar\omega} \tag{2.15}$$

Two-photon absorption has been used to demonstrate a number of applications including optical thresholding, correlation and all-optical switching [65, 66].

2.4 Absorption Saturation

When the energy of the incident photons is greater than the band-gap (or just below band-gap) there is absorption resulting in the creation of one electron-hole pair (or exciton) for every photon absorbed. For low enough intensities, the absorption cross-section is a constant as the upper energy level is mostly empty. However, at high intensities, the number of carriers generated can be so high that stimulated emission becomes comparable to absorption and hence net absorption drops. For the sake of simplicity, the absorption can be modeled as a two-level system. The absorption and refractive index is assumed to be of the form:

$$\alpha = \alpha_0 - \sigma_\alpha N \tag{2.16}$$

$$n = n_0 - \sigma_n N \tag{2.17}$$

Here, α_o and n_o are the linear coefficients for absorption and refractive index respectively, σ_α and σ_n are the absorption and refractive index cross-sections respectively, and N is the number of carriers generated as a result of absorption. At steady state, the carrier generation is related to the absorption coefficient and incident intensity as:

$$N = \frac{\alpha \tau_c I}{\hbar \omega} \tag{2.18}$$

Here, τ_c is the effective carrier life-time. Using the expression for the carrier density in eqn. (2.15), the absorption coefficient can be written as:

$$\begin{aligned} \alpha &= \alpha_0 - \frac{\sigma_\alpha \alpha \tau_c I}{\hbar \omega} \\ \alpha &= \frac{\alpha_0}{1 + \frac{\sigma_\alpha \tau_c I}{\hbar \omega}} \end{aligned} \tag{2.19}$$

Here, $\hbar\omega / \sigma_\alpha \tau_c$ is the saturation intensity (I_{sat}) and denotes the intensity at which the absorption coefficient is half the initial magnitude. Thus, the variation of the absorption coefficient with the incident intensity can be expressed as:

$$\alpha = \frac{\alpha_0}{1 + \frac{I}{I_{sat}}} \tag{2.20}$$

For the refractive index, the expressions for carrier density (eqn. 2.17) and absorption coefficient (eqn. 2.20) can be used in eqn. (2.16) to give:

$$n = n_0 - \frac{\sigma_n \alpha_0}{\sigma_\alpha} \cdot \left[\frac{\frac{I}{I_{sat}}}{1 + \frac{I}{I_{sat}}} \right] \tag{2.21}$$

As the incident intensity approaches infinity, the absorption becomes zero while the index change reaches $\Delta n_{sat} = -\sigma_n \alpha_0 / \sigma_\alpha$ asymptotically.

2.5 Gain Saturation

When excess carriers are generated in a direct band-gap semiconductor, either by

injection in a p-n junction or optical pumping, some of them recombine by radiation. The radiation can be either spontaneous or stimulated. A light beam, with photon energy greater than the band gap, traversing such a region undergoes both gain and loss. The gain is due to stimulated emission resulting in the recombination of electron-hole pairs, while loss occurs due to absorption resulting in the creation of electron-hole pairs. For sufficiently high injection, the electron density in the conduction band exceeds that of the valence band (and vice-versa for holes) and the stimulated emission is greater than absorption. In such a case, the incident light beam undergoes a net gain while passing through the region. The dependence of gain on the carrier density can be approximated by a linear function as:

$$g = a_g (N - N_t) \tag{2.22}$$

Here, N is the carrier density in the active region, N_t represents the transparency carrier density, and a_g is a constant. At steady state, the carrier density in the active region is determined by the injection and recombination rates:

$$\frac{J}{qd} - \frac{gI}{\hbar\omega} - \frac{N}{\tau_c} = 0 \tag{2.23}$$

The first term represents the carrier injection into the active region of thickness d by a current density J. The second term represents the carrier recombination rate due to stimulated emission (gain) for an optical wave of intensity I traversing the active region. The last term represents carrier recombination from processes other than stimulated emission such as spontaneous emission and non-radiative recombination mechanisms such as Auger, Shockley-Reed-Hall, and surface recombination. From eqns. 2.22 and 2.23, the steady-state carrier concentration can be expressed as:

$$N = \frac{N_0 + N_t \cdot \dfrac{I}{I_{sat}}}{1 + \dfrac{I}{I_{sat}}} \tag{2.24}$$

$N_0 = \tau_c J / qd$ is the carrier-density when there is no incident optical wave and $I_{sat} = \hbar\omega / \tau_c a_g$ is the saturation intensity similar to the case of absorption saturation in the previous section. Thus, the gain coefficient g can be expressed as a function of current density and optical intensity using eqns. 2.22 and 2.24:

$$g = \frac{a_g (N_0 - N_t)}{1 + \dfrac{I}{I_{sat}}} \tag{2.25}$$

Equivalently,

$$g = \frac{g_0}{1 + \dfrac{I}{I_{sat}}} \tag{2.26}$$

$g_0 = a_g (N_0 - N_t)$ is the material gain when there is no incident optical intensity.

To determine the variation of refractive index with carrier density and optical intensity, one can assume a functional form similar to the absorption saturation case as in eqns. 2.15 and 2.16 or equivalently use the linewidth enhancement factor approach. The linewidth enhancement factor, or the Henry α-factor, is defined as the ratio of the change in the real and imaginary part of the refractive index [67]. The coupling between the real and imaginary part of the refractive index is due to the dependence on carrier density.

$$\alpha_H = -\frac{4\pi}{\lambda} \cdot \frac{dn}{dg} = -\frac{4\pi}{\lambda} \cdot \frac{dn/dN}{dg/dN} \tag{2.27}$$

Using the expression for gain g from eqn. 2.22, the real part of refractive index can be expressed using eqn. 2.27 as

$$n = n_0 - \frac{a_g \alpha_H \lambda N}{4\pi} \tag{2.28}$$

This is similar to eqn. 2.16 for the case of absorption saturation, where it was assumed that both index and absorption had a linear dependence on carrier density. The constant n_0 is the refractive index when there is no current injection and no incident light. Using the expression for carrier density from eqn. 2.24 in eqn. 2.28, the refractive index can be expressed as:

$$n = n_0 - \frac{\alpha_H \lambda a_g N_0}{4\pi} + \frac{\alpha_H \lambda g_0}{4\pi} \frac{\frac{I}{I_{sat}}}{1 + \frac{I}{I_{sat}}} \tag{2.29}$$

The first term is the unperturbed refractive index. The second term is the index change caused by injection of carriers into the active region due to an applied bias. The third term represents the index change caused by an incident optical beam that modifies the carrier density due to stimulated emission.

The Henry α-factor has been measured for various semiconductor materials in both quantum well and bulk structures and typically lies in the range of 2-6 [68-70]. Quantum wells typically have lower values compared to bulk structures [71].

2.6 Comparison of Optical Non-Linear Processes

In this section, I will compute the index changes produced by the various non-linear effects mentioned above as a function of optical intensity for an InP system at 1550

nm. The goal of this exercise is to compare and pick the optimal method for achieving non-linear switching at the lowest optical intensities. The various parameter values used in the calculation are indicated in table 2.1. In all cases, the waveguide is assumed to be 0.5 μm x 0.5 μm. For the Kerr effect, bulk InGaAsP with a band-edge at 1430 nm is assumed as the medium. For TPA, the waveguide is assumed to be an InGaAsP multi-quantum well structure with InP barriers [7]. For the gain saturation case, the waveguide is assumed to contain a few InGaAsP quantum wells in the middle of a larger quaternary wave-guiding region. Figure 2.1 shows the resulting log-log plot of the absolute refractive index change as a function of intensity for the three different processes: optical Kerr effect, two photon absorption and gain saturation. Gain saturation is seen to be the most efficient mechanism for achieving non-linear refraction. Between TPA and Kerr effect, the latter dominates below a threshold intensity beyond which, the TPA process becomes more efficient than the Kerr effect. Absorption saturation is similar to gain saturation in its behavior and is equally suitable for low intensity non-linear refraction if absorption losses are not critical to device operation. However, one critical difference is the direction of change of the refractive index, which is negative for absorption saturation and positive for gain saturation.

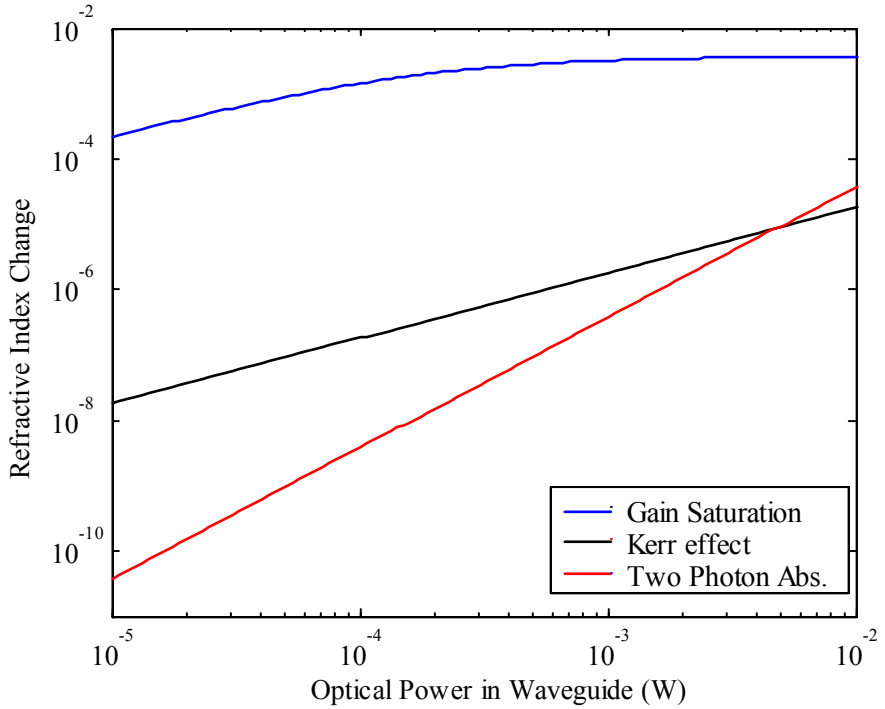

Figure 2.1 Plot of the refractive index change as a function of optical intensity in an InP/InGaAsP waveguide for different non-linear optical processes.

Parameter Name	Value, Reference
Waveguide area (A_{eff})	0.5 μm x 0.5 μm
Kerr index coefficient (n_2)	-4.5 x 10^{-12} cm^2/W [2]
Refractive volume (σ_n)	10^{-20} cm^3 [3]
TPA absorption coeff. (α_2)	60 x 10^{-9} cm/W [7]
Carrier lifetime (τ_c)	1 ns
Wavelength (λ)	1.55 x 10^{-4} cm
Gain coefficient (a_g)	2 x 10^{-15} cm^2
Unsaturated gain (g_0)	2000 cm^{-1}
QW – optical mode overlap (Γ)	0.05
Henry alpha factor (α_H)	3

Table 2.1 Values of parameters used in calculating the non-linear refractive index change. Values without references are typical for the InP/InGaAsP system.

2.7 Optical Non-linearity Enhancement in Microresonators

In the previous sections, I derived the expressions for various non-linear effects as a function of intensity. One common characteristic among them is that refractive index change increases monotonically with incident intensity. A simple way to increase intensity for a fixed input optical power is through the use of resonators. In a resonator, the steady state optical intensity can be made many times higher than the input thus enhancing the non-linear effects of the medium placed inside the resonator. However, this intensity enhancement involves a trade-off in the range of frequencies (or bandwidth) that can pass through the resonator. Since most optical switching and transmission is done over a single or narrow band of frequencies, the use of resonators is attractive for such enhancement. The effect of the reduced bandwidth is to lower the maximum speed of modulation on the carrier optical signal that passes through the resonator. If a monochromatic carrier signal is modulated, it acquires a finite non-zero line-width that is proportionate to the modulation frequency. Thus, when such a modulated carrier signal passes through a finite bandwidth device, the higher frequency components are attenuated much more than the lower frequency ones and the net result is loss of information at the higher frequencies. An equivalent way of looking at it is the effect of photon cavity lifetime. The higher the intensity enhancement inside a resonator, the longer the photon is retained inside the cavity. This is due to the fact that the optical intensity needs to build up over a longer time to reach a higher intensity. The effect of this is to 'smear' out any fast temporal variations in the incident wave over the cavity lifetime of the photon.

2.7.1 Quantifying resonant enhancement of optical non-linearity – small-signal analysis

In this section, I will examine the effect of placing a non-linear medium within a

microring resonator. The goal is to quantify the non-linearity enhancement that is obtained as result.

One way of quantifying is to examine the small-signal variation in net phase with input power:

$$\mathrm{X}(\phi_0, P_{in}) = \frac{d\Phi(\phi_0, P_{in})}{dP_{in}} \tag{2.30}$$

Here $\Phi(\varphi_0, P_{in})$ is the net phase response (eqn. 1.19), P_{in} is the input intensity and φ_0 is the initial round-trip phase detuning from resonance. To calculate this quantity, it is useful to split it into its component contributions:

$$\frac{d\Phi}{dP_{in}} = \frac{d\Phi}{d\phi} \cdot \frac{d\phi}{dI_R} \cdot \frac{dI_R}{dP_{in}} \cdot \tag{2.31}$$

In the expression above, the first and last terms in the product are a function of the resonator properties alone and are not dependent on the non-linearity of the medium. The middle term characterizes the non-linearity of the medium in the resonator. Note that the net rate of change of phase with input power is a function of the initial detuning from resonance as well as the absolute value of the incident optical power. Hence, these need to be taken into account when comparing different cases.

The first term can be evaluated simply by differentiating eqn. 1.19 with respect to the round trip phase. For the sake of simplicity, the resonator is assumed to be gain/loss free ($a = 1$). Thus,

$$\frac{d\Phi}{d\phi} = \frac{(1-\tau^2)\sec^2\phi}{(1-\tau)^2 + (1+\tau)^2 \tan^2\phi} \tag{2.32}$$

Ideally, we want to maximize this quantity, so as to get the most change in transmission

for a small change in input power. This happens when φ = 0, i.e. when the input wavelength is tuned to the resonance. Thus,

$$\left.\frac{d\Phi}{d\phi}\right|_{\max} = \frac{1+\tau}{1-\tau} \tag{2.33}$$

The last term in eqn. 2.31 is obtained by differentiating eqn. 1.13 with respect to input intensity. Again, assuming a = 1 and φ = 0 (maxima),

$$\frac{dI_R}{dP_{in}} = \frac{1}{A_{eff}} \cdot \left.\frac{\kappa^2}{1+a^2\tau^2-2a\tau\cos\phi}\right|_{a=1,\phi=0} = \frac{1}{A_{eff}} \cdot \frac{1+\tau}{1-\tau} \tag{2.34}$$

The second term in eqn. 2.31 is the intensity induced round-trip phase change and is given by:

$$\frac{d\phi}{dI_R} = \frac{2\pi L}{\lambda} \cdot \frac{dn(I_R)}{dI_R} \tag{2.35}$$

Putting it all together, the net small-signal rate of change of phase for a microring resonator is given by:

$$\left.\frac{d\Phi}{dP_{in}}\right|_{Ring} = \frac{1}{A_{eff}} \cdot \frac{(1+\tau)^2}{(1-\tau)^2} \cdot \frac{2\pi L}{\lambda} \cdot \frac{dn(I_R)}{dI_R} \tag{2.36}$$

This is a very significant result in that it illustrates the 'amplifying' effect of the resonator on the non-linearity. Comparing with an equivalent length of waveguide, the effective phase change is given by:

$$\left.\frac{d\Phi}{dP_{in}}\right|_{WG} = \frac{1}{A_{eff}} \cdot \frac{2\pi L}{\lambda} \cdot \frac{dn(I_{WG})}{dI_{WG}} \tag{2.37}$$

Thus the effect of the resonator is to enhance the non-linear phase change by a

magnifying factor M given by:

$$M = \left.\frac{(1+\tau)^2}{(1-\tau)^2}\right|_{\tau\approx 1} \approx \left(\frac{F}{\pi}\right)^2 \tag{2.38}$$

Here, F is the finesse of the resonator and the coefficient τ is assumed to be close to unity. An equivalent small-signal analysis can be done using the transmission coefficient, defined as the ratio of output to input intensity, instead of the net phase change as done here and will yield the same result [72].

2.7.2 Quantifying resonance enhancement of optical non-linearity – the large signal case

In the small signal approximation discussed above, it was assumed that the phase excursion due to intensity induced index change is very small and hence the detuning from resonance is nearly zero ($\varphi \sim 0$) throughout the process. In other words, the wavelength is always positioned at the best spot for producing the maximum change in output. However, in switching applications, this is never true as the output needs to change from zero to a large value or vice versa for maximum contrast. To see how this occurs consider the case when the input intensity gradually increases from zero to a large value. Assume that the wavelength of the incident beam is initially tuned exactly to the resonance. i.e. $\varphi = 0$. As the intensity increases, initially the field enhancement in the ring is given by $FE = \kappa/1-\tau$. The increasing intensity results in a non-linear phase shift and takes the operating point away from the $\varphi = 0$ condition. Thus, the resonance moves away from the initial location and the field enhancement is reduced at high intensities to $FE = \kappa/\left|1-\tau\exp(-j\phi)\right|$, where φ is the intensity induced phase-shift.

To model the large-signal characteristics, consider the ring intensity relations from eqns. 1.13 and 1.16 reproduced here for convenience.

$$I_R = I_{in} \cdot \frac{\kappa^2}{1 + a^2\tau^2 - 2a\tau\cos\phi} \tag{2.39}$$

$$I_t = I_{in} \cdot \frac{\tau^2 + a^2 - 2a\tau\cos\phi}{1 + a^2\tau^2 - 2a\tau\cos\phi} \tag{2.40}$$

The round-trip phase is now a function of the intensity in the ring:

$$\phi = \phi_0 + \frac{2\pi}{\lambda} L\Gamma\Delta n(I_R) \tag{2.41}$$

Here φ_0 is the unperturbed or initial phase, and $\Delta n(I_R)$ is the intensity induced index change and is determined by one of the following:

$$\Delta n(I) \quad \begin{cases} = n_2 I & \text{Kerr Effect} \\ = -\dfrac{\sigma_n \alpha_2 \tau_c I^2}{2\hbar\omega} & \text{Two Photon Abs.} \\ = \dfrac{\alpha_H \lambda g_0}{4\pi} \cdot \dfrac{\overline{I}}{1 + \dfrac{\overline{I}}{I_{sat}}} & \text{Gain Saturation} \end{cases} \tag{2.42}$$

Eqns. 2.39 through 2.42 form a system of non-linear equations that can be solved for the through-port intensity as a function of the input intensity. Figures 2.2 and 2.3 show the results of the simulation for the case of gain saturation based on the above set of equations. The parameters used in the simulation are as indicated in table 2.2. For the sake of simplicity, the round-trip gain (a) is assumed to be constant. In reality, the round-trip gain goes down with intensity due to saturation. The initial round-trip phase detuning from resonance (φ_0) is varied on both sides of the resonance.

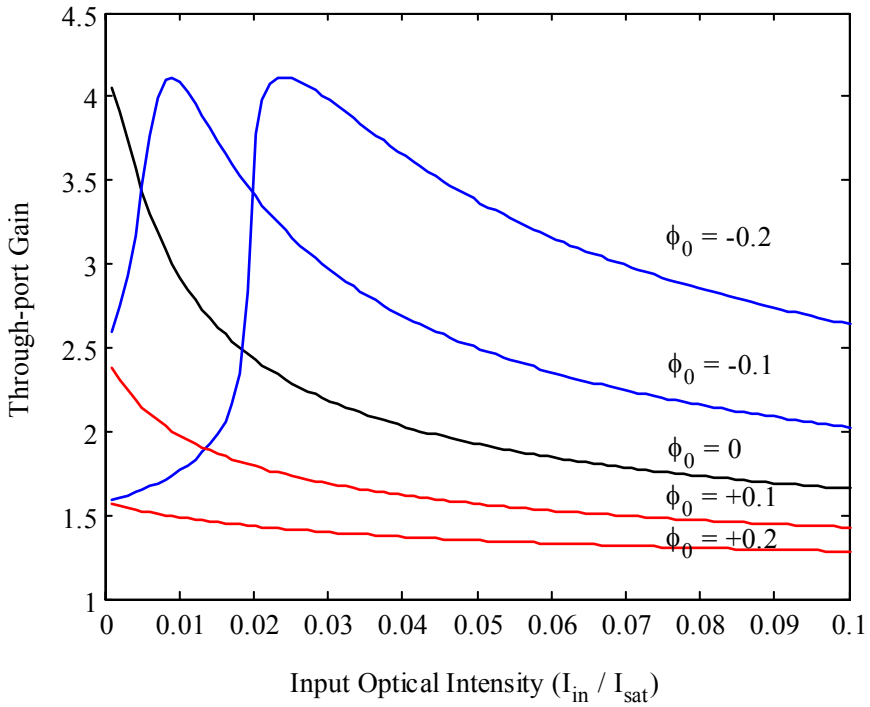

Figure 2.2 Through-port response of microring resonator as a function of input intensity (normalized to I_{sat}) for the case of gain-saturation. The detuning parameter (φ_0) is varied on both sides of the resonance.

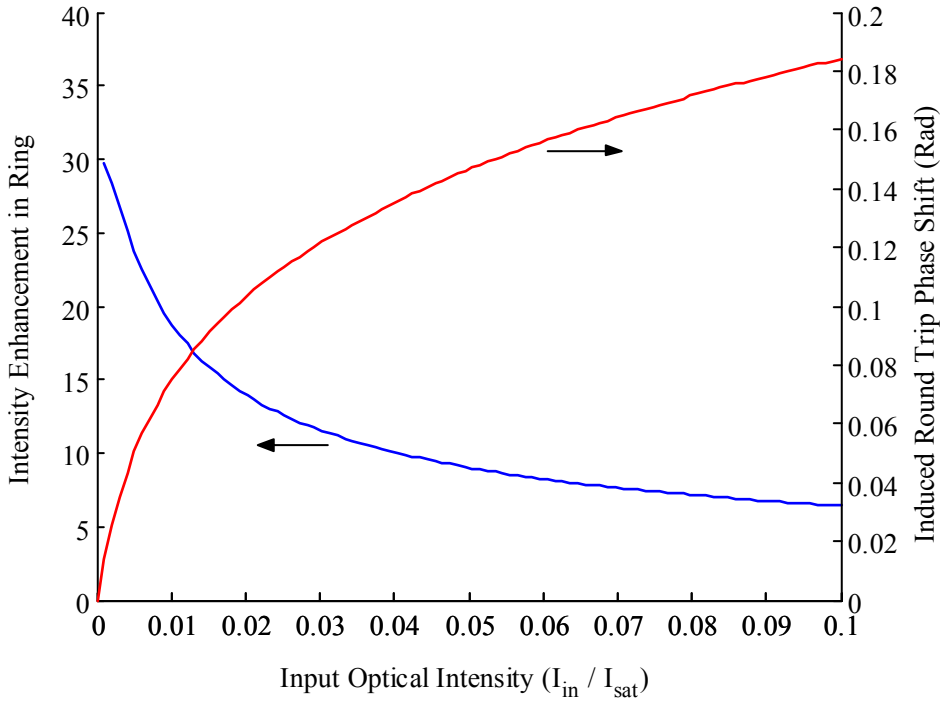

Figure 2.3 Intensity enhancement in the ring and round-trip phase change due to gain-saturation non-linearity for the case when the wavelength is tuned to the resonance peak initially ($\varphi_0 = 0$).

Parameter, Symbol	Value
Ring radius (R)	10 μm
Coupling coefficient (κ)	0.5
Round-trip gain (a)	1.05
Unsaturated gain (g_0)	1000
QW – optical mode overlap	0.05
Henry alpha factor (α_H)	3

Table 2.2 Values of parameters used in the large-signal non-linear characteristics calculation shown in figures 2.2 and 2.3.

Figure 2.2 is a plot of the through-port response (I_{out} / I_{in}) as a function of input intensity. The input intensity is normalized to the saturation intensity (I_{in} / I_{sat}). In the absence of any non-linearity, all curves would have remained flat as the intensity was varied. The $\varphi_0 = 0$ case (black curve) corresponds to the case when the wavelength is tuned exactly to the resonance. As the intensity increases, the resonance moves to longer wavelengths corresponding to a decreasing refractive index and consequently the net gain drops. If the starting point is red-detuned initially ($\varphi_0 < 0$), then the induced refractive index change causes the resonance to move towards the operating wavelength and eventually move past the peak. This results in a response indicated by the blue curves in figure 2.2. Conversely, if the starting point is blue-detuned, then the resonance moves farther away as the intensity increases resulting in very low gain. This results in a response indicated by the red curves in the figure. Figure 2.3 shows the intensity induced round-trip phase change (red-curve) and intensity enhancement (blue-curve) within the resonator as a function of input intensity for case when $\varphi_0 = 0$.

Chapter 3

DESIGN AND FABRICATION

In this chapter I will present details of the optical and epitaxial design followed by the fabrication process. The devices were based on the InP/InGaAsP system to enable operation at communication wavelengths i.e. the 1550 nm band. The first few batches of devices were based on the vertical coupling scheme primarily for two advantages: The rings can be made using the active layers while the bus waveguides that transport light between rings can be made passive. Also, the coupling strength between ring and bus can be controlled precisely by the epitaxial thickness of the middle layer.

3.1 Optical Design of the Vertical Coupling Scheme

A schematic cross-section of the vertical coupling structure is shown in figure 3.1. It shows the ring waveguide on top of the bus waveguide separated by a middle layer. The primary optical design criteria for this structure were:

- Single-mode operation.
- Minimal radiation losses to bending in the ring waveguide.
- Minimal loss to absorption in electrical contacts.
- Maximum coupling between ring and bus waveguides.

Additionally, achieving these design objectives were subject to constraints imposed by the difficulty of fabrication or desired electrical and thermal properties of the device. The

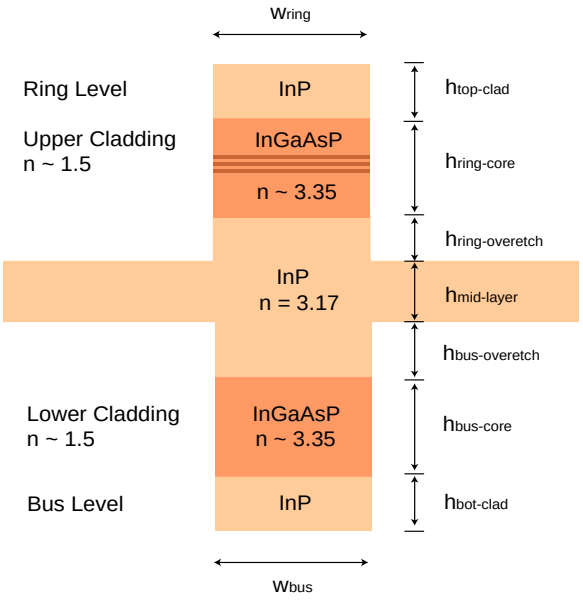

Figure 3.1: Cross-section of a vertically coupled ring-resonator fabricated in the InP/InGaAsP system.

optical behavior of the waveguides was evaluated by numerically solving the wave-equation in terms of the transverse electric fields on a 2-D grid. The numerical simulations were carried out using the commercially available software OWMS [73].

3.1.1 Single mode operation

Single mode operation is desirable to ensure predictability of behavior, especially coupling between ring and bus, as well as the resonances in the ring. Single mode behavior is also desirable to cut down losses in the waveguide as the higher order modes overlap with the etched surface more than the fundamental mode. Also, modal dispersion due to higher order modes results in pulse distortion. In the growth direction, single mode operation is fairly easy to achieve due to the low index contrast between core (n_{core} ~ 3.35) and cladding (n_{clad} ~ 3.17). However, in the lateral direction the strong index contrast ($n_{core} - n_{clad}$ ~ 1.8) results in a large normalized frequency for the waveguide and

hence very narrow waveguides are necessary to bring the normalized frequency down and 'squeeze' out the higher order modes. The transition from single to multi-mode behavior in the lateral direction occurs at a waveguide width of approximately 0.4 μm. This is just beyond the resolution capabilities (~ 0.5 μm) of the projection aligner used to define the waveguides lithographically. Figure 3.2 shows the supported modes for increasing waveguide widths. The mode nomenclature is of the form $E_{mn}^{x/y}$, where the superscript denotes the polarization and the subscript denotes the number of peaks in the X and Y directions. Fortunately, we can relax the requirement from strict single-mode behavior to allow for a few additional modes. This is because there is no coupling of power between (1) the first mode (E_{11}^{x}) and the next higher mode (E_{21}^{x}) as the overlap integral between them is zero and (2) cross-polarized modes (E_{11}^{x} and E_{11}^{y}). The primary mode of interest is E_{11}^{x} as interaction with quantum wells in the core of the ring is stronger for polarization in the plane of the quantum well. Thus, horizontally polarized light from a single mode fiber aligned to the center of the waveguide facet is expected to mostly feed into the E_{11}^{x} mode and very little power if any should couple into the other modes. The waveguide width was thus selected to be between 0.8 μm and 1.0 μm to ensure ease of fabrication as well as provide effectively single mode behavior.

A key consideration in most semiconductor waveguide based devices is the polarization dependence of device characteristics. I will discuss this briefly in the context of active microring devices in a later section. While coupling between cross polarized modes is not a concern in straight waveguides, there is some amount of polarization conversion in curved waveguides [74]. Consequently, the resonance spectrum of microrings contains features arising from coupling to the cross–polarized mode. The

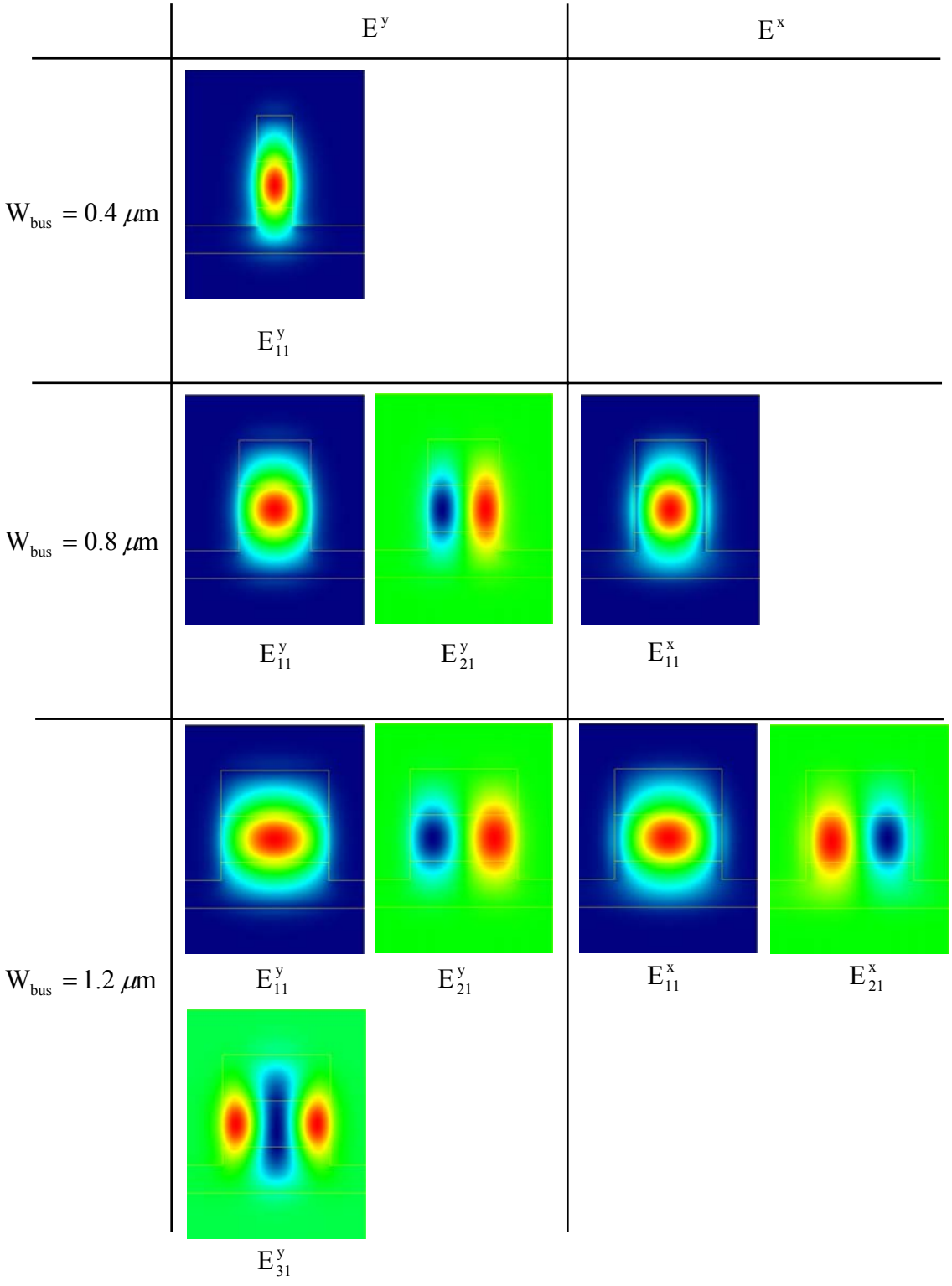

Figure 3.2: Optical mode profiles for increasing waveguide widths. The left column is for the Y-polarized modes and the right column is the X-polarized modes.

cross-polarized mode has a different propagation constant and hence different resonance wavelengths.

3.1.2 Radiation loss in microrings and disks

Curved optical waveguides can be analyzed by the method of conformal transformation [46]. In this method, the coordinate system is transformed from the X-Y plane to the U-V plane according to the relation:

$$W = u + iv = f(Z = x + iy) \tag{3.1}$$

The ring is co-planar with the X-Y plane. The function $f(z)$ is chosen so as to convert curved boundaries in the X-Y plane to straight ones in the U-V plane. The result of this transformation is to modify the 2-D scalar wave-equation to an equivalent one in the U-V plane.

$$[\nabla^2_{x,y} + k^2(x,y)]\psi = 0 \overset{f(z)}{\rightarrow} [\nabla^2_{u,v} + \left|\frac{dZ}{dW}\right|^2 k^2(u,v)]\psi = 0 \tag{3.2}$$

The refractive index too undergoes the transformation:

$$n(x,y) \overset{\text{f(z)}}{\rightarrow} n(u,v) \tag{3.3}$$

For the case of a circular waveguide in the X-Y plane such as a ring, a suitable transformation function $f(z)$ is:

$$W = R_2 \ln\frac{Z}{R_2} \tag{3.4}$$

Here, R_2 and R_1 are the outer and inner radius of the microring respectively. The effect of this transformation is illustrated in figure 3.3. Figure 3.3(a) shows the new boundaries in

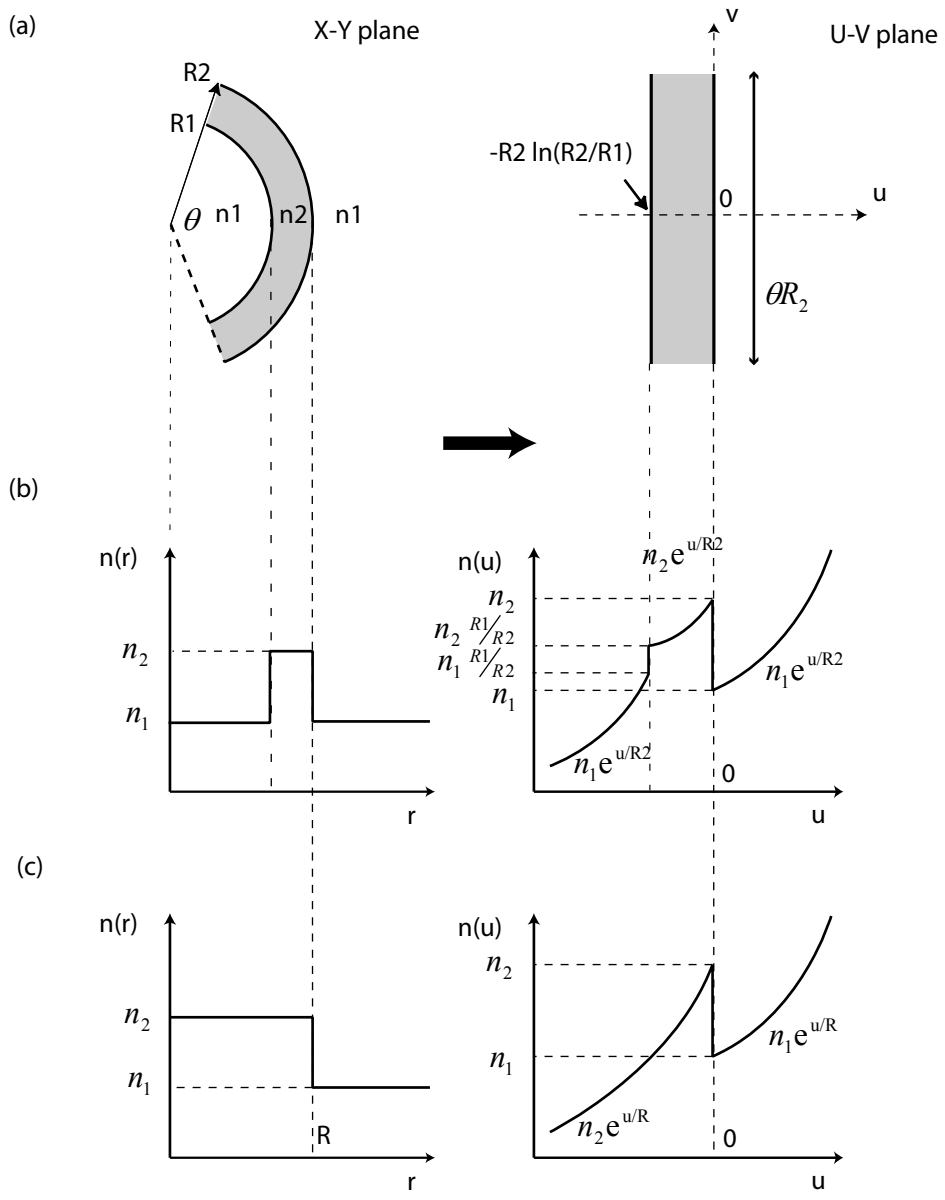

Figure 3.3: (a) Transformation of geometry of microring from X-Y to the U-V plane (b) Transformation of refractive index profile of ring (c) Transformation of refractive index profile for a microdisk.

the U-V plane. The outer wall is at $u = 0$ and the inner wall at $u = -R_2 \ln(R_2/R_1)$. Thus, the problem now reduces to solving the wave-equation for a simple planar waveguide in the U-V plane. Figure 3.3(b) shows index profile in the X-Y plane along the radial direction and the corresponding profile in the U-V plane along the u-direction. Figure 3.3(c) shows the index profile for a microdisk resonator.

Two very interesting things can be observed in the index diagrams. One is that the index increases exponentially along the u-direction outside the ring. Thus, light can couple from the confined modes in the slab-waveguide structure (U-V plane) to freely radiating modes in the high-index semi-infinite region to the right. This accounts for the loss seen in bending waveguides. The gap between the slab-waveguide and the semi-infinite high index region to the right is determined by the radius of the ring and decreases with the radius. Thus, tightly bent waveguides have higher radiation losses. The other interesting point to note is the index profile in the U-V plane for the microdisk resonator. The microdisk index profile is seen to form a local maxima near $u = 0$ even though there is no confining wall or index step towards the center of the disk. Thus wave-guiding can occur along the periphery of the disk in the absence of any inner wall.

The bending loss analysis and design was carried out using the commercially available software OWMS [73]. For the range of radii used in these devices (5 to 20 μm), the index contrast between semiconductor and polymer ($\Delta n \sim 1.8$) is well above sufficient to prevent radiation losses directly from the semiconductor to the polymer. However, the presence of the high index middle layer close to the ring core, which extends in the ring plane beyond the outer wall, presents a path for light to couple from the ring to the slab waveguide modes in this layer. This is illustrated in figure 3.4(a), which shows the

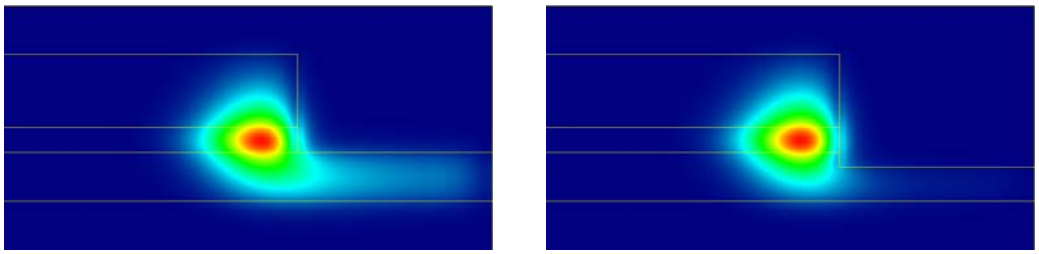

(a)

$n = 3.067 - i0.00167$

$\alpha_{bend} = 131\ cm^{-1}$

(b)

$n = 3.059 - i0.00014$

$\alpha_{bend} = 11\ cm^{-1}$

Figure 3.4: Simulation of optical mode intensity distribution and bending loss in a microdisk of radius 10 μm for varying etch depths (a) $h_{ring\text{-}overetch} = 0$ (b) $h_{ring\text{-}overetch} = 200$ nm. The thickness of the middle layer before etch is the same in both cases ($h_{mid\text{-}layer} = 500$ nm).

optical mode pattern for the case when the microdisk is etched only to the boundary of the middle layer. The radiation loss to the middle layer can be minimized by etching below the ring core – middle layer boundary ($h_{ring\text{-}overetch}$ in figure 3.1). However, this has to be balanced against a higher electrical resistance and accompanying heating effects as the middle layer also forms the current conduction path between the N-contact and disk/ring. Figure 3.4(b) shows the optimized structure, which minimizes this bending loss while maintaining a sufficiently thick middle layer for conduction. Another option would have been to increase the thickness of the middle layer and etch the rings deeper but this results in the distance between the bus and ring cores increasing and hence coupling decreases significantly.

3.1.3 Absorption loss in contact layer

A 200 nm InGaAs ternary layer is used to form the p-contact layer at the top of the ring. To ensure an ohmic contact, a small band-gap material such as the InGaAs

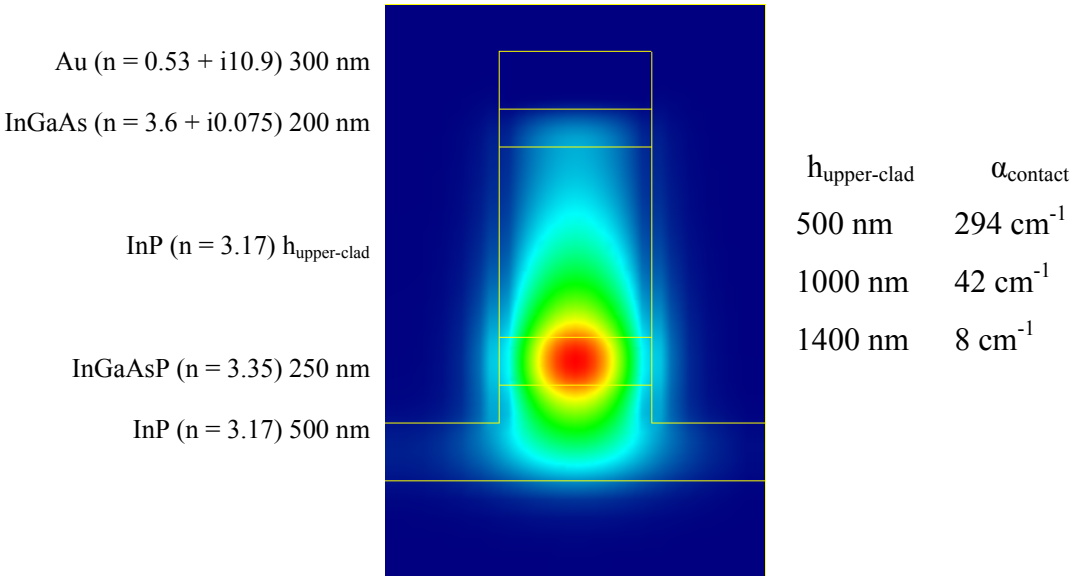

Figure 3.5: Absorption loss in contact layers (InGaAs and Au) is determined by thickness of intervening InP upper-clad layer. Table shows the calculated loss for increasing thickness of the upper-clad layer.

ternary is necessary. However, if this layer is very close to the ring-core, there is increased optical loss due to absorption in the ternary layer. Figure 3.5 shows the calculated loss for increasing distance between the core and contact layers. An optimum thickness would be one that minimizes the optical loss as well as keeps the etch-depth required to a minimum and is around 1.4 μm for the geometry and material system used in these devices.

3.1.4 Coupling strength estimation

The fraction of power that couples from the bus wave-guide to the ring/disk is determined by the coupling constant κ. The coupling constant has a very strong influence on the ring-resonator characteristics and hence being able to design a device for a particular coupling is critical to achieve the desired switching behavior.

This section deals with the numerical estimation of the coupling constant by calculating the overlap between optical modes of the bus and ring waveguides. The calculation can be split into two components. In the first part, I estimate the coupling between two straight parallel waveguides assuming weak coupling. The second part deals with extending the calculation to determine the total coupling between two arbitrarily curved waveguides.

Following coupled-mode theory as described in ref. [43], the intensity in two weakly coupled parallel waveguides aligned in the z-direction can be written as:

$$\begin{aligned} \frac{d\Psi_1}{dz} &= -j\beta_1\Psi_1 - jc_2\Psi_2 \\ \frac{d\Psi_2}{dz} &= -j\beta_2\Psi_2 - jc_1\Psi_1 \end{aligned} \tag{3.5}$$

Here, Ψ_1 and Ψ_2 represent the contribution of the individual waveguide modes to the combined mode, which is assumed to be of the form:

$$\overline{E}_{12}(x,y,z) = \Psi_1(z)\overline{E}_1(x,y) + \Psi_2(z)\overline{E}_2(x,y) \tag{3.6}$$

The coupling constant c_q is defined as:

$$c_q = \frac{\omega\varepsilon_0}{4}\iint\left[n_{pq}^2(x,y) - n_q^2(x,y)\right]\overline{E}_p^*(x,y)\cdot\overline{E}_q(x,y)dxdy \tag{3.7}$$

Here, n_{pq} is the refractive index distribution with both the waveguides present and n_q is the refractive index distribution with only waveguide q present. The electric-fields are normalized such that there is unit power flowing in the z-direction, i.e.

$$\frac{1}{2}\iint\hat{z}\cdot(\overline{E}_p^*\otimes\overline{H}_p)dxdy = 1 \tag{3.8}$$

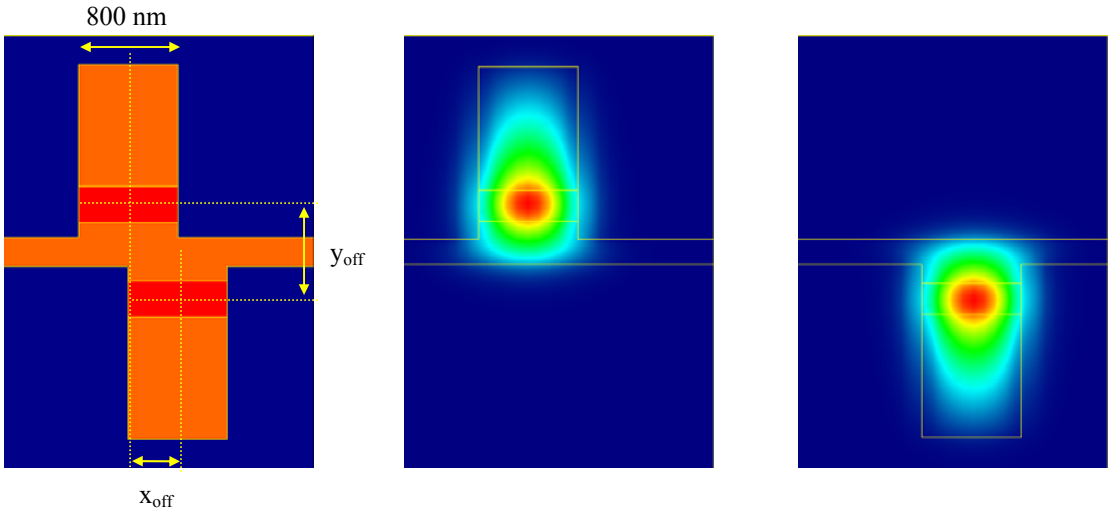

Figure 3.6: Coupling calculation (a) schematic showing ring (top) and bus (bottom) waveguides with relevant offsets as indicated. (b) and (c) show the optical mode intensity distribution for the individual waveguides used in the overlap integral calculation.

The coupling coefficient can be calculated numerically as defined in eqn. 3.7. The optical modes ($\mathbf{E_p}$ and $\mathbf{E_q}$) for the individual waveguides are determined using the OWMS mode solver. A MATLAB [75] script (software supplement A) then reads in the output from the solver and calculates the coupling coefficient as indicated above. Figure 3.6 shows the structure used in the calculation as well as the optical modes for the individual waveguides in a vertically coupled scheme. The coupling is expected to fall exponentially with waveguide separation since the optical intensity drops exponentially outside the core. The coupling constant is calculated for two different offsets of the bus-waveguide and is fitted to a function of the form

$$c_0(x_{off}, y_{off}) = a_1 \exp\left(-a_2\sqrt{x_{off}^2 + y_{off}^2}\right) \tag{3.9}$$

For the structure shown in figure 3.6, the waveguide widths are 0.8 μm and the x-offsets were chosen as 0 and 400 nm. The y-offset is determined by the epitaxial thickness and is equal to 750 nm. The coupling constant was calculated to be

$$c_0 = 5.611\times10^6 \exp\left(-5.316\times10^6 \sqrt{x_{off}^2 + y_{off}^2}\right) \text{ m}^{-1} \tag{3.10}$$

The coupling coefficient derived by this method is useful for analyzing parallel waveguides. However, it needs to be modified for use in non-parallel and/or curved waveguides such as in microrings, where the bus waveguide approaches tangentially to the circular ring waveguide. I follow the method of ref. [1] to calculate the coupling between curved waveguides.

Consider the case of coupling between a curved and straight waveguide as shown in figure 3.7. Strictly speaking, the incremental change in electric field at point t_1 has a contribution from all-points on waveguide-2. However, as an approximation, the field at point t_1 can be considered to be affected by contributions only from a single point t_2 on waveguide-2, where the point t_2 is chosen such that the tangents to the waveguides at t_1 and t_2 subtend equal angles with the line connecting them. The modified version of the coupled-mode equations (eqn. 3.5) is given by:

$$\begin{aligned} \frac{d\Psi_1(t_1)}{dt_1} &= -j\beta_1\Psi_1(t_1) - jc_1\Psi_2(t_2) \\ \frac{d\Psi_2(t_2)}{dt_2} &= -j\beta_2\Psi_2(t_2) - jc_2\Psi_1(t_1) \end{aligned} \tag{3.11}$$

Here t_1 and t_2 are the parametric-coordinates for the corresponding waveguides and are related to each other by the constraint mentioned above and defined by the shape-function:

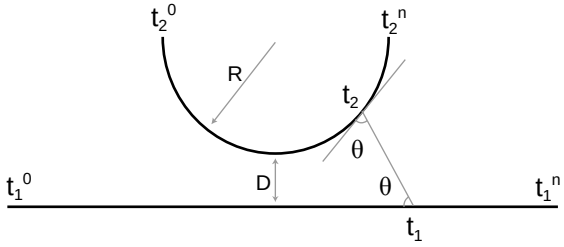

Figure 3.7: Schematic showing coupling between a curved and straight waveguide.

$$t_2 = f_{sh}(t_1) \tag{3.12}$$

The coupling coefficients c_1 and c_2 are related to each other and to the coupling coefficient for the case of straight waveguides (c_0) as

$$\begin{aligned} c_1 &= c_2 \cdot \frac{dt_2}{dt_1} \\ c_1 &= c_0 \cos(\pi - 2\theta) \cdot \left(\frac{dt_2}{dt_1} \right)^{1/2} \\ c_2 &= c_0 \cos(\pi - 2\theta) \cdot \left(\frac{dt_1}{dt_2} \right)^{1/2} \end{aligned} \tag{3.13}$$

The variation of Ψ_q along t_q can be separated into the phase and amplitude parts as:

$$\Psi_q(t_q) = \psi_q(t_q) \exp(-\beta_q t_q) \tag{3.14}$$

Substituting this in the coupled mode equations (eqn. 3.11) results in a pair of coupled equations.

$$\frac{d^2\psi_q}{dt_q^2} + j2B_q \frac{d\psi_q}{dt_q} + C_q^2 \psi_q = 0 \ ; \ q = 1,2 \tag{3.15}$$

The coefficients (B_q, C_q) of the differential equations are given by:

$$B_q = \frac{1}{2}\left[\left(\beta_p \frac{dt_p}{dt_q} - \beta_q\right) + j\frac{1}{c_q}\frac{dc_q}{dt_q}\right]$$
$$C_q = \left[c_p c_q \frac{dt_p}{dt_q}\right]^{1/2} \tag{3.16}$$

The differential equation coefficients defined above are not constant and hence a transmission matrix approach is adopted, where the equations are solved for a small stretch of the waveguides. The coefficients are assumed to be piece-wise constant over these small stretches. Thus, for a small section of the waveguides from t_q^{k-1} to t_q^{k}, the amplitudes at either end can be written as:

$$\begin{bmatrix}\psi_1(t_1^k)\\ \psi_2(t_2^k)\end{bmatrix} = \begin{bmatrix} b_{11}(t_1^k, t_1^{k-1}) & jb_{12}(t_1^k, t_1^{k-1}) \\ b_{21}(t_2^k, t_2^{k-1}) & b_{22}(t_2^k, t_2^{k-1})\end{bmatrix} . \begin{bmatrix}\psi_1(t_1^{k-1})\\ \psi_2(t_2^{k-1})\end{bmatrix} \tag{3.17}$$

Here, the matrix coefficients b_{ij} are determined by the solutions to the differential equations above (eqn. 3.15) over the interval [t_q^{k-1}, t_q^{k}]. The net response is then calculated by the multiplication of these matrices over the entire length of the waveguides.

$$\begin{bmatrix}\psi_1(t_1^n)\\ \psi_2(t_2^n)\end{bmatrix} = \prod_{k=1}^{n}\begin{bmatrix} b_{11}(t_1^k, t_1^{k-1}) & jb_{12}(t_1^k, t_1^{k-1}) \\ b_{21}(t_2^k, t_2^{k-1}) & b_{22}(t_2^k, t_2^{k-1})\end{bmatrix} . \begin{bmatrix}\psi_1(t_1^0)\\ \psi_2(t_2^0)\end{bmatrix} \tag{3.18}$$

The method described here was implemented numerically using a MATLAB script (software supplement B). Figure 3.8 shows the calculated net coupling coefficient (κ) as a function of the horizontal gap between bus and ring-waveguides for the structure shown in fig. 3.6. The ring radius is assumed to be 10 μm.

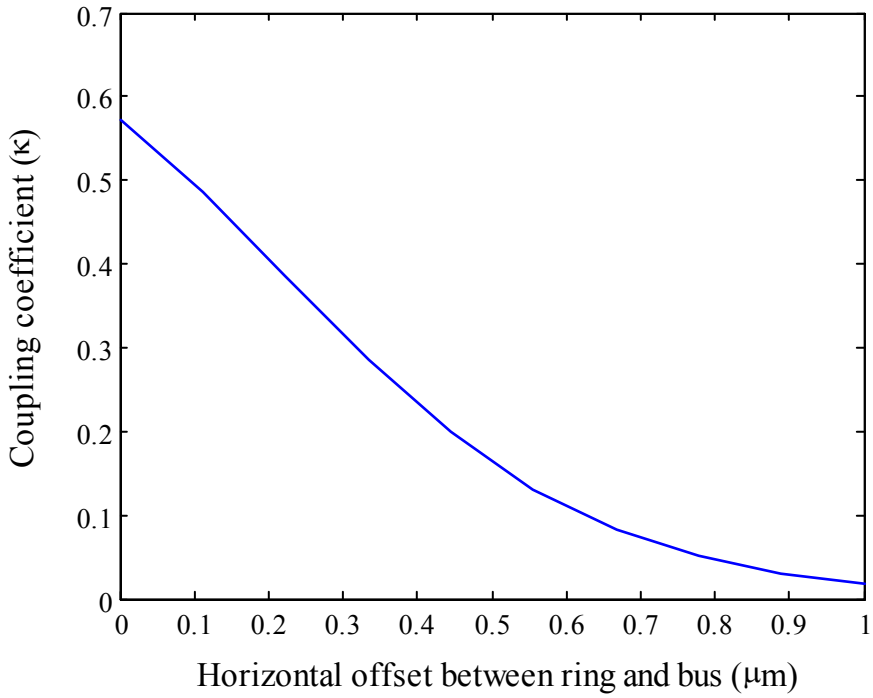

Figure 3.8: Coupling strength between a microring (R = 10 μm) and vertically coupled bus waveguide as a function of the horizontal offset (x_{off}) between them calculated using the method in reference [1].

3.2 Epitaxy Design and Growth

The epitaxial layer structure used for the vertically coupled active microrings and disks is shown in fig. 3.9. The layer structure is inverted from the final orientation to allow for flip bonding of the epi-layers to a carrier substrate. The epitaxial growth (# g564a) was carried out in a solid-source MBE machine at the Laboratory for Physical Sciences, College Park. I am grateful to Dr. S. Kanakaraju and Dr. C. Richardson for the MBE growth.

After wafer cleaning, preparation and loading, the growth begins with a short buffer layer of InP that acts as the starter layer. Following this, a 200 nm thick heavily p-

	500 nm InP		Undoped	Lower Clad n = 3.17
Bus Core	10 nm InP	**x 5**	Undoped	
	40 nm $Ga_{0.27}In_{0.73}As_{0.57}P_{0.43}$		Undoped	λ_g = 1.25-1.30 um n = 3.38
Coupling Layer	300 nm InP		$n^+ = 5 \times 10^{18}$ cm^{-3}	N-Contact
	200 nm InP		$n = 5 \times 10^{17}$ cm^{-3}	Mid Clad
Ring Core	65 nm $Ga_{0.27}In_{0.73}As_{0.57}P_{0.43}$		Undoped	Shoulder
	10 nm $Ga_{0.27}In_{0.73}As_{0.57}P_{0.43}$	**x 5**	Undoped	Q-Barrier
	10 nm $Ga_{0.27}In_{0.73}As_{0.80}P_{0.20}$		Undoped	Q-Well λ_g = 1.55 um
	75 nm $Ga_{0.27}In_{0.73}As_{0.57}P_{0.43}$		Undoped	Shoulder
	1400 nm InP		$p = 5 \times 10^{17}$ cm^{-3}	Upper Clad
	200 nm $Ga_{0.47}In_{0.53}As$		$p^+ = 1 \times 10^{19}$ cm^{-3}	P-Contact
	300 nm InP			Buffer
	2"/3" InP Substrate			Substrate

Figure 3.9: Epitaxial layer structure used for the vertically coupled active microring devices.

doped layer of lattice matched InGaAs ternary is added. The InGaAs layer serves two vital purposes; the first is to form the small band-gap contact layer for the p-contact and

the second is to form the etch-stop layer during wet-etching to remove the substrate. Subsequently, a 1400 nm thick layer of InP is grown, which forms the upper cladding for the ring optical core. The large thickness serves to separate the highly-absorbing InGaAs layer from the ring core. The p-doping is stepped down from 10^{19} cm^{-3} near the contact to $5x10^{17}$ cm^{-3} near the core to minimize free-carrier absorption losses. The ring core is a 240 nm thick undoped InGaAsP quaternary layer with a refractive index of approximately 3.4 and a band-gap wavelength of 1.26 μm. The core serves as both the carrier and optical confinement layer. At the center of the ring-core a set of five compressively-strained quantum wells is used to provide optical gain. Following the core, a 500 nm thick n-doped InP middle-cladding layer is grown. The thickness of this layer determines the coupling strength between the bus and ring waveguides. It also serves as the n-contact layer and hence is doped to about 5 x 10^{18} cm^{-3}. The bus-core comprises alternate layers of InP with InGaAsP quaternary and has a net effective index of about 3.35. A very thick layer of quaternary InGaAsP tends to undergo spinodal decomposition into InAs and GaP during growth and hence needs to be alternated with thin InP layers [76]. The bus core is undoped to minimize free-carrier optical absorption. The last layer is a 500 nm undoped InP cladding layer for the bus waveguide.

3.3 Fabrication

In this section, I outline the fabrication procedure for the vertically-coupled active microrings and disks. The process recipes used are described in detail in appendix A. The process steps are illustrated in fig 3.10. Fabrication starts with cleaving a 15 mm x 15 mm coupon from a 2-inch wafer with epitaxial structure as described above. The wafer-piece is cleaned with acetone, methanol and iso-propanol rinses successively, followed by a

nitrogen blow dry.

3.3.1 Etch-mask deposition

A 300 nm layer of silicon dioxide (SiO_2) is deposited in an HDPECVD system at 120 °C using silane (SiH_4) and nitrous oxide (N_2O) as the precursor gases. Prior to the deposition, the wafer-piece is treated for 1 minute in ammonia (NH_3) plasma to enhance adhesion of the silicon dioxide to indium phosphide. The layer is used as the etch-mask for plasma etching bus-waveguides in the indium phosphide below.

3.3.2 Bus-waveguide lithography

A 1500 nm thick layer of positive photoresist (OiR 906-10) is spun on the silicon-dioxide coated wafer-piece and baked. It is then aligned and exposed on a 5x projection aligner with the bus level photo-mask. Following exposure, it is hard-baked and developed to form the photo-resist pattern.

3.3.3 Pattern transfer to etch-mask layer

The photo-resist pattern is transferred to the silicon dioxide layer by plasma etching in a reactive-ion etcher (RIE). Prior to the etch, a 15 second oxygen plasma clean is used to remove photoresist residue in the exposed areas. The silicon dioxide etch has marginal selectivity over photo-resist but the large thickness of photo-resist compared to silicon dioxide compensates for the lack of selectivity. The etch is continued for about 2 minutes beyond the end-point to ensure complete removal of silicon-dioxide in the unmasked areas. Following the etch, the photoresist is removed by oxygen plasma ‘ashing’ and acetone rinse.

3.3.4 Bus-waveguide etching

The bus waveguides are etched into the indium-phosphide in the RIE system using the silicon-dioxide pattern as the etch-mask [77, 78]. The etch process is a two step scheme. The first step is a 5 minute InP etch in a methane (CH_4), hydrogen (H_2) and argon (Ar) plasma. The use of a carbon containing gas results in polymerization reactions in the plasma and the chamber and wafer-piece is covered by a thin layer of long-chain hydrocarbons. This polymer layer serves to passivate the side-walls preventing under-cutting and results in vertical side-walls. However, the reaction on the horizontal surfaces is driven by ion bombardment and indium phosphide continues to etch by formation of volatile organo-metallic group-III compounds ($In\text{-}C_xH_y$) and PH_3. The second step is a 3 minute oxygen plasma process, which removes the excessive build-up of polymer. These two steps are repeated as often as necessary to achieve the desired etch-depth. The bus-waveguides are etched to the boundary of the bus core and middle layer. Typical etch rate of indium phosphide is around 50 nm/min while that of the silicon dioxide etch mask is around 1 nm/min. Thus, the etch-selectivity is 50:1 approximately. Following etching, the silicon-dioxide etch cap is removed by a 2 minute dip in buffered hydrofluoric acid (BHF).

3.3.5 Polymer wafer bonding

Accessing the ring-level epi-layers for processing needs the substrate to be removed. However, the epi-layers are very thin (~ 2 μm) to support its own weight. The epi-layers need to be transferred by flip-bonding to a carrier substrate before backside processing can be done. The transfer is accomplished by way of polymer wafer bonding [79].

Benzo-cyclobutene (BCB, Dow Chemical), a low solvent content polymer, is used to carry out the polymer wafer bonding [80-82]. An indium phosphide carrier substrate slightly larger than the epi-substrate is prepared by spinning a layer of BCB-35 along with an adhesion promoter (APS 3000, Dow Chemical) . The epi-surface of the original substrate with the etched bus waveguides is prepared by flooding it with BCB. Both the carrier and original substrate are baked at 90 °C for 15 minutes on a hot-plate to drive out solvents. Following the bake, the wafer pieces are transferred to a 120 °C hot-plate and flip-bonded. Care must be taken to align the crystal axes of the two pieces to ensure good cleaving behavior at the end. Excess BCB is cleaned off by rinsing in a solvent (T-1100, Dow Chemical). At this point, the bonded wafer-pieces can be inspected under an IR microscope for trapped air bubbles. The wafer pieces are then sandwiched between graphite blocks with weights added on top to generate a bond pressure of approximately 1 MPa. The blocks are then placed in an oven in a nitrogen ambient and cured at 220 °C for 2 hrs. Following cool down, the blocks are separated and the bonded wafer-pieces extracted. Typical bond line thickness is around 500 nm for low viscosity BCB (BCB-35).

3.3.6 Substrate removal

The original substrate is removed to expose the back side of the epi-layers. The substrate is thinned from approximately 300 μm to 50 μm by mechanical lapping. The remaining 50 μm is removed by wet-etching in a HCl + H_3PO_4 mixture. The wet etch stops on the InGaAs etch-stop layer. The wafer-piece is then rinsed in DI water and blown dry.

At this point, the wafer-piece consists of thin epi-layers bonded bus-side down to

the carrier substrate using BCB.

3.3.7 Ring etch-mask layer deposition

A 500 nm layer of silicon dioxide is deposited in an HDPECVD system. This layer forms the mask for etching indium phosphide subsequently.

3.3.8 Ring waveguides lithography

Positive photoresist is spun on the wafer-piece and patterned using a projection aligner with the ring level photomask. The procedure is identical to that for the bus waveguides above.

3.3.9 Pattern transfer to etch-mask layer

The photoresist pattern containing rings is transferred to the silicon dioxide layer by plasma-etching in an RIE system using the photoresist as an etch-mask. Following the etch, the photoresist is removed by dissolving it in acetone and by plasma 'ashing'.

3.3.10 Ring etching

Using the silicon dioxide pattern as the etch-mask, the microring side indium phosphide is etched in an RIE system using methane, hydrogen and argon plasma as before. Etching is stopped when the depth reaches about 150 to 200 nm below the ring core – middle layer boundary. Total etch depth is about 2 μm. Following the etch, the silicon dioxide is removed by a 3 minute dip in buffered hydrofluoric acid.

A smooth side-wall is critical to ring operation as loss in the ring is determined to a large extent by scattering from side-wall roughness.

3.3.11 N-metal lithography

A 1600 nm thick negative resist (NR7-1500PY Shipley) is spun onto the wafer-piece and baked. It is then exposed on the projection aligner using the n-metal photomask. Following the exposure, it is hard-baked and developed to form the metallization pattern. The areas to be metalized are open while the remaining areas are covered by the resist. Negative resist provides the negatively sloped sidewall required for metalization by lift-off.

3.3.12 N-metal evaporation

The n-contact if formed by evaporating Ni, Ge, Au, Ni, Au in an e-beam evaporator with thicknesses of 50, 300, 800, 400, 2500 Å respectively. Prior to evaporation the wafer-piece is dipped in a 5% solution of sulfuric acid (H_2SO_4) to remove native surface oxides. Following the evaporation, the wafer-piece is soaked in acetone for about 10 minutes to lift-off the evaporated metal leaving behind metal only in areas not covered by the negative resist.

3.3.13 Sulfur passivation

Sulfur passivation is carried out to minimize carrier loss to surface recombination [6]. The wafer-piece is first dipped for 2 minutes in buffered hydrofluoric acid to to remove native oxides. It is then rinsed in DI water followed by a rinse in iso-propanol. Following this, it is immediately immersed in a saturated solution of sodium sulfide in iso-propanol for 2 minutes [83]. The sodium sulfide solution is filtered through a micro-filter to eliminate undissolved sodium sulfide crystals from settling on the wafer-piece. It is then rinsed in iso-propanol, blown dry and immediately transferred to the HDPECVD

chamber.

3.3.14 Passivation protection using silicon nitride

The sulfur passivation is prone to deterioration in atmosphere due to oxidation. To prevent this, a thin layer of silicon nitride is deposited on the wafer-piece immediately following the passivation procedure [84, 85]. The 20 nm thick silicon nitride is deposited using an HDPECVD system at a low temperature of 120 °C. The silicon nitride layer also serves the purpose of enhancing adhesion of the planarizing polymer (BCB) to the ring sidewalls.

3.3.15 Planarization

A thick layer of BCB (~ 6 μm) is spun on along with an adhesion promoter to cover and planarize the rings. It is then cured in an oven at 225 °C for 2 hours in a nitrogen ambient.

3.3.16 Etch-back

The cured BCB layer is blanket etched in an RIE system to expose the top of the rings for subsequent metalization. The etch stop point is determined by monitoring the color changes between etch runs. As the thickness decreases, color fringes can be seen atop the rings which disappear when all the BCB above the ring is removed.

3.3.17 P-metal lithography

As before, negative resist is used to pattern openings for depositing the p-metal on top of the rings.

3.3.18 P-metal evaporation

The p-contact is formed by successively depositing Ti-Pt-Au in an e-beam evaporator with thicknesses of 100, 500 and 3000 Å correspondingly. Prior to evaporation, the wafer-piece is dipped in 5% sulfuric to remove native oxides. Following the evaporation, it is soaked in acetone to lift-off the metal leaving behind the contacts.

3.3.19 Via etch lithography for n-contacts

The n-contacts buried beneath the BCB planarization layer need to be exposed to enable a probe needle to contact them. A lithography step is carried out to define openings in a photoresist layer (OiR 908-35) above the BCB. The openings are used to etch vias in the BCB layer down to the n-metal.

3.3.20 Via etch for n-contacts

Following the lithography, the BCB is etched in an RIE system using the photoresist as an etch mask. The large thickness of the photo-resist compared to the BCB layer compensates for the near equal etch-rates of the two. The photoresist is then removed by dissolving it in acetone.

3.3.21 Wafer thinning

The substrate is thinned from 350 μm to approximately 150 μm by mechanical lapping. The thinning ensures good crystal cleaving to separate the devices into bars for easy testing.

3.3.22 Scribing and cleaving

The thinned wafer-piece is then scribed using a high-power laser scriber setup.

The scribing ensures that the crystal cleaves along the scribe lines giving optical quality facets for the waveguides. The die pattern is aligned along a crystal axis during the first lithography step (bus waveguide definition). Consequently the scribe lines are long crystal axes. Cleaving is done by sandwiching the thinned and scribed wafer piece between flexible polyethylene sheets and applying downward pressure over a horizontal sharp edge aligned along the scribe line. The cleaved bars, about 800 μm in width and 8 mm long, are then separated.

3.3.23 Rapid thermal annealing

After the devices are cleaved into bars, they are annealed in a rapid thermal annealing system at 400 °C for a short interval. The anneal results in the formation of an low resistance ohmic contact at the metal-semiconductor junctions.

3.3.24 Mounting

The annealed bars are mounted on the narrow face of 5mm x 12 mm x 1mm copper heat-sinks using a silver-epoxy (Omegatherm HD5) as the glue. A ‘pick and place’ system is used to ensure accurate alignment of the bars and heat-sinks. The epoxy is then cured by heating the bars on a hot-plate for 15 min at 120 °C.

3.3.25 Anti-reflection coating

The large contrast in refractive index between the waveguide and air means that a large part of the incident light is reflected from the facet. Also, the Fabry-Perot resonator formed by the waveguide facets modulates the resonance behavior of the microrings. To eliminate this coupled cavity effect and to increase power coupling from the fiber, the facets are coated with a quarter wavelength thick layer of aluminum oxide (Al_2O_3), which

has a refractive index of about 1.6 ($n_{Al_2O_3} \approx \sqrt{n_{air} \cdot n_{InP}}$). The coating is carried out using an e-beam evaporator. To ensure that the coating does not cover the metal contacts, the devices are mounted at a 15° angle inside the evaporator and the thickness re-calibrated to account for the tilt.

Figure 3.11 shows the SEM scan of a completely processed device along with a schematic off the cross-section.

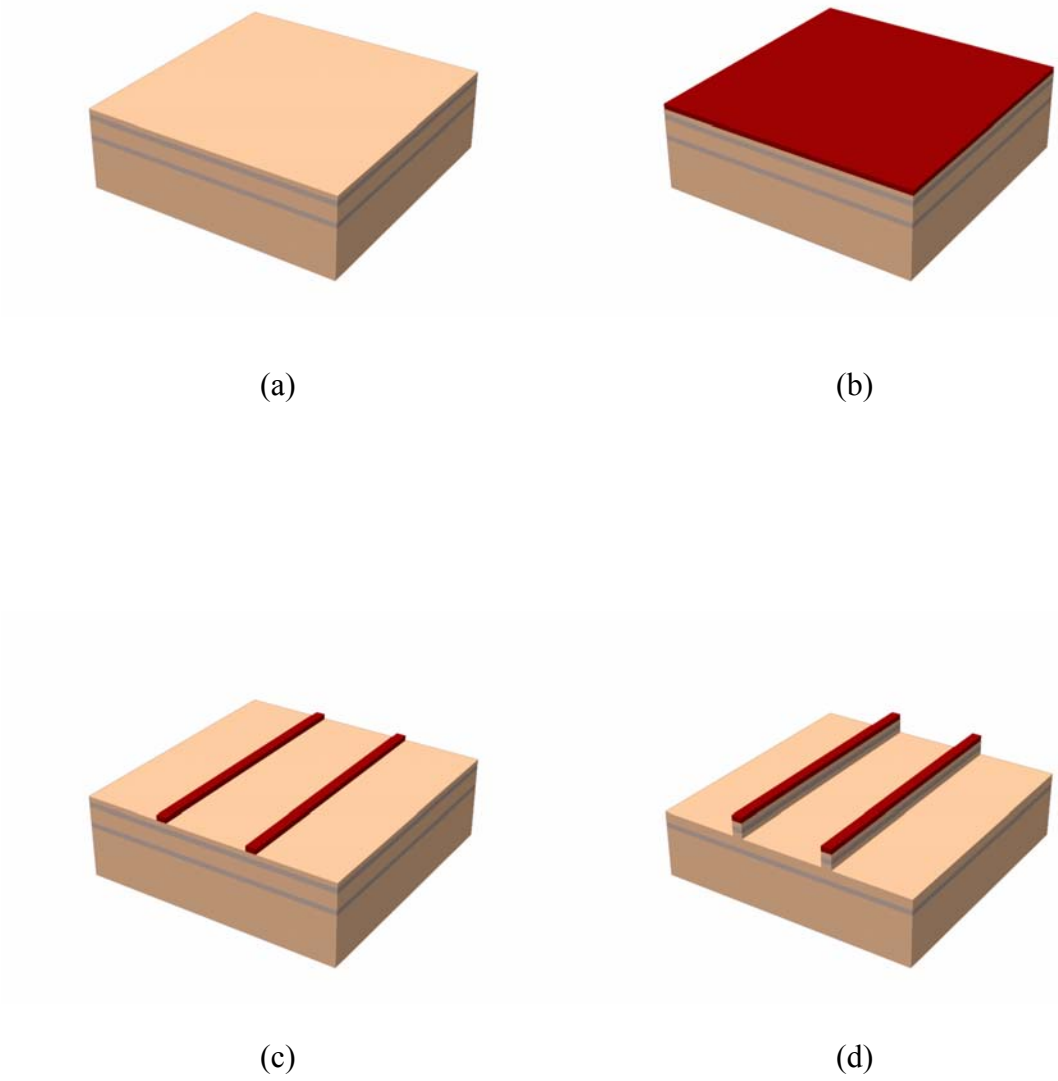

Figure 3.10: Steps in the processing of vertically coupled active microrings. (a) Wafer-piece with epi-growth (b) Deposit 300 nm of silicon dioxide etch-mask in HDPECVD (c) Lithographically pattern bus-waveguides and transfer pattern to silicon dioxide in RIE (d)Bus waveguide etch in RIE using silicon dioxide etch-mask.

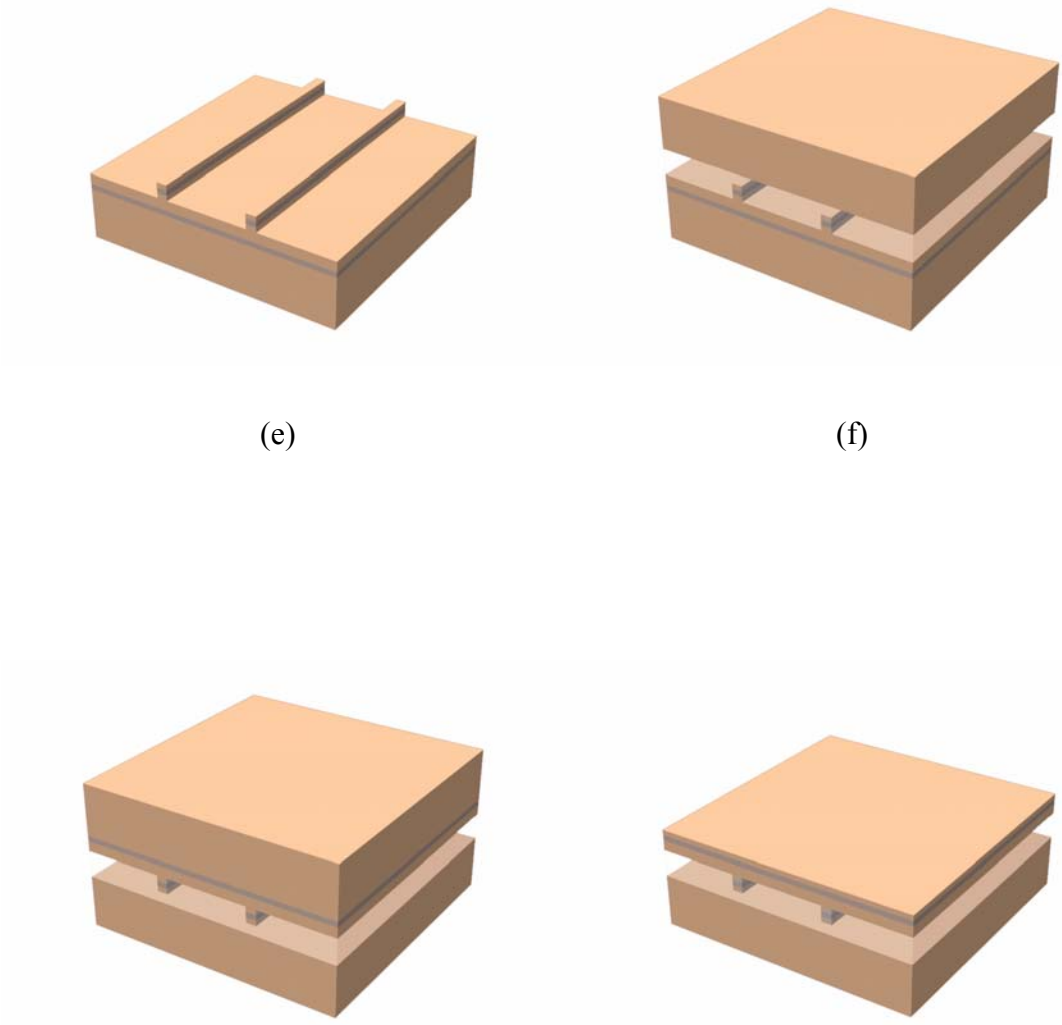

Figure 3.10: (Contd.) (e) Remove etch-mask in BHF (f) Wafer-bond using BCB (g) Flip original and carrier substrate (h) Thin original substrate by mechanical lapping and wet etching

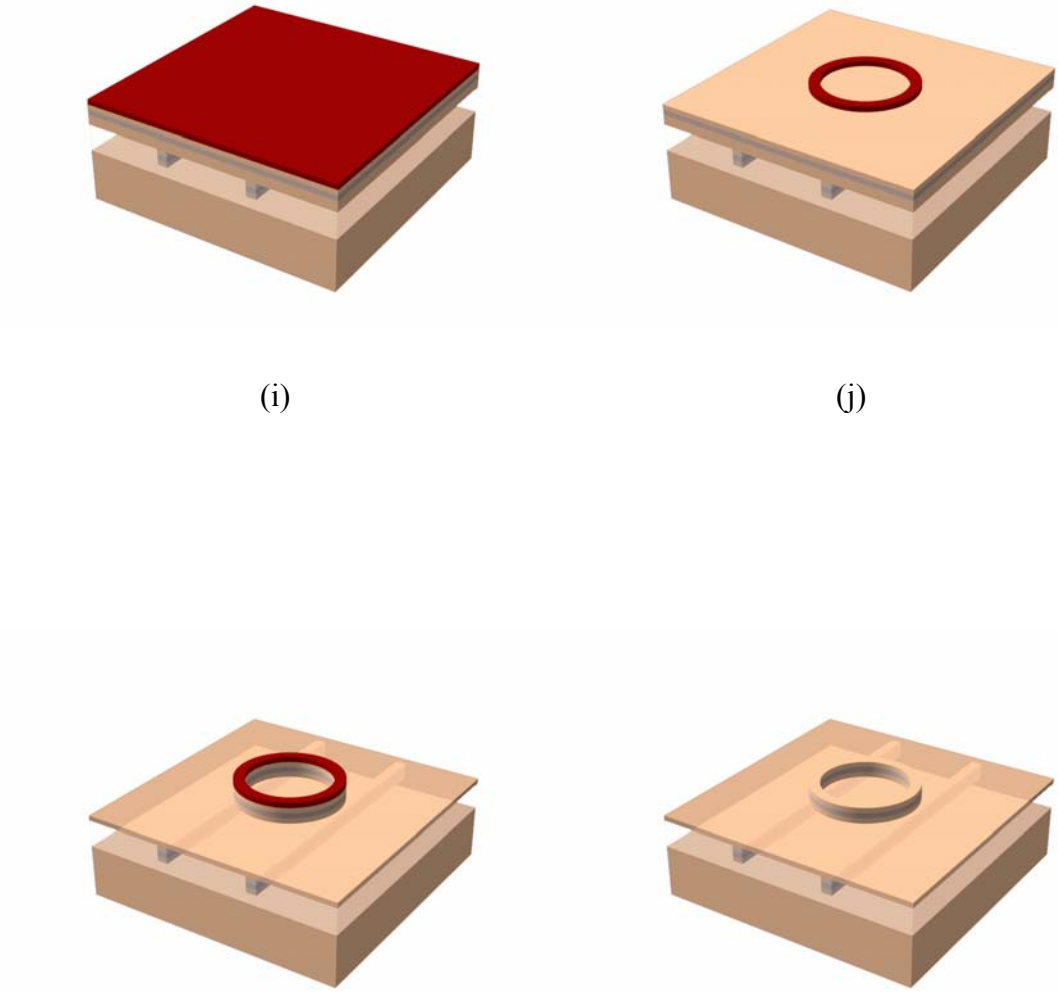

Figure 3.10: (Contd.) (i) Deposit 500 nm silicon dioxide etch mask in HDPECVD (j) Lithographically pattern microrings and transfer pattern to etch mask (k) Etch microrings in RIE using silicon dioxide etch mask (l) Remove etch-mask by dip in BHF

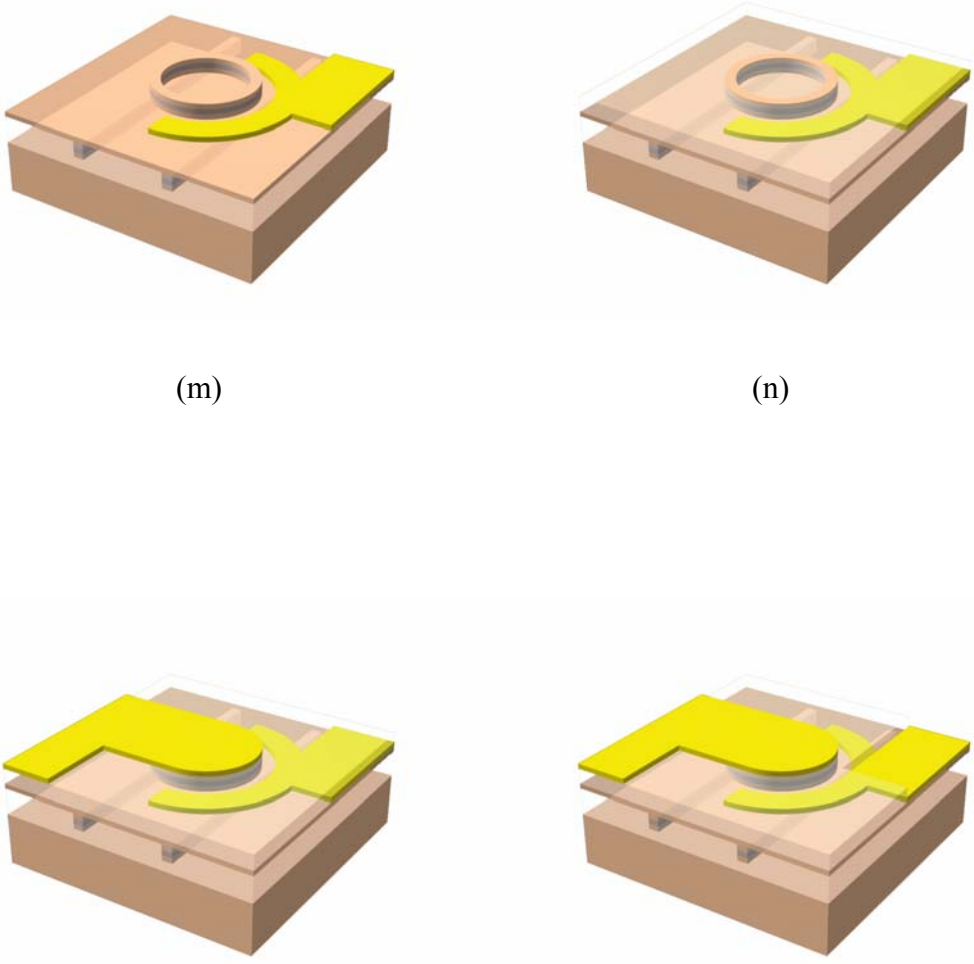

(m) (n)

(o) (p)

Figure 3.10: (Contd.) (m) Lithographically pattern and evaporate n-contacts (n) Planarize with BCB and etch-back in RIE (o) Lithographically pattern and evaporate p-contacts (p) Lithographically pattern via openings and etch BCB in RIE to expose n-contacts

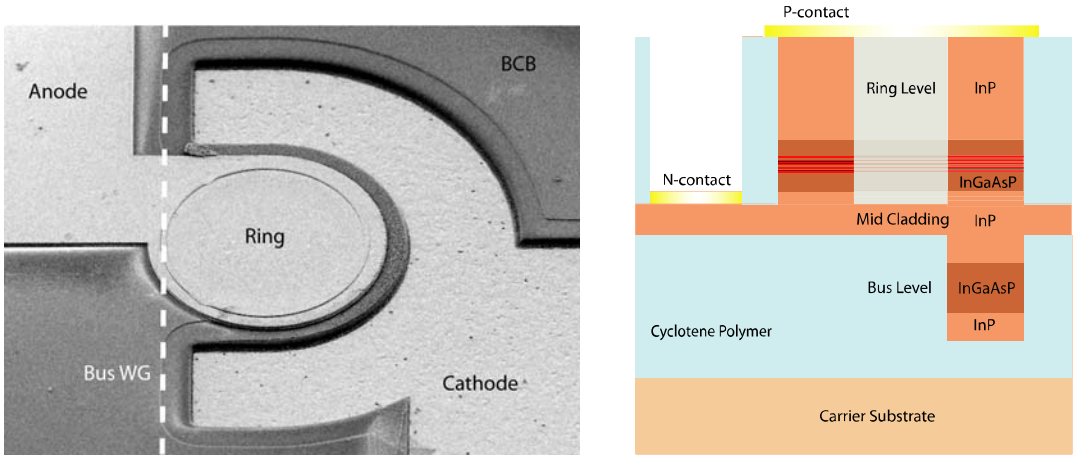

Figure 3.11: (a) SEM scan of a fully processed device. The bus waveguide is on the other side and indicated by a dashed line. (b) Schematic cross-section of a vertically coupled active microring.

Chapter 4

SURFACE RECOMBINATION AND PASSIVATION

In this chapter, I will discuss the effect of surface recombination on the device performance and model the lateral carrier transport process in quantum wells. The model will be used to analyze the experimental results from test devices to gauge the effectiveness of the sulfur passivation scheme to control surface recombination.

Surface recombination in III-V compounds and ways to control it has been explored in great detail in previous studies, especially in GaAs based devices [86]. The presence of surface oxides and un-terminated bonds on the surface of III-V compounds has been thought to produce mid-gap recombination sites and/or surface Fermi-level pinning [87, 88]. Several studies subsequently have shown that treating the surfaces in solutions that contain sulfur results in the removal of oxygen and replacement by sulfur to form In-S-In, Ga-S-Ga or In-S-Ga bonds, which are thought to have energy states outside the band-gap [89, 90]. Such treated surfaces show a remarkable drop in surface recombination as well as a sharp increase in photo-luminescence (PL) intensity [91-93]. Gallium containing compounds typically have higher surface recombination compared to indium containing compounds. The surface recombination rate is characterized by the surface-recombination velocity (S_v):

$$J_s = qnS_v \tag{4.1}$$

Here, J_s is the surface recombination current density and n is the surface carrier density. Typical measured values of S_v for GaAs are around 6 x 10^5 cm/s [94]. For n-type GaAs this can be as high as 2 x 10^6 cm/s [95], showing that the limiting factor is the electron capture rate at recombination centers. For bulk InP, the surface recombination velocity is almost two orders of magnitude lower. Typical measured values are around 1.5 x 10^4 cm/s [96]. In the devices studied here, the quantum well is an InGaAsP quaternary with a significant amount of gallium (~ 27 %). Hence, the surface recombination velocity is expected to be higher than that measured for bulk InP. This also makes the quantum wells the primary location of surface recombination in the device.

4.1 Lateral Carrier Transport in Quantum Wells

The majority of the carriers injected at the top and bottom of the ring make their way to the quantum wells, where they undergo recombination. A large part of the carriers in the quantum well diffuse along the well to reach the surface, where they undergo recombination through surface states. It is useful to calculate the fraction of injected carriers that are lost to surface recombination so as to estimate the need for surface passivation. The transport can be modeled by means of ambipolar diffusion equations and is outlined below [97]. Consider the device cross-section shown in figure 4.1. The carriers are assumed to be injected uniformly throughout the width of the quantum well with a current density $J_{n,p}$. The 1-D drift-diffusion equations for holes and electrons in the quantum well can be written as:

$$J_n = q\mu_n nE + qD_n \frac{dn}{dx}$$
$$J_p = q\mu_p pE - qD_p \frac{dp}{dx} \tag{4.2}$$

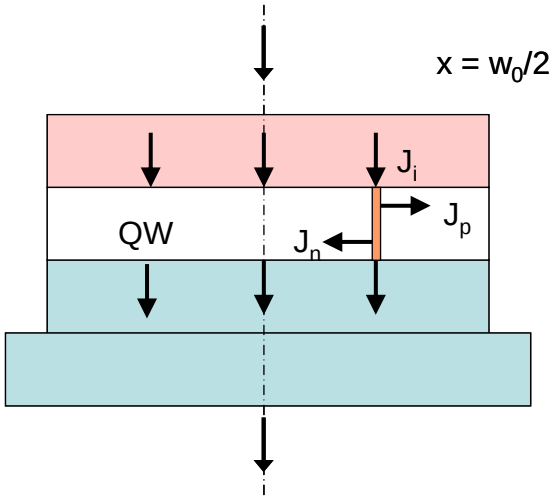

Figure 4.1: Schematic for modeling lateral transport of injected carriers in a quantum well in the ring core. The lateral hole and electron currents are equal and opposite. The injected current J_i is assumed to be constant throughout the width of the structure.

Here, *n,p* are the electron and hole densities, $D_{n,p}$, $\mu_{n,p}$ the corresponding diffusion coefficient and mobility respectively. *E* is the lateral electric field. The choice of cartesian coordinates over polar is due to the fact that the ring/waveguide thickness is much smaller (0.8 μm) compared to the radius (> 10 μm). Thus, the transport in the small thickness can be approximated as a 1-D system along the width of the waveguide. At any point along the x-direction, the hole and electron currents must be equal and opposite as there cannot be a net lateral current. This is because for every electron that reaches the surface and recombines, a hole has to be provided for the recombination. Assuming the carriers cannot escape once inside the quantum well, this implies equal and opposite electron and hole currents.

$$\begin{aligned} J_n &= -J_p \\ q\mu_n nE + qD_n \frac{dn}{dx} &= -q\mu_p pE + qD_p \frac{dp}{dx} \end{aligned} \tag{4.3}$$

This gives an expression for the lateral electric field:

$$E = \frac{-D_n \frac{dn}{dx} + D_p \frac{dp}{dx}}{\mu_n n + \mu_p p} \tag{4.4}$$

Another useful assumption is quasi-neutrality ($n \approx p$). The hole and electron densities at any point on the x-coordinate can be assumed to be approximately equal since there are no dopants in the quantum well. Strictly speaking, there cannot be an intrinsic lateral electric field without some charge imbalance. However, this imbalance ($|n - p|$) is very small compared to carrier density variation in the lateral direction ($n\big|_{x=0} - n\big|_{x=w/2}$) that it can be neglected, i.e. $dn/dx \approx dp/dx$. Thus, the expression for electric field assuming charge quasi-neutrality is given by:

$$E = \frac{-D_n + D_p}{\mu_n + \mu_p} \cdot \frac{1}{n} \frac{dn}{dx} \tag{4.5}$$

Plugging this back in the expression for the electron current results in:

$$J_n = -J_p = q \frac{\mu_n D_p + \mu_p D_n}{\mu_p + \mu_n} \cdot \frac{dn}{dx} = qD_a \frac{dn}{dx} \tag{4.6}$$

Here D_a is the ambipolar diffusion coefficient and defined by:

$$D_a = \frac{\mu_n D_p + \mu_p D_n}{\mu_p + \mu_n} = \frac{kT}{q} \cdot \frac{\mu_p \mu_n}{\mu_p + \mu_n} \tag{4.7}$$

The second equality in the above expression is derived by making use of the Einstein relation:

$$\frac{D}{\mu} = \frac{kT}{q} \tag{4.8}$$

The expression for the ambipolar diffusion coefficient in eqn. 4.7 implies that the

transport of both holes and electrons is now determined by the species with the lower mobility, which happens to be holes in most semiconductors.

The continuity equation for carriers can now be written using the expression for the electron and hole diffusion currents from above.

$$D_a \frac{d^2 n}{dx^2} - \frac{n}{\tau_c} + \frac{J_i}{qh} = 0 \tag{4.9}$$

The first term represents the net electron diffusion current into a small slice/volume along the x-axis. The last term represents the carrier injection into the quantum well volume from the applied bias. The constant *h* is the quantum well thickness.

The second term represents the carrier loss to recombination within the volume. τ_c represents the average carrier lifetime in the quantum well. It represents the average lifetime for a variety of carrier loss mechanisms including spontaneous recombination, Auger recombination as well as Shockley-Reed-Hall type of recombination at defect centers within the band-gap. Each of these processes varies differently with carrier density. For example defect recombination varies as An, while spontaneous recombination varies as Bn^2, and Auger processes vary as Cn^3. Thus,

$$\frac{n}{\tau_c} = An + Bn^2 + Cn^3 \tag{4.10}$$

For ease of solution and the purpose of demonstration, the simpler expression for the carrier recombination is used, as in eqn. 4.9. However, for analyzing experimental results, the carrier recombination term will be replaced by the one in eqn. 4.10.

Equation 4.9 needs to solved over the range x = [0, w/2], where *w* is the width of the ring. The boundary conditions are determined by two conditions: the electron/hole

current is zero at the center of waveguide for reasons of symmetry and the current at the edge of the waveguide is equal to the carrier surface recombination current. Thus the B.C.s are:

$$\left.\frac{dn}{dx}\right|_{x=0} = 0$$
$$-qD_a \left.\frac{dn}{dx}\right|_{x=w/2} = qS_v n(x = w/2) \tag{4.11}$$

The general solution to eqn. 4.9 is of the form:

$$n(x) = A\exp(x/\sqrt{\tau_c D_a}) + B\exp(-x/\sqrt{\tau_c D_a}) + \frac{J_i \tau_c}{hq} \tag{4.12}$$

Applying the boundary conditions results in the expression for carrier density:

$$n(x) = \frac{J_i \tau_c}{hq}\left(1 - \frac{\cosh(2x/w_0)}{\frac{2D_a}{S_v w_0}\sinh(w/w_0) + \cosh(w/w_0)}\right) \tag{4.13}$$

Here, w_0 is the diffusion length and given by $w_0 = 2\sqrt{D_a \tau_c}$. The current is then given by eqn.4.6.

$$J_n(x) = -\frac{J_i w_0}{2h}\left(\frac{\tanh(2x/w_0)}{1 + \frac{2D_a}{S_v w_0}\tanh(w/w_0)}\right) \tag{4.14}$$

The fraction of the injected current that is lost to surface recombination can be estimated by taking the ratio of the lateral current at x = w/2 to the total injected current.

$$\frac{I_{sr}}{I_{tot}} = \left| \frac{J_n\big|_{x=w/2} \cdot h}{J_i \cdot w/2} \right| = \frac{w}{w_0} \cdot \frac{\tanh(w/w_0)}{1 + \frac{2D_a}{S_v w_0} \tanh(w/w_0)} \tag{4.15}$$

Figure 4.2 is a plot of the fraction of device current lost to surface recombination as a function of the waveguide width. The values of parameters used in eqn. 4.15 are indicated in the figure and are typical for the InGaAsP quantum well system. The ambipolar diffusion coefficient is assumed to be 7 cm^2/s [4]. The values of carrier lifetime shown in the graph represent the extremes of what is typically seen. Typically lifetimes of carriers in InGaAsP quantum wells are usually a few nanoseconds. The two values of the surface recombination velocity represent the case of InP (2 x 10^4 cm/s) and InGaAs (1 x 10^5 cm/s). The quaternary InGaAsP material used in the quantum wells of the microrings is expected to fall in between these two extremes. The graph is very informative in that it predicts the utility of any passivation scheme. The typical ring width is about 1 μm. For this width, it can be seen from the graph that between 30 to 80 % of the carriers can be lost to surface recombination even for the lower extreme of the surface recombination velocity. Since ohmic heating varies as I^2R, it is very critical that surface recombination be controlled by means of passivation in order to keep device currents and consequent heating to a minimum.

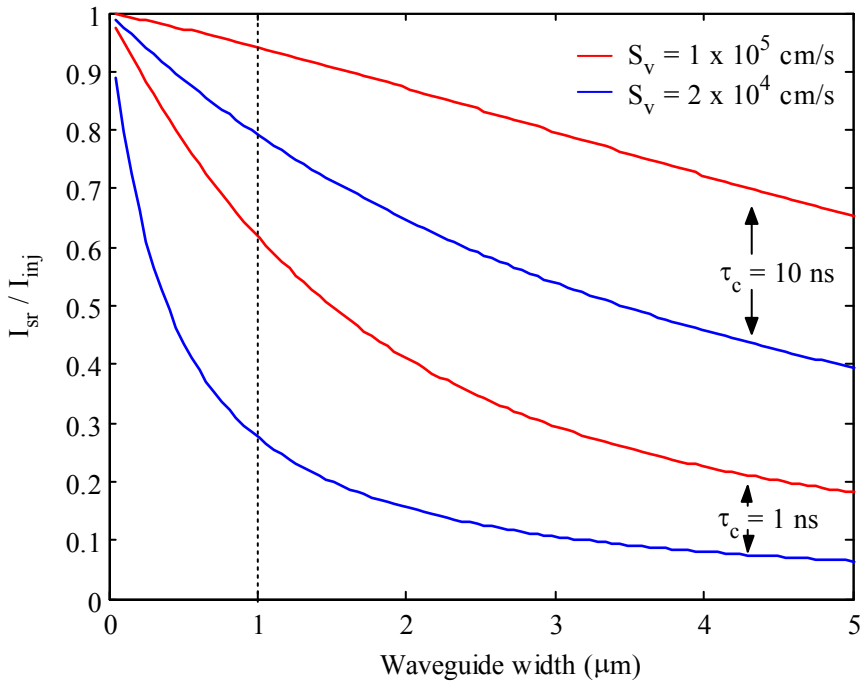

Figure 4.2: Plot of fraction of device current lost to surface recombination as a function of ring width calculated using eqn.5.15. The typical ring width of 1 μm is indicated by a dashed line. The values of parameters used represent the extremes.

4.2 Measuring the Effect of Passivation

Sulfur treatments have been shown to be very effective in controlling surface states in III-V semiconductors. Of these, the saturated solution of sodium sulfide (Na_2S) in isopropanol ($CH_3CH(OH)CH_3$) has been shown to be better than aqueous solutions in the amount of sulfur coverage of the surface [83]. In order to verify the effect and efficiency of this passivation scheme, a set of deep-etched test ridge lasers was fabricated. The goal of the experiment was to measure the drop in threshold currents following passivation and correlate this with the drop in surface recombination velocity using the model developed in the previous section. The ridge-lasers are 3 μm wide and of

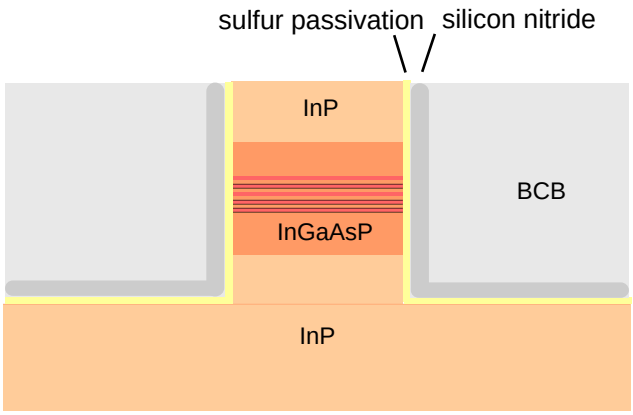

Figure 4.3: Schematic cross-section of ridge-lasers used to measure the effect of passivation. The ridges are 3 μm wide. The quantum wells are exposed on the side-walls of the ridge.

varying length (500 to 1100 μm). A cross-section of the ridge lasers is shown in figure 4.3. The lasers are fabricated by plasma etching in an RIE system using silicon dioxide as an etch mask. They are etched deep enough that the quantum wells are exposed on the side-walls of the ridge. Following the etch, they are passivated and capped with a silicon nitride layer as described in chapter 3. A set of control lasers is also processed identically except for the passivation step. They are then planarized and metal contacts added. After annealing to alloy the contacts, they are scribed and cleaved into bars of varying lengths.

The lasers were tested for the L-I characteristics in pulsed mode at room-temperature. Figure 4.4 shows the measured threshold currents for both the passivated (blue) and un-passivated (red) devices. The error bars on the data points represent the total range in the measured values of threshold current for a particular length. Each point represents data from about 12 devices. From the graph, it can be seen the passivation scheme reduces the threshold currents by nearly 20 to 25 % for the 3 μm wide lasers. For rings which are 1 μm wide, the passivation can be expected to reduce the currents even more as a larger fraction of the carriers can reach the sidewalls.

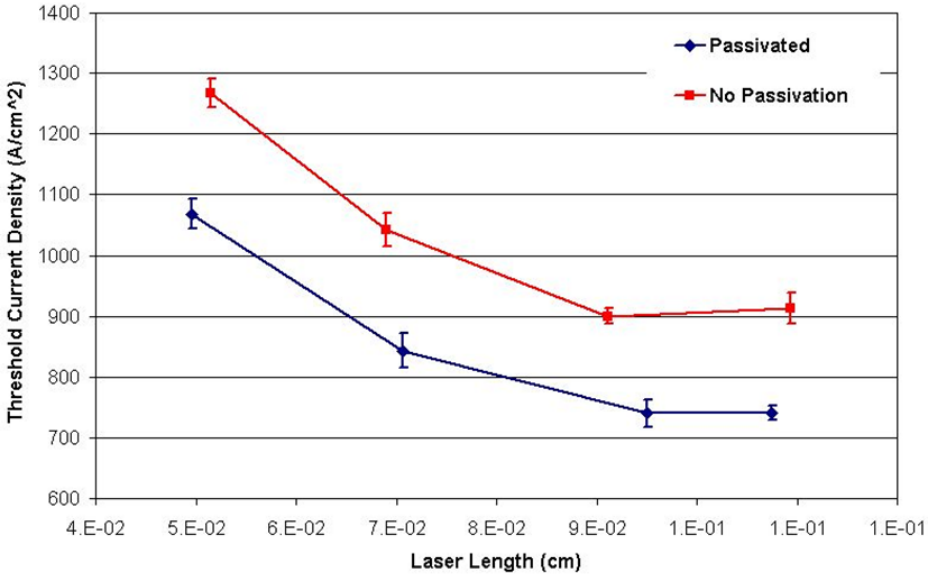

Figure 4.4: Measured threshold current in ridge lasers as a function of length for devices with (blue) and without (red) passivation. Error bars represent the total range of measured values for a particular length.

The data was analyzed using the model developed earlier for carrier transport in quantum wells with one change. The expression for the carrier lifetime was now expanded to include the dependence on carrier density for the various processes. The 1-d continuity equation was rewritten as:

$$D_a \frac{d^2 n}{dx^2} - An - Bn^2 - Cn^3 + \frac{\eta_{inj} J_s}{qN_{QW} h} = 0 \qquad (4.16)$$

Here, η_{inj} represents the injection efficiency or the fraction of total carriers (J_s) that get trapped in the quantum wells. N_{QW} represents the number of quantum wells. The solution to the above equation is subject to the same boundary conditions as before (eqn. 4.11). The solution was obtained numerically by means of a MATLAB script. The values of the various parameters used are indicated in table 5.1.

Parameter	Value
Ambipolar diffusion coeff. (D_a)	7 cm^2/s
Monomolecular recomb. coeff (A)	5 x 10^7 /s
Bimolecular recomb. coeff. (B)	1 x 10^{-10} cm^3/s
Auger recomb. coeff. (C)	8 x 10^{-29} cm^6/s
Injection efficiency (η_{inj})	0.8
Quantum well thickness (h)	10 nm
Number of quantum wells (N_{QW})	5
Surface recomb. velocity (S_v) before passivation	2.5 x 10^4 cm/s

Table 4.1: Values of parameters used to model surface recombination and passivation efficiency in test ridge lasers. Values are taken from ref. [4-6].

Using the model and the experimental data, it was estimated that the surface recombination velocity dropped from 2.5 x 10^4 cm/s to nearly 4 x 10^3 cm/s following passivation. This corresponds to over 30 % drop in current for the 0.8 μm to 1 μm wide waveguides used in microrings.

Chapter 5

AMPLIFICATION AND LASING IN MICRORINGS

In this chapter I will present and analyze the results from vertically coupled active microring optical amplifiers and lasers fabricated as described in chapter 3. The microring amplifiers are intended for use in cascaded photonic logic gates. All-optical logic gates based on passive microrings have been previously demonstrated [98]. Such devices operate by switching a low-power probe beam using a high-power pump beam to effect a non-linear refractive index change that causes the ring resonances to shift. However, it is difficult to cascade multiple gates to form optical logic circuits due to 1) the insertion losses associated with each stage and 2) the fact that the low-power probe beam for the preceding stage has to form the high-power pump beam for the succeeding stage. Incorporating a microring amplifier between successive stages can solve both the problems. Strictly speaking, a linear semiconductor optical amplifier can perform these functions too. The advantage of the microring amplifier is its compactness without loss of amplifying power. This is achieved by trading off un-necessary bandwidth for higher amplification by use of a resonator. Also, the presence of gain within a resonator such as a microring means that the refractive index non-linearity is enhanced compared to a passive device and the amplifier itself can form the switching element.

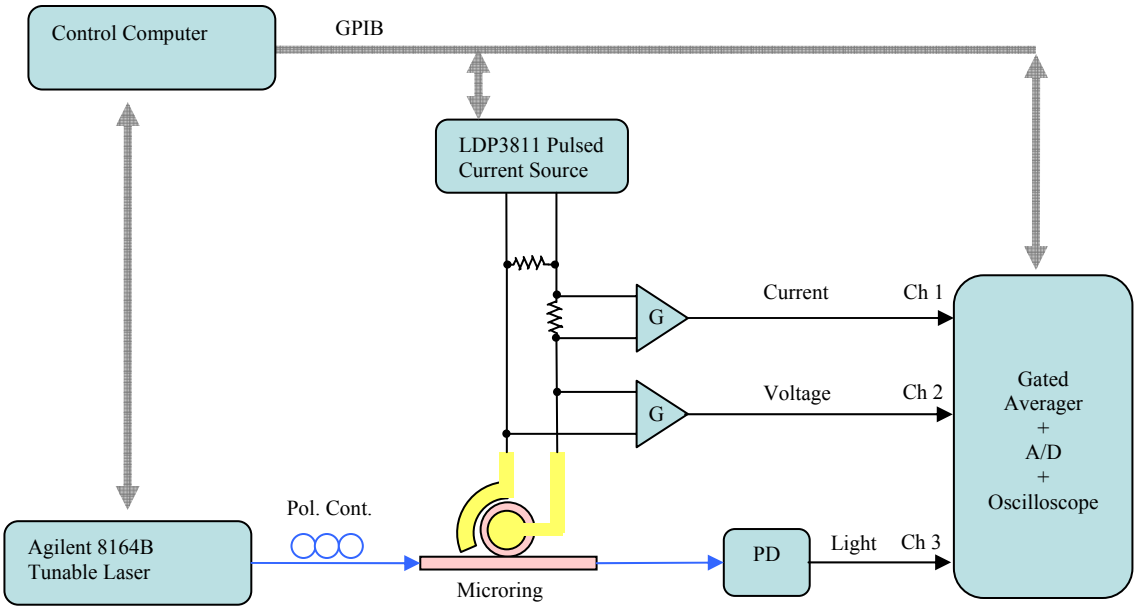

Figure 5.1: Schematic of experimental setup for pulsed testing of vertically coupled active microrings. The inset shows a photograph of the device with probes and lensed fibers.

5.1 Test Setup

Figure 5.1 shows the schematic of the test setup. Light is coupled in and out of the device through lensed fibers mounted on a 3-axis piezo stage. Electrical contact is made by probe needles controlled by a 3-axis positioner. The devices were tested in pulsed mode to avoid performance loss due to heating. The devices were also mounted on a thermoelectric cooler to keep operating temperatures below room-temperature. Light from a tunable laser source passes through a polarization controller set to transmit the horizontally polarized component corresponding to the E_{11}^{x} mode of the ring. The electrical pumping is done in pulsed mode with 5 µs long pulses at 1 ms intervals. The current and voltage at the device is monitored by a gated averager. The optical output is

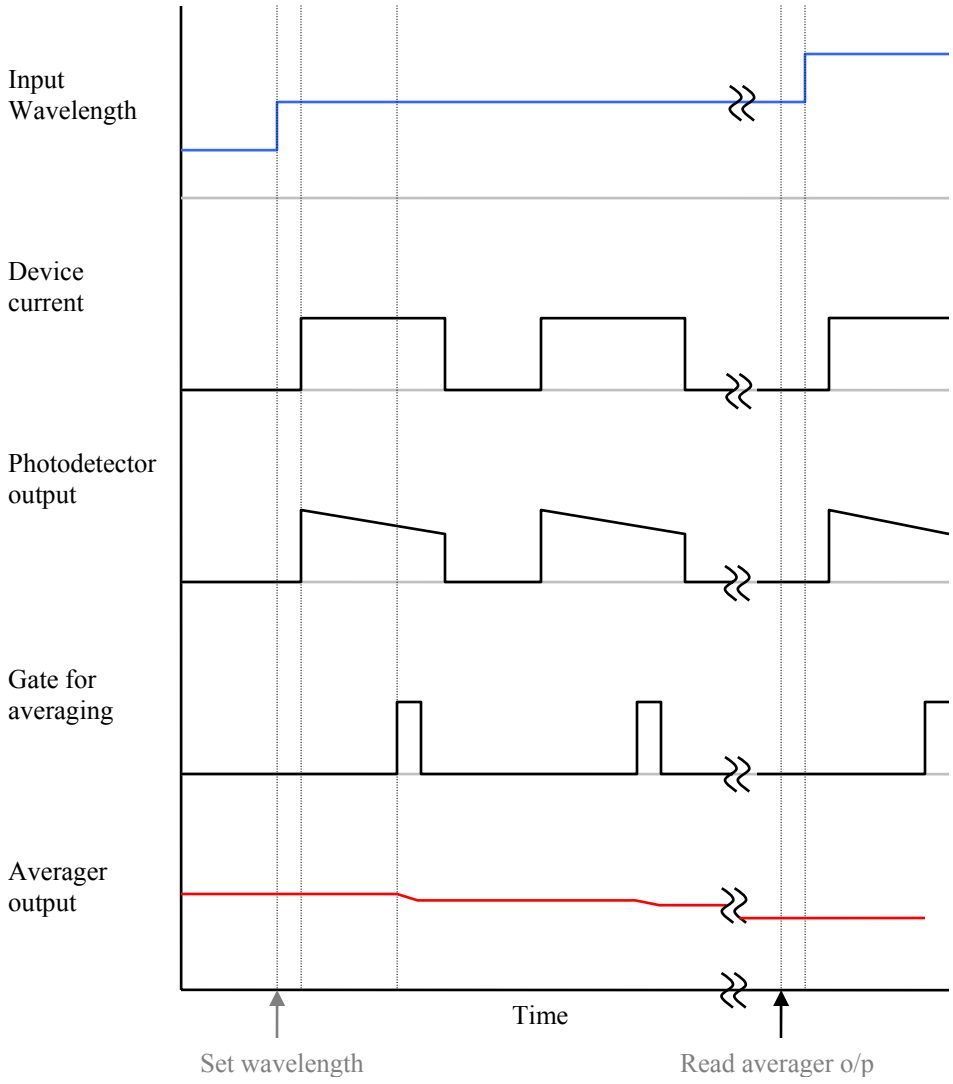

Figure 5.2: Schematic showing timing in one cycle of pulsed testing of active microrings. The cycle corresponds to one step in wavelength. Each cycle has many pulses, which are averaged before being read.

fed to a photodetector and the output monitored through the gated averager. The measurement timing is illustrated in figure 5.2. The timing and data acquisition for all the instruments is controlled via GPIB by a computer running a LABVIEW program.

The measurement cycle begins with setting the wavelength on the tunable laser source to a specific wavelength. The device is then pulsed electrically through a current source. The optical output is measured through a 10 ns gate delayed from the start of the

pulse by a fixed value. The measurement is averaged over a large number (~ 30) of pulses and read by the controlling program. The next cycle begins by incrementing the wavelength on the tunable laser.

5.2 Amplification in Microrings

Figure 5.3 shows the transfer characteristics of a 20 μm radius microring for increasing currents through the device measured in pulsed mode. Increasing the current through the device raises the round-trip field gain (a) in the resonator. As the gain increases, the transfer characteristics change from (i) under-coupled ($\kappa^2 < 1-a^2$) to (ii) critically coupled ($\kappa^2 = 1-a^2$) to over-coupled ($\kappa^2 > 1-a^2$) (iii) transparency ($a = 1$) to (iv) gain ($a > 1$) to (v) half the lasing threshold ($a^2 \approx 0.5*(1-\kappa^2)^{-1}$).

The variation in response across wavelength is primarily the result of two factors: the wavelength dependence of gain from the quantum wells and the variation of the coupling factor with wavelength, with the first factor being largely dominant over the second. Figure 5.4 shows a higher resolution scan of the through-port response and the corresponding theoretical fit over a narrower wavelength range for a device current of 30 mA. From the fitted spectrum, the peak gain at the through-port was estimated to be 8 dB for 30 mA current. This corresponds to a round-trip gain (a) of 1.21 and a coupling coefficient (κ) of 0.77. Gain up to 10 dB was observed for higher currents. The devices were designed to have a high coupling coefficient between the ring and bus waveguides since they are primarily meant to be used as compact optical amplifiers in photonic circuits.

There is a strong polarization dependence that is a result of three factors: 1) the coupling strength between bus and ring waveguide, 2) interaction strength with the

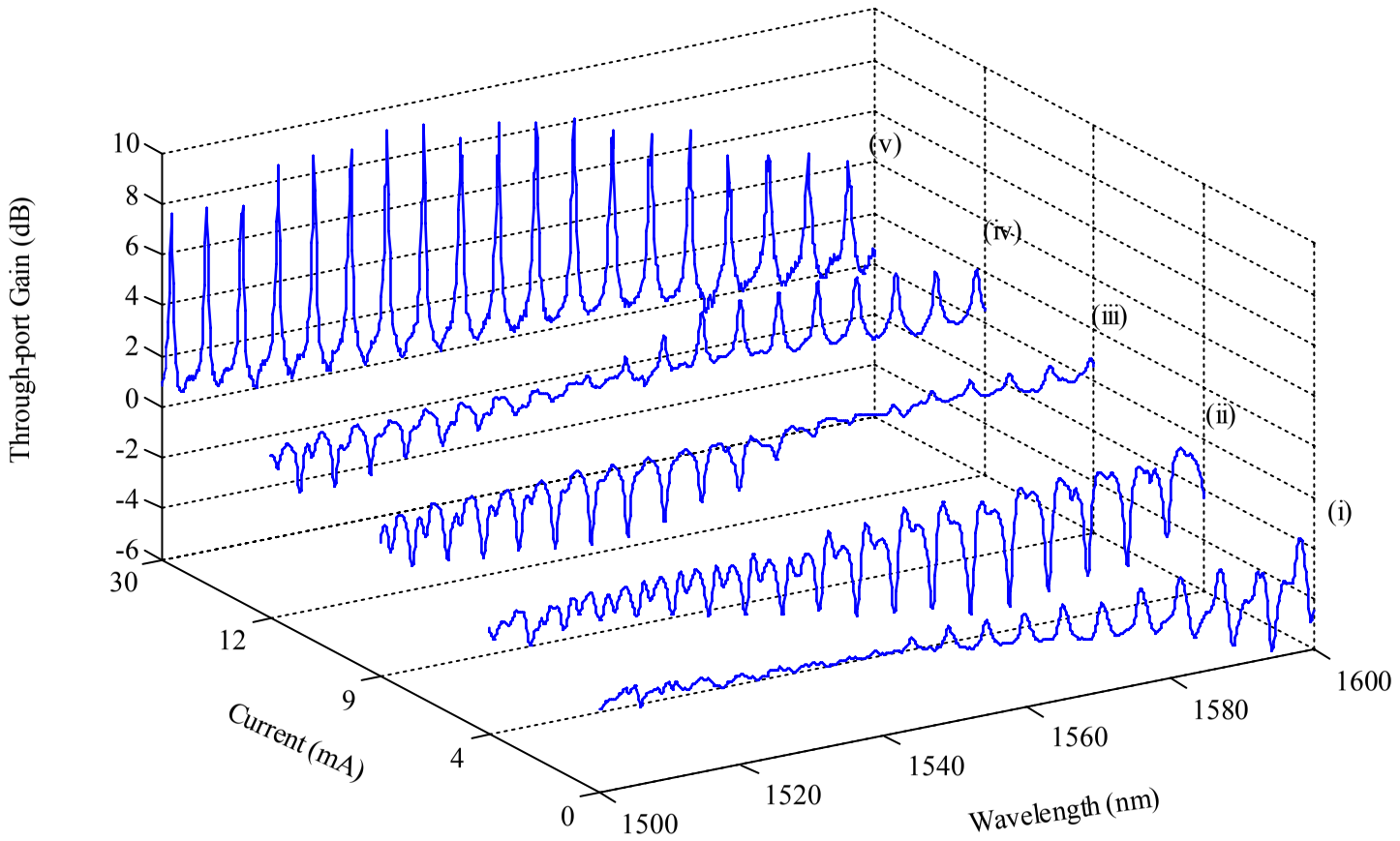

Figure 5.3: Through-port response of a 20 µm radius microring for increasing currents showing transition from (i) under-coupled ($\kappa^2 < 1-a^2$) to (ii) critically coupled ($\kappa^2 = 1-a^2$) to (iii) transparency ($a = 1$) to (iv) gain ($a > 1$) to (v) half the lasing threshold ($a^2 \approx 0.5*(1-\kappa^2)^{-1}$).

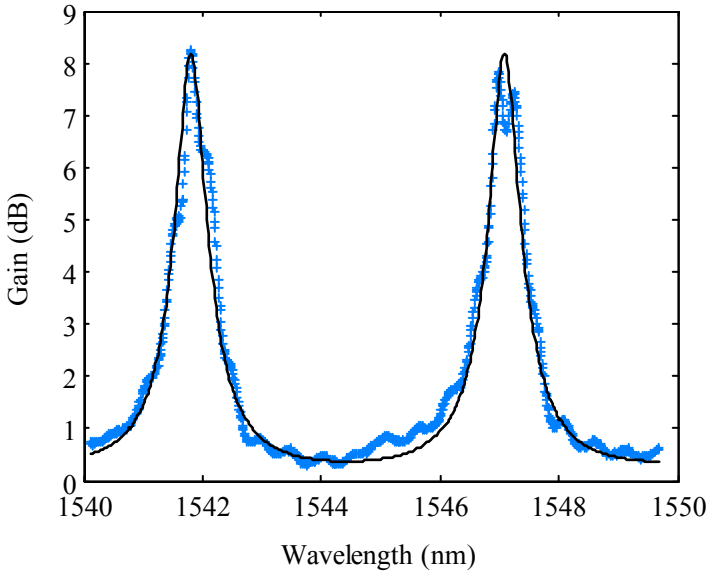

Figure 5.4: Throughport gain of microring amplifier (R = 20 µm). Higher resolution scan from 1540 to 1550 nm and theoretical fit showing 8 dB gain at I = 30 mA

quantum wells and 3) waveguide birefringence. The horizontally polarized mode has a lower coupling between the bus and ring waveguides in a vertically coupled structure. Gain or loss in the quantum well is dependent on polarization orientation with respect to the QW plane and is also influenced by stress / strain in the QW [99]. There is some polarization rotation in curved waveguides as the optical modes are no longer purely horizontally or vertically polarized [74, 100]. Also, deviations of the waveguide shape from a perfect rectangular profile cause the optical modes to have cross-polarization components. The net effect is coupling from the horizontally polarized mode in the bus waveguide to more than one mode in the ring waveguide, with the result that additional resonance features are seen in the transfer characteristics.

5.2.1 Resonance tuning by current

Changing the current through the device results in a shift of the resonance peaks.

There are several mechanisms through which this occurs. The first is the increase in free-carrier density in the quantum wells with bias, which results in the blue-shift of the resonances. Secondly, there is a change in loss or gain in the quantum well which affects the refractive index in a way that is determined by the Kramers-Kroenig relations [3, 101, 102]. Also, any rise in temperature (due to ohmic heating) changes the refractive index [103] in addition to the ring circumference due to thermal expansion of the ring material. Both these thermal effects result in a red-shift of the resonances. The net shift in resonance is a result of all these mechanisms occurring at the same time. The variation in resonance frequency with current can be used to tune a microring to a specific frequency. This is especially advantageous as the lithographic tolerances required for tuning by geometry alone is very small.

5.3 Lasing in Microrings

Increasing the current even higher results in lasing. The lasing threshold is determined by the condition that the net round-trip gain be equal to one.

$$a \cdot \tau = 1 \tag{4.17}$$

Figure 5.5 shows the light intensity versus driving current (in pulsed mode) for one such microring laser. Devices without anti-reflection coating on the waveguide facets behave as coupled cavity lasers, where the first cavity is the ring resonator and the second cavity is formed by the bus waveguide facets. The lasing spectrum for such devices, shown in the upper part of figure 5.6, appears as multiple peaks for each ring resonance, where the wavelength separation between two adjacent peaks in a bunch corresponds to the waveguide cavity free spectral range (FSR) and the separation between bunches

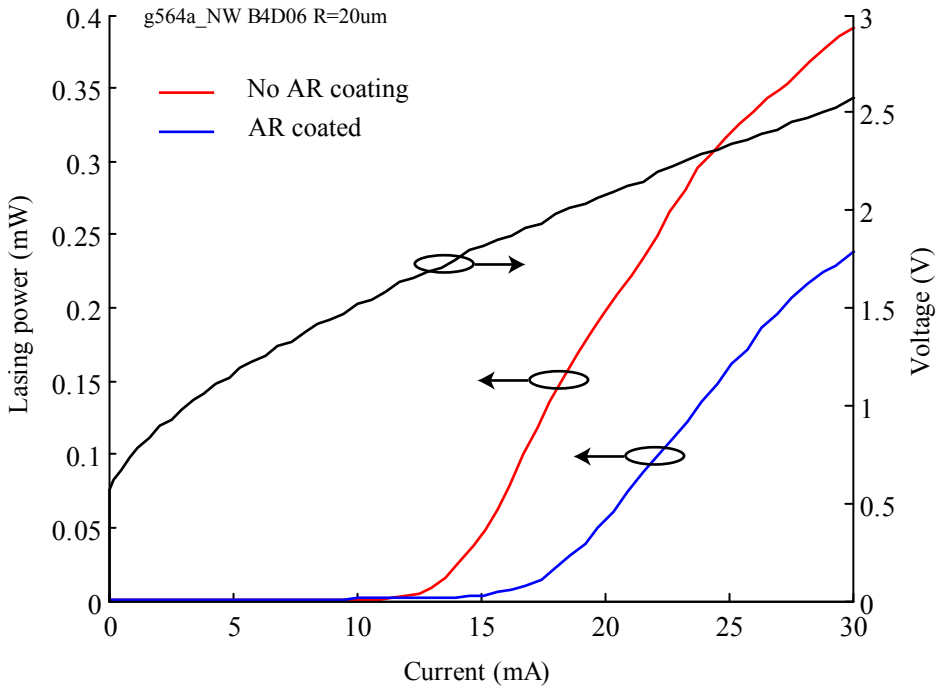

Figure 5.5: L-I curves (red and blue) for a 20 µm radius microring laser showing effect of anti-reflection coating. The black curve shows the V-I characteristics.

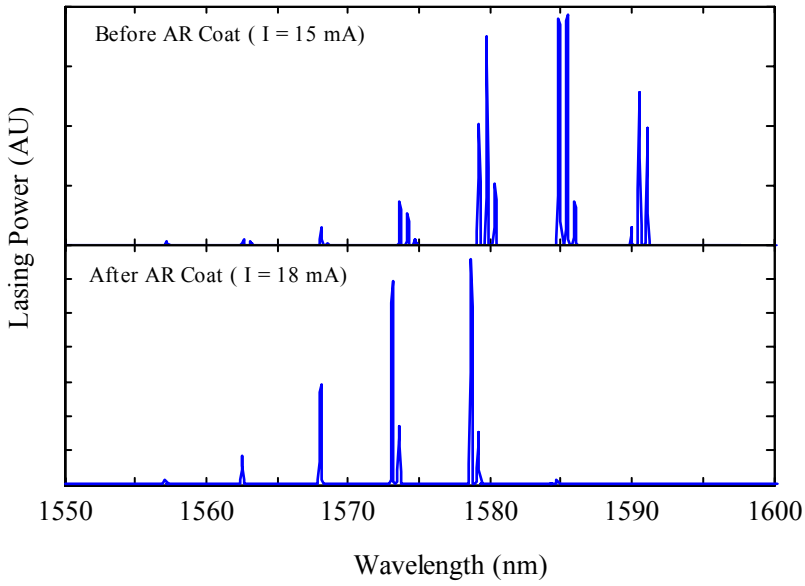

Figure 5.6: Lasing spectrum before and after AR coating. The coating reduces the influence of the waveguide cavity on the ring resonator.

corresponds to the ring cavity FSR. Following the anti-reflection coating, the effect of the waveguide cavity is reduced and lasing is essentially confined to just the ring cavity, as seen in the lower inset for figure 5.6. The rather wide emission spectrum for the devices is a result of inhomogeneous broadening due to non-uniform quantum well thickness and composition, which was confirmed from photo-luminescence measurements on the quantum wells. Threshold currents increased following the anti-reflection coating as the effective Q-factor is lowered.

The V-I characteristic is indicated by the black curve in figure 5.5. The differential resistance was measured to be 53 ohms.

5.4 Thermal Performance

The thermal performance of the device is limited by the heat dissipation from the ring to the carrier substrate through the BCB layer used for wafer bonding. BCB has one of the lowest thermal conductivities (k_{th} = 0.24 W/Km) amongst common micro-fabrication materials [82, 104].

The temperature in the ring can be deduced from a measurement of the shift in resonances as a function of time following switch-on. The resonance frequencies, besides being dependent on geometry and current through the device, are also determined by the temperature. Thus, if the temperature coefficient of variation of refractive index is known for the InGaAsP/InP system, the resonance shift measurements can be used to infer the temperature change in the microring. The resonance measurements are done as before (figure 5.2), but the gate-delay (τ_{delay}) is increased for successive wavelength scans. This has the effect of measuring the resonance at increasing delays following switch on. Figure 5.7 shows two such scans for different gate-delays. The microring can be assumed

to be at room temperature before switch-on and heats up immediately thereafter. Hence, higher gate-delays correspond to higher temperatures. Figure 5.8 shows the graph of resonance frequency shift as a function of gate-delay. Immediately after switch-on, the resonance is seen to blue-shift rapidly followed by a slower rise thereafter. The blue-shift is due to carrier injection into the ring-core, which results in a refractive index drop and hence the shift in resonances towards the shorter wavelengths. The time for the blue-shift is determined by the pulse rise time and is limited by load impedance. The temperature changes very little during this short period. Following that, the temperature rises in the ring and resonance shifts towards the longer wavelengths. Using the temperature coefficient of refractive index for InP (1.9×10^{-4} K^{-1}) [105] and the linear thermal expansion coefficient (4.6×10^{-6} K^{-1}), the temperature in the microring following switch-on is calculated. This is indicated on the y-axis on the right. The temperature is seen to rise nearly 20 °C over a very short period of time of about 5 μs.

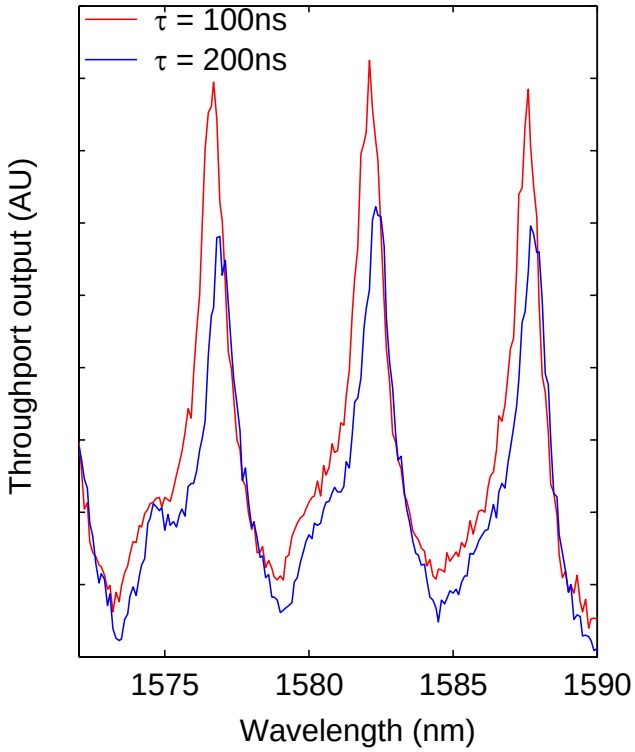

Figure 5.7: Through-port response of a 20 µm radius microring measured at gate-delays of 100 ns and 200 ns showing effect of temperature on resonance frequency.

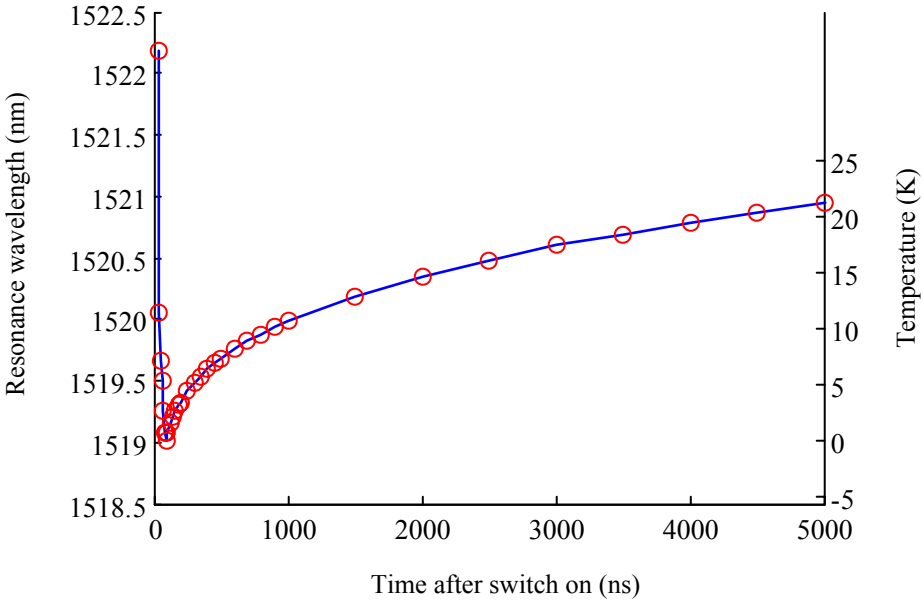

Figure 5.8: Resonance shift and corresponding temperature drift for a 20 µm radius microring laser following the application of a 10 mA step-impulse current

5.4.1 Process changes for better thermal response

The device design was modified to allow for better heat conduction from the device. The modifications primarily focused on partially or fully replacing the low thermal conductivity BCB layer used for wafer bonding. While direct wafer bonding would have provided the best solution, the lack of appropriate process and equipment resources forced the development of an approach utilizing high conductivity bonding layers. A review of different bonding techniques can be found in ref. [106].

In the first approach, silicon nitride was used as a substitute for BCB. Silicon nitride has a bulk thermal conductivity (k_{th} ~ 30 W/Km) over two orders of magnitude larger than BCB [107]. A thick layer of about 1 μm was deposited on the bus waveguides in an HDPECVD system. This was then planarized by chemical-mechanical polishing to provide for a flat bonding surface. Since direct bonding using silicon nitride requires extremely clean and flat surfaces, a low melting point solder such as Au-Sn (MP 225 °C) eutectic alloy was tried for wafer-bonding [108]. However, the high stress/strain associated with the use of hard-solder such as Au-Sn results in damage to the semiconductor. The bonding interface showing the semiconductor crystal damage and void formation when using a hard-solder such Au-Sn is shown in fig. 4.9a.

In order to avoid the drawbacks of using a hard-solder, a soft-solder such as indium metal (MP 158 °C) was tried as the bonding medium [109]. While the bond itself and associated semiconductor interfaces fare much better, indium is not suitable for subsequent high-temperature processing, such as rapid thermal annealing (400 °C) used to alloy contacts. The melting and reflow of indium during annealing causes the thin epilayers to buckle and warp. Figure 5.9b shows the bond interface using indium as the

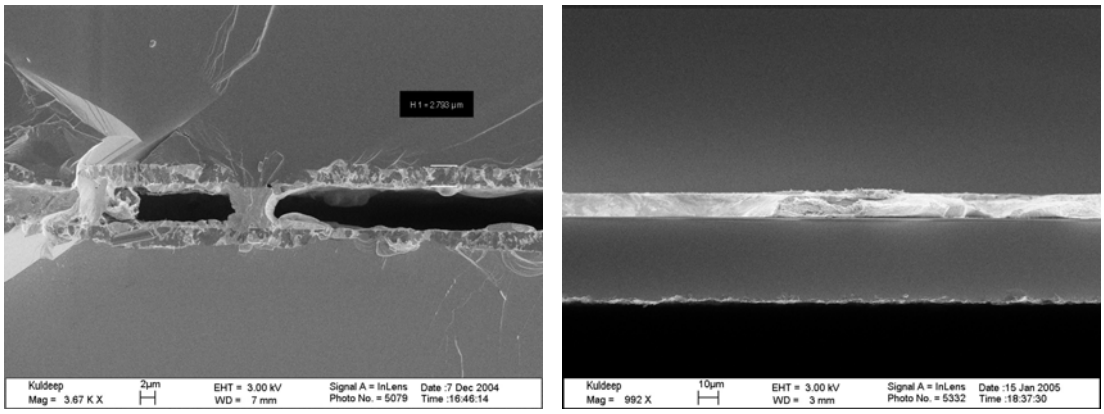

Figure 5.9: SEM scan of semiconductor-metal interface for wafer-bonding done using (a) Au-Sn eutectic alloy. Hard solder stresses the bonded semiconductors besides producing voids (b) Indium solder. A stress free interface with relatively few voids is obtained.

bonding layer.

A more viable solution was to deposit a thick layer (~1 µm) of silicon nitride on the bus-waveguide side followed by chemo-mechanical planarization and use a very low viscosity grade of BCB as the bonding polymer. The low viscosity produces a very thin bonding layer (~300 to 500 nm), while the high thermal conductivity silicon nitride enables conduction of heat laterally away from the device. This is schematically illustrated in figure 5.10. Test ridge lasers were fabricated using this method to test its efficiency. The threshold current for the control device with just the BCB layer and the modified design with the silicon nitride layer is illustrated in figure 5.11. The lower threshold observed for the second device indicates the effectiveness of the heat sinking. While improved thermal performance is seen in the test lasers, the thick poly-crystalline silicon nitride makes it difficult to produce good quality facets by cleaving.

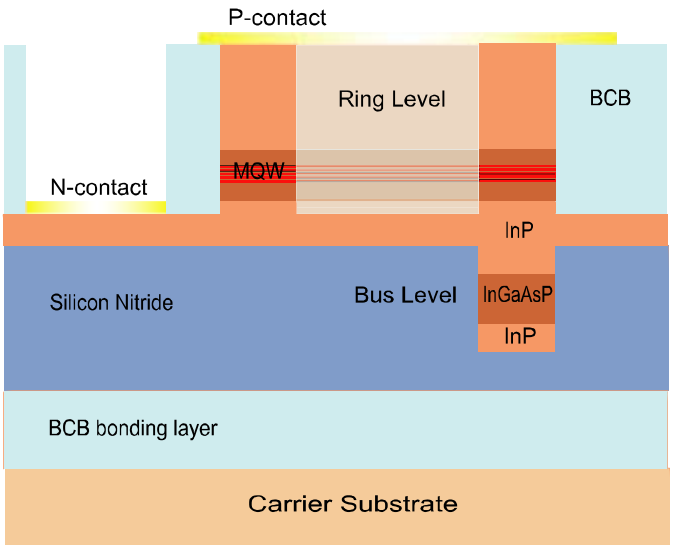

Figure 5.10: Schematic cross-section of device with improved heat-sinking scheme. The silicon nitride layers help in the lateral conduction of heat away from the ring.

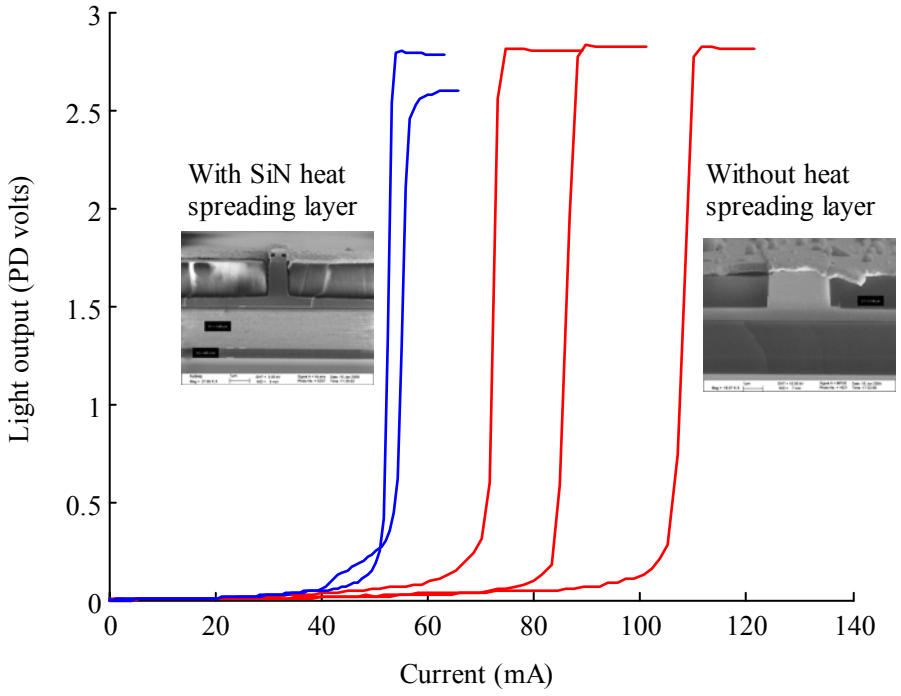

Figure 5.11: Comparison of threshold currents for 1000 µm long, 3 µm wide, test InP ridge lasers with (blue) and without (red) silicon nitride heat spread layer. Both lasers are wafer bonded using BCB. Photodetector power calibration is 16.3 µW/V at λ = 1550 nm.

Chapter 6

OPTICAL SWITCHING IN PSEUDODISK RESONATORS

Vertically coupled active microrings fabricated by polymer wafer bonding have two major disadvantages. The first is poor heat dissipation. The energy generated by ohmic heating has to dissipate mostly through the narrow bottom of the ring, where it can only spread laterally through the thin mid-layer. There is very little heat conducted to the substrate through the BCB wafer bonding layer. At the top, heat conduction through the contacts is limited by the thin (300 nm) metal layers. The other major disadvantage is surface recombination. There are two surfaces, the inner and outer walls of the ring, on which carriers can recombine and generate waste heat. In this chapter, I discuss a novel microdisk resonator scheme which addresses these two issues and present results from non-linear optical switching experiments based on these devices.

6.1 Motivation for Microdisks

In a microdisk, optical waveguiding occurs by total internal reflection along the periphery and hence an inner wall is not necessary. The transfer response of a microdisk is nearly identical with a microring of the same radius for the fundamental mode. The advantages of using a microdisk in place of microring are in improved heat conduction and lowered surface recombination. The large area of a microdisk provides better heat conduction away from the disk periphery, where the optical mode exists. Also, the larger

thermal mass ($C_s m$) means smaller temperature rise for the same energy dissipation. By combining the use of a microdisk with a monolithic architecture such as the laterally coupled scheme, where the microdisk is part of the original substrate, heat dissipation can be made much higher than the vertically coupled, polymer bonded, microring scheme.

The other advantage lies in reduced surface recombination as the inner side-wall no longer exists. Consequently, carrier loss to surface recombination is approximately halved. The absence of an inner side-wall and associated surface recombination also means that the carrier density is higher in that region. Thus, the optical mode overlap with the gain producing carriers is also correspondingly higher. This is illustrated in figure 6.1.

One of the disadvantages of using a microdisk is carrier recombination losses away from the periphery. As mentioned before, the optical mode exists mostly along the perimeter of the disk. However, the disk is pumped electrically uniformly throughout its top and bottom surfaces. This results in a large reservoir of carriers in the middle of the disk that do not contribute to the optical gain at the periphery. The carriers in this reservoir undergo wasteful recombination by spontaneous emission as well as non-radiative mechanisms like Auger and mid-band-gap defect recombination. Depending on the recombination rates and diffusivity, a significant percentage of carriers can be lost before they reach the periphery. Thus, for very large radii, it might actually be more efficient to switch to a microring structure. For lower radius microdisks, the increased optical gain and lowered surface recombination can more than compensate for the carrier losses in the middle of the disk. For the range of radii of devices in this study, most of the carriers diffuse to the periphery before recombination and hence a significant advantage

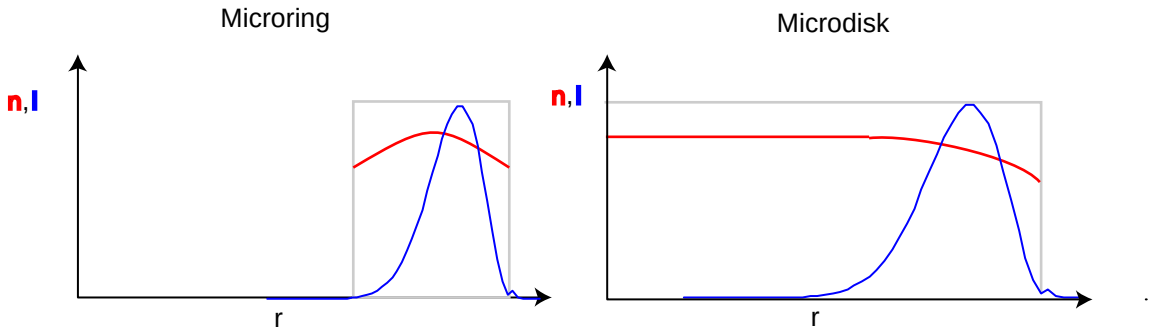

Figure 6.1: Schematic comparing optical mode intensity (blue) and carrier concentration profile (red) between microrings and microdisks. Microdisks do not have surface recombination on the inner side-wall unlike microrings.

was realized by switching to the disk architecture. The exact critical radius (R_c), beyond which rings become more efficient than disks is strongly dependent on the various material recombination and transport properties (Auger, SRH, spontaneous emission, diffusion coefficient), which are determined by growth quality as much as intrinsic material properties.

The other disadvantage of using a microdisk is the large number of lateral modes present unlike a microring structure, where the inner wall reduces the numerical aperture of the waveguide and consequently the number of supported modes. Power from the bus-waveguide and the fundamental mode of the disk couples into the higher order lateral modes resulting in a complex through-port response. The resonances of the higher order modes are at different wavelengths and consequently any optical switching based on resonance wavelength modulation by non-linear optical effects is also affected, especially the on-off contrast ratio. Figure 6.2 shows the simulated fundamental and higher order modes in a 20 μm radius InP microdisk. The higher order modes extend farther into the disk from the periphery than the fundamental mode. This fact is made use of in the present study to design the pseudodisk structure, where the higher order lateral modes are

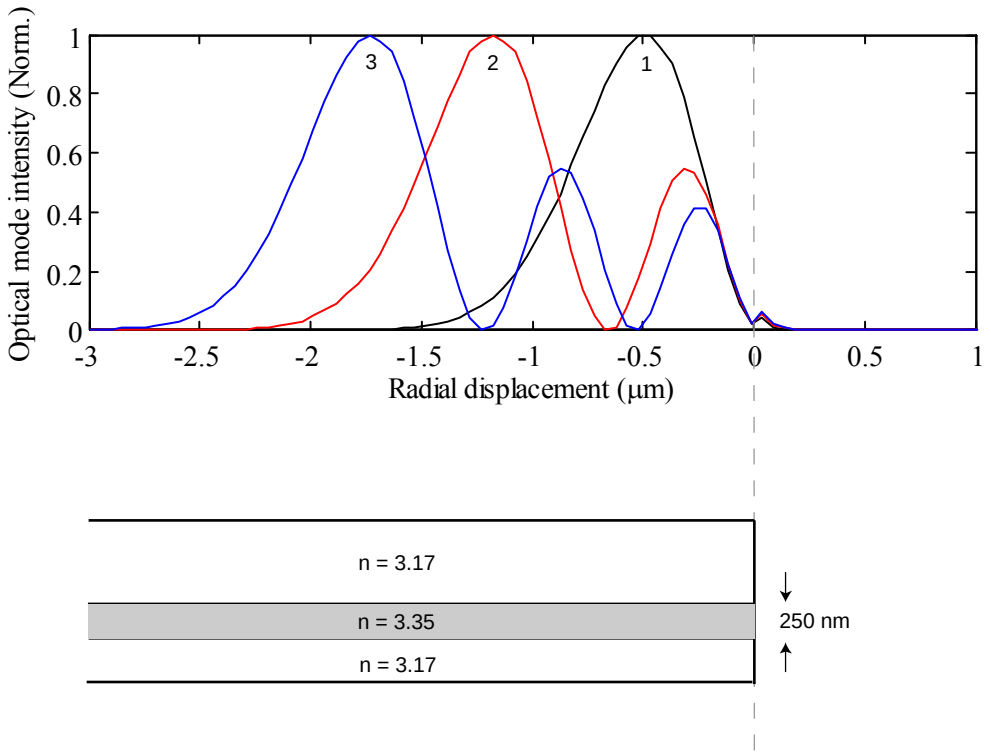

Figure 6.2: Simulated optical intensity for the first three lateral modes in a 20 μm radius microdisk. For higher order modes the energy resides more towards the disk center.

blocked by including a trench or hole etched into the disk at an appropriate location away from the sidewall.

6.2 Pseudodisks

In this program, the pseudodisk architecture was developed as an alternative to microdisks to combine the best of microrings and disks. Specifically, the device was designed to retain the superior heat-sinking and lower surface recombination capability of the microdisk with the single-mode capability of the microring. This is accomplished by etching a trench or hole into a laterally coupled microdisk near the junction with the bus waveguide. The trench is sufficiently away from the side-wall to allow for the

fundamental mode to pass through without much attenuation but restricts the passage of the higher order modes. The various schemes are illustrated in figure 6.3. The transition from a disk like optical-mode to a ring-like waveguide needs to be slowly tapered to prevent losses from scattering at an abrupt interface. The tapering can be done by either having a circular hole such as in figs. 6.3c and 6.3d, or a curved trench with rounded corners (fig. 6.3b). Figure 6.4 shows a schematic cross-section of a laterally coupled active pseudo-disk with separately biased bus-waveguides. The lateral coupling scheme greatly simplifies the fabrication.

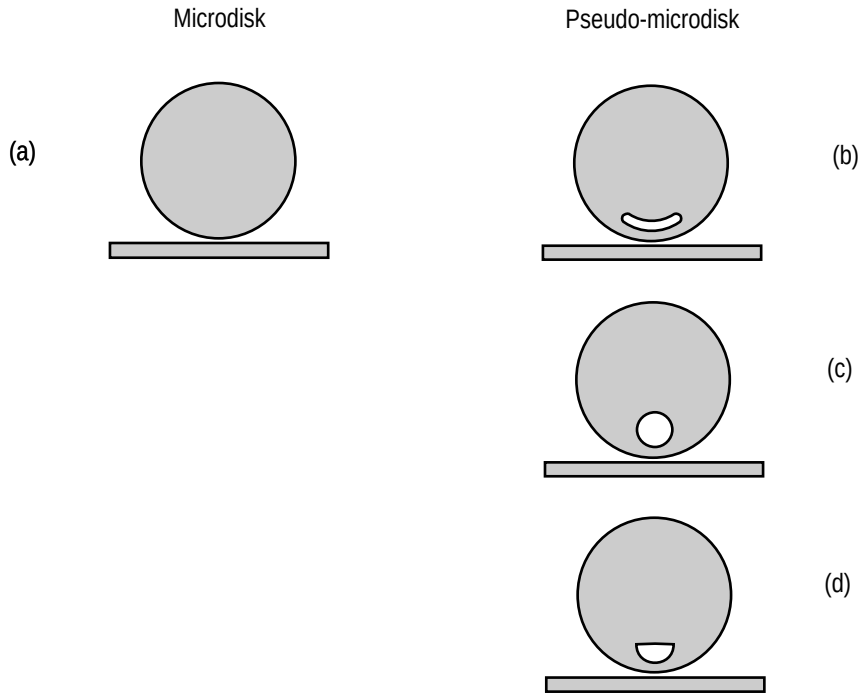

Figure 6.3: The standard microdisk structure laterally coupled to a bus waveguide. (b), (c), (d) Psueudo-microdisk structures that filter out higher order lateral modes.

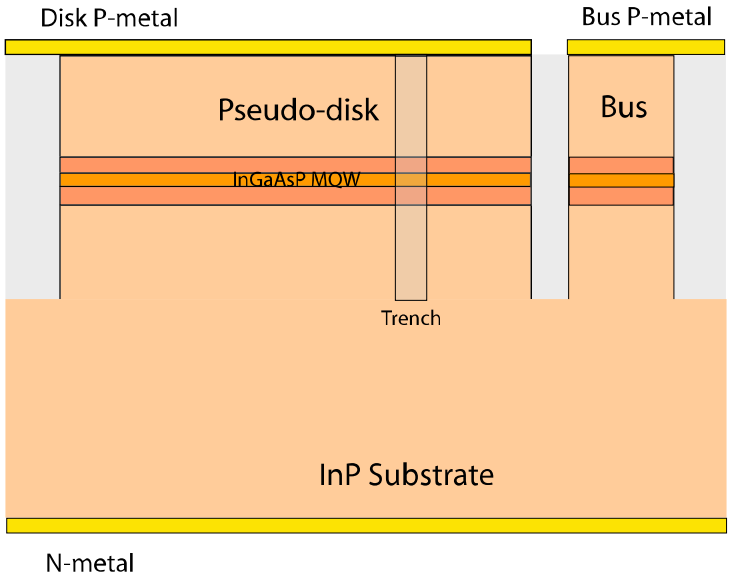

Figure 6.4: Schematic cross-section of a laterally coupled pseudodisk showing etched trench and separately biased bus-waveguide. The microdisk is now part of the substrate and hence has better heat-sinking.

6.2.1 Negative gap coupling

Another variation from the standard disk structure developed in this program is negative gap coupling. Normally, there is a small gap (~ 200 nm) between bus and ring waveguides in laterally coupled schemes that determines the coupling strength. Recently, it was demonstrated that reducing this gap to zero or even below zero (bus-waveguide overlaps with ring-waveguide) still provided good control on the coupling strength [110]. This is a critical difference in that the small gaps are beyond the resolution capability of conventional photo-lithography and hence have to be done via e-beam lithography. However, in negative gap coupling, the fused bus and ring waveguides means that conventional photo-lithography can be used to define the structures. Figure 6.5 is a graph of the calculated coupling as a function of the gap between bus and ring waveguide of radius 10 μm for an ideal junction. Notice how for gaps below zero, there is still good control of the coupling strength with gap. In such fused gap schemes, the junction essentially behaves as a multi-mode interference (MMI) coupler [111]. The coupling of power from one waveguide to another can be analyzed using the multi-mode interference techniques as has been done in MMI couplers. The placement of the trench or hole near the bus-waveguide essentially transforms the microdisk junction region to an MMI type coupler when negative gap coupling is used. In a real junction, the non-ideality arises from the rounding of sharp points due to lithography limits. This results in slightly higher losses due to scattering from the rounded corners.

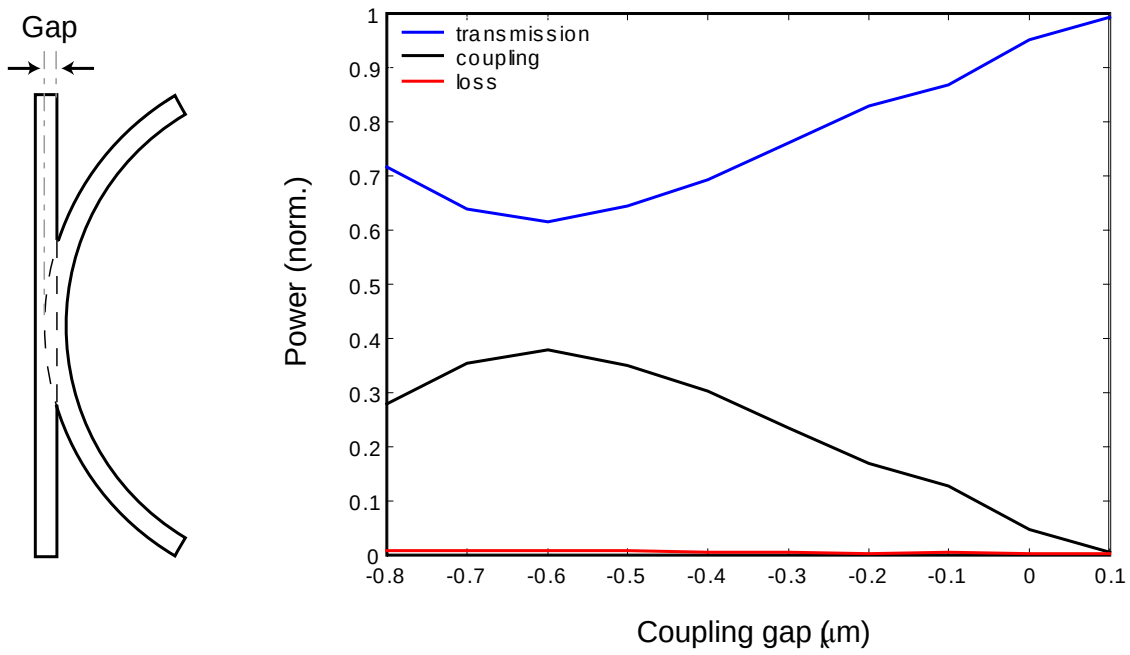

Figure 6.5: Coupling between bus and ring waveguide in an ideal junction for negative gap size calculated using 2D FDTD simulations. The waveguides are 1.2 μm wide and the radius of the ring is 10 μm.

6.3 Optical Design of Pseudodisks

In this section, I will present results from the numerical analysis of various pseudo-disk designs and optimization. The 2D-FDTD simulations were carried out using APSS (Apollo Photonics Solutions Suite), a commercially available software from Apollo Photonics [112]. The typical simulation takes about 20 to 30 hrs to complete, especially because of the large wavelength range over which the device response has to be calculated. So the range of parameters has to be chosen judiciously to glean as much information as possible with fewer simulations. I am grateful to Dr. Tie-Nan Ding (LPS) for help with the simulations.

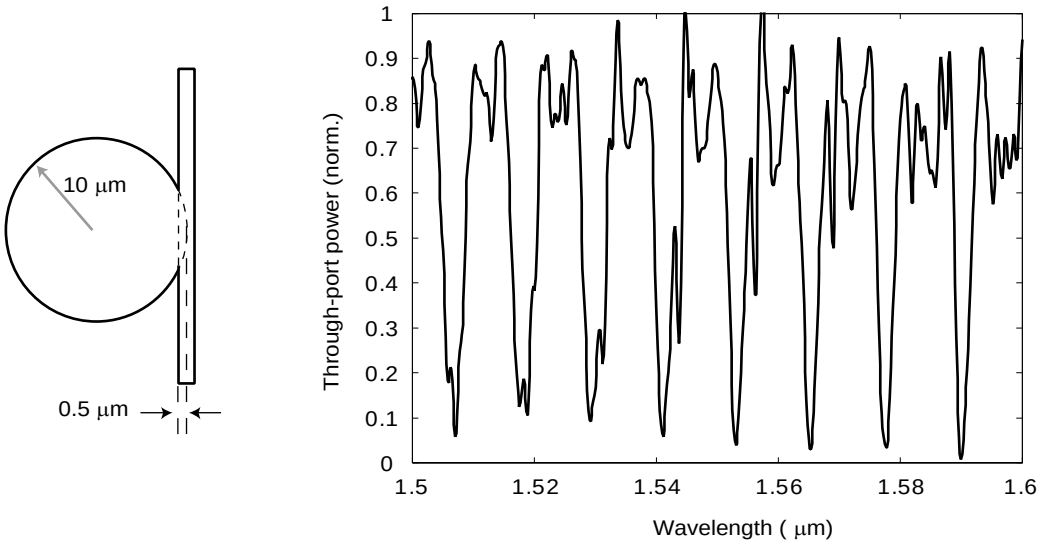

Figure 6.6: Simulated through-port response of a 10 μm radius microdisk coupled to a bus-waveguide with a negative gap of -0.5 μm. The response has multiple sets of resonances from higher order modes.

6.3.1 Mode control in pseudodisks

The starting point for the design is a standard microdisk resonator laterally coupled to a bus waveguide. Figure 6.6 is a graph of the through-port response for a 10 μm radius microdisk with gap of -0.5 μm. Notice how the transmittance has a fairly complex variation with wavelength with multiple sets of resonances due to contributions from many higher order lateral modes. This is a result of power coupling from the bus waveguide to the higher order modes at the junction region. Next, a 2 μm wide trench is inserted into the microdisk at a distance of 1.2 μm from the disk wall near the junction. This has the effect of blocking the higher order lateral modes. Figure 6.7 is a graph of the through-port response from a trench type pseudodisk. Notice how the number of higher order resonances is greatly reduced. A similar response is obtained for pseudodisks with a hole or a half-hole instead of a narrow trench.

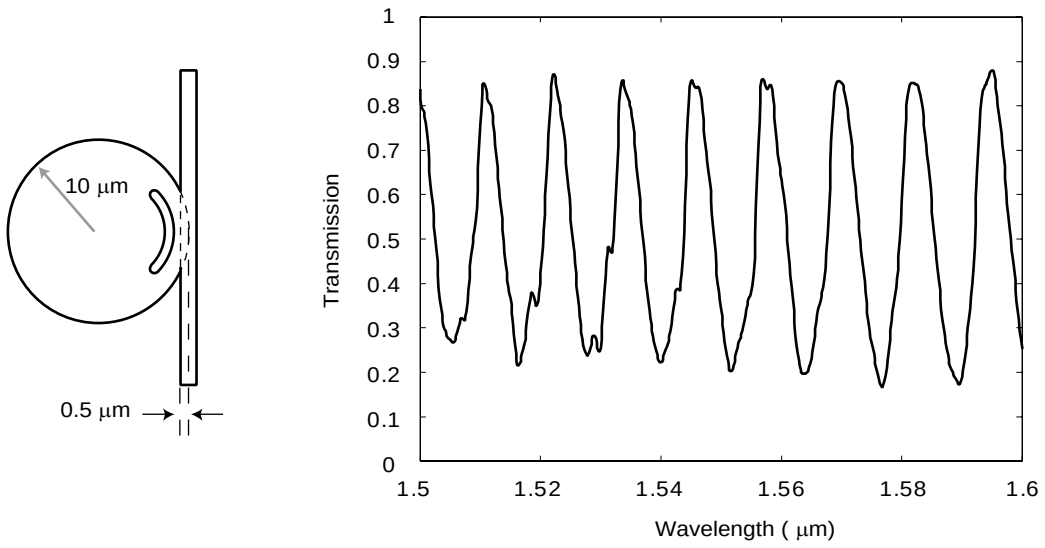

Figure 6.7: Simulated response of a 10 μm radius pseudodisk with trench and negative gap of -0.5 μm. The effects of higher order lateral modes are greatly reduced.

6.3.2 Laterally coupled pseudodisks with passive waveguides

In the laterally coupled pseudodisk scheme illustrated in fig. 6.4, the bus-waveguide has an active core too and hence has to be biased separately from the disk to transparency. This increases the current drawn by the devices as well makes the optical signal noisier due to spontaneous emission from the bus waveguides. An alternate scheme was developed, in which the gain producing quantum wells are offset from the center of the core towards the top and then etched away in the bus waveguides to make them passive. Near the pseudo-disks, the waveguides transition from a passive structure to an active one by introducing the upper active sections through a gradual taper as illustrated in figure 6.8. The advantage of this structure is that it allows for the disks to be active while still keeping the bus waveguides passive in a laterally coupled scheme. The laterally coupled structure is much easier to fabricate compared to the vertically coupled one.

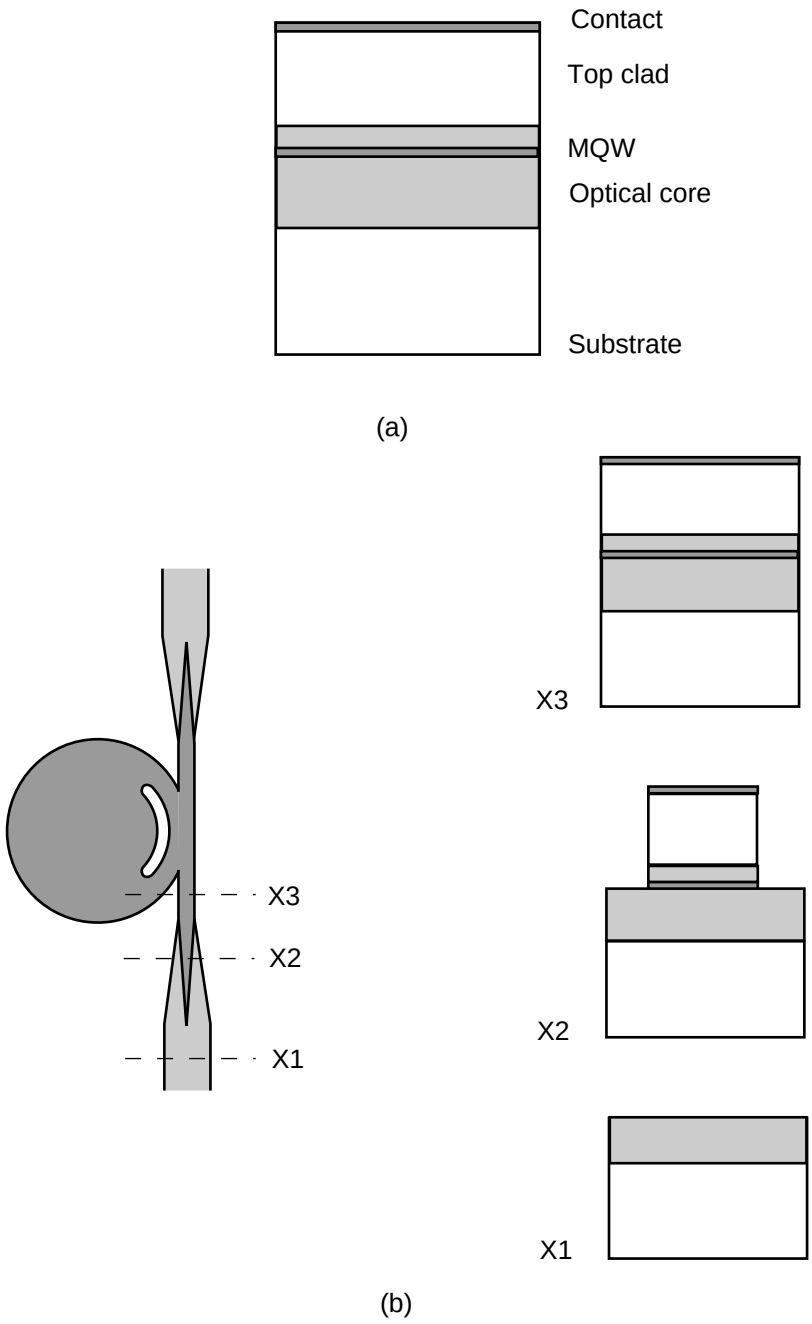

Figure 6.8: (a) Layer structure for the laterally coupled active disk, passive bus device scheme. (b) Pseudodisk and waveguide structure showing cross-sections at various points along the bus waveguide. The active region is etched away in the bus-waveguides.

The main disadvantage is the reduced optical mode overlap with the quantum wells. Since the quantum wells are no longer at the peak of the optical mode intensity and the optical confinement layer (core) has to be made thicker to accommodate the bus-core, the fraction of the mode intensity which overlaps with the gain producing quantum wells (Γ) also drops. Thus, net modal gain is lowered. The other disadvantage is that the bus-waveguides now need to be etched very deep to prevent light leaking to the substrate. The effective index of the optical mode in the bus-waveguide is lower than before and hence the light leaks into the high index substrate layer unless separated by a large distance. Also, both the sidewalls and upper surface of the bus-waveguide are defined by a plasma etch, which increases the optical loss due to scattering from etch induced surface roughness.

6.4 Fabrication

The fabrication of the laterally-coupled pseudodisks with separately biased waveguides is much simpler compared to the vertical coupling scheme described in chapter 3.

6.4.1 Epitaxy

The epitaxial structure is similar to the standard layer structure used in InP 1550 nm semiconductor lasers. The layer structure used for these devices is shown in figure 6.9. The epitaxy was done in the solid-source MBE facility at the Laboratory for Physical Sciences, MD and was originally grown for making ridge lasers. The growth begins with a short buffer layer of n-doped InP followed by the optical core. The core is a 150 nm thick undoped InGaAsP quaternary that serves as both the optical and carrier confinement

100 nm $Ga_{0.47}In_{0.53}As$		$p = 1 \times 10^{19}$ cm^{-3}	P contact
1000 nm InP		$p = 5 \times 10^{17}$ cm^{-3}	Top clad
10 nm $Ga_{0.27}In_{0.73}As_{0.57}P_{0.43}$		$p = 5 \times 10^{17}$ cm^{-3}	Etch stop
350 nm InP		$p = 5 \times 10^{17}$ cm^{-3}	Top clad
20 nm InP		$p = 1.5 \times 10^{18}$ cm^{-3}	
45 nm $Ga_{0.27}In_{0.73}As_{0.57}P_{0.43}$		i	Optical core
9 nm $Ga_{0.27}In_{0.73}As_{0.57}P_{0.43}$	**x 3**	i	QB
9 nm $Ga_{0.27}In_{0.73}As_{0.80}P_{0.20}$	**x 4**	i	QW
45 nm $Ga_{0.27}In_{0.73}As_{0.57}P_{0.43}$		i	Optical core
InP		$n = 5 \times 10^{17}$ cm^{-3}	N gradient, Buffer
InP Substrate		$n = 3 \times 10^{18}$ cm^{-3}	(100) Substrate

Figure 6.9: Epitaxial layer structure of laterally coupled pseudodisk devices. The layer structure is similar to that used in InP/InGaAsP 1550 nm diode lasers.

layer. Four quantum wells and barriers are located at the center of core for providing optical gain. An approximately 1400 nm thick p-doped InP clad layer is grown above the core and serves to keep the contacts away from the core. The contact layer is a 100 nm thick heavily p-doped InGaAs ternary.

6.4.2 Fabrication steps

The major steps in the processing of the laterally coupled pseudodisks are outlined in this section. The details of the procedures are similar to those described in chapter 3.

- Begin with cleaved-off 15 mm x 15 mm wafer-piece with epitaxial growth.
- Deposit 500 nm of silicon dioxide etch-mask in an HDPECVD system.
- Pattern photoresist on the wafer by photolithography to define the bus and disk structures.
- Transfer resist pattern to silicon dioxide etch mask by reactive ion etching (RIE). Remove resist after etch using acetone and oxygen plasma 'ashing'.
- Etch the indium phosphide layers in an RIE system in methane-hydrogen-argon plasma using the silicon dioxide pattern as an etch mask. Etch depth is about 3 μm.
- Remove silicon dioxide etch mask in buffered hydrofluoric acid (BHF).
- Passivate the side-walls using Na_2S / Iso-propanol solution.
- Deposit 30 nm of silicon nitride in an HDPECVD system at 120 °C to cap the passivation.
- Planarize by spinning on BCB and cure at 225 °C for 2 hrs in nitrogen ambient. Etch back BCB in an RIE system to expose the top of the disks and waveguides.
- Pattern negative resist by photo-lithography to define the p-contact openings for the disks and waveguides.
- Evaporate Ti-Pt-Au with thicknesses of 100, 500, 3000 Å respectively in an e-beam evaporator to form the p-contacts for both disk and waveguide. Lift-off excess metal in acetone.
- Thin the wafer by mechanical lapping to about 150 μm thickness.
- Evaporate Ni-Ge-Au-Ni-Au with thicknesses of 50, 300, 800, 400, 2500 Å respectively on the backside of the thinned wafer to form the n-contacts to the device.
- Anneal the devices at 400 °C in a rapid thermal annealing system (RTA) for 40

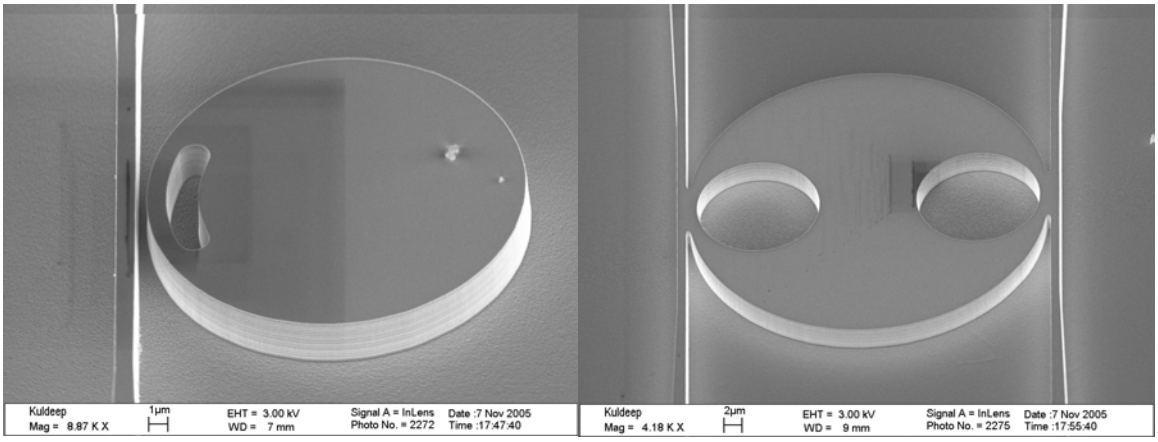

(a)

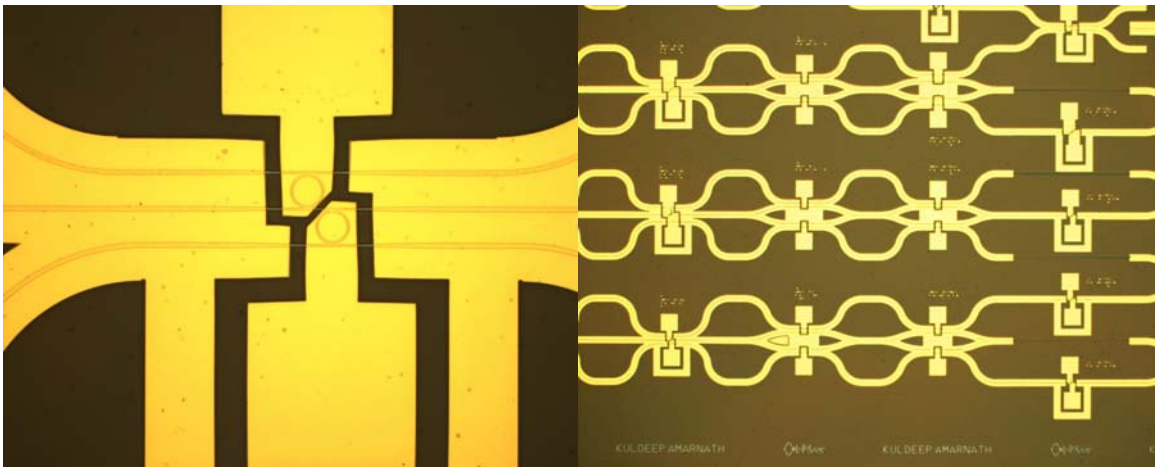

(b)

Figure 6.10: (a) SEM scans of pseudodisk structures following the indium phosphide RIE etch. On the left is a trench type pseudodisk and on the right is hole type coupled to two bus waveguides (b) Optical microscope pictures of fully processed devices. The left image shows a NOR gate with the disk and waveguides biased separately. The right image illustrates the cascading of individual gates to form photonic circuits.

seconds to alloy the contacts.

- Scribe the wafer using a laser scribing system and cleave into 800 µm wide bars.
- Mount the bars on a copper heat-sink using silver conducting epoxy.
- Deposit anti-reflection coating of Al_2O_3 on waveguide facets in e-beam evaporator.

6.5 Lasing in Pseudodisks and Microdisks

Following fabrication, the devices were tested for lasing in pulsed mode. The test-setup is the same as in figure 4.1. The pulse width was 5 μs at 1 ms intervals. The optical output was measured through a 3 μs gate delayed from the start of the pulse by 1 μs. The devices were cooled to below room-temperature by means of a TE cooler. Only the current through the disk was pulsed. The bus waveguide was biased continuously.

6.5.1 Effect of the bus-waveguide current

The devices were tested for lasing both before and after AR coating the WG facets. The bus-waveguide bias was seen to play a significant role in the lasing characteristics for devices without AR coating. Adjusting the current through the bus has the effect of changing the loss or gain in the waveguide and hence modulates the effect of reflections from the uncoated facets. At low currents, the bus-waveguide is lossy and the effect of the waveguide facets is not seen. The lasing is confined to just the microdisk cavity. As the bus current is increased, the waveguide becomes transparent and the laser becomes a coupled cavity system. Increasing the current even higher introduces gain within the bus-waveguide and consequently the lasing threshold current (I_{disk}) drops to lower values. Figure 6.11 is a graph of the light output versus disk current (L-I) for 20 μm radius microdisk for various bus-waveguide currents (I_{bus}). The light output was collected by a lensed fiber aligned to the waveguide facet and fed to a photodetector. The lasing threshold is seen to drop for bus currents above a certain cut-off value. The cut-off value is determined by when the bus-waveguide approaches transparency. The transparency current was estimated to be around 30 mA for these devices. For bus

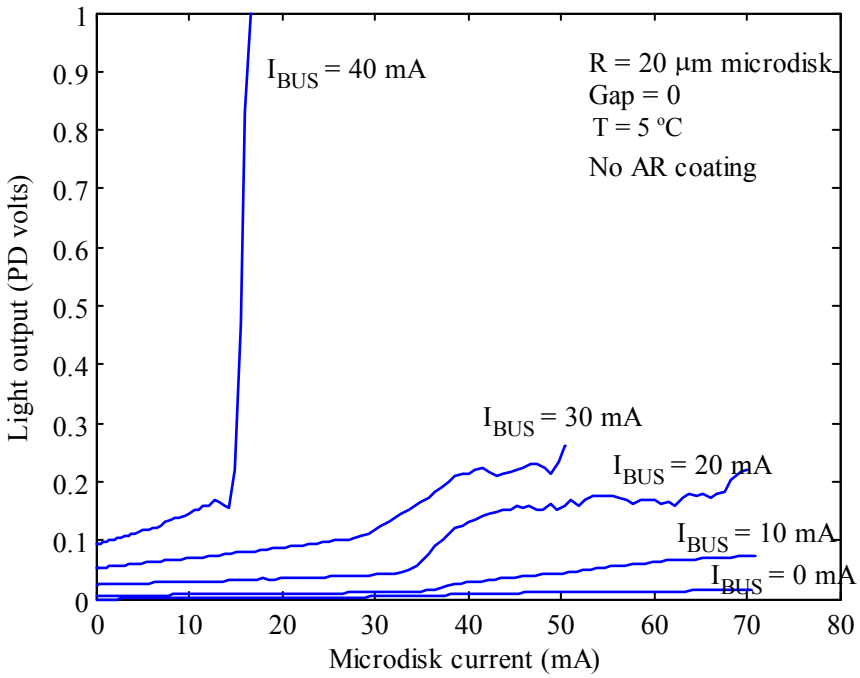

Figure 6.11: L-I curves measured in pulsed mode for 20 µm radius microdisk for increasing values of the bus current. For I_{bus} above 30 mA, the lasing threshold is seen to drop significantly. The photodetector (PD) calibration is 16.3 µW/V at λ = 1550 nm.

currents below the transparency condition, the lasing threshold current of the disks is seen to be almost constant. For devices with AR coating, depending on the effectiveness of the coating, the bus-waveguide current was observed to have a much lower influence on the threshold currents.

6.5.2 CW lasing and lasing spectrum

The improved design for better heat-sinking enabled continuous-wave (CW) operation of the devices without over heating. The L-I characteristic of a 20 µm radius microdisk measured in CW mode is shown in figure 6.12. The bus waveguide was biased at 20 mA, well below the value required for transparency thus minimizing influence of the waveguide facets on lasing characteristics. The TE cooler / heat-sink temperature was

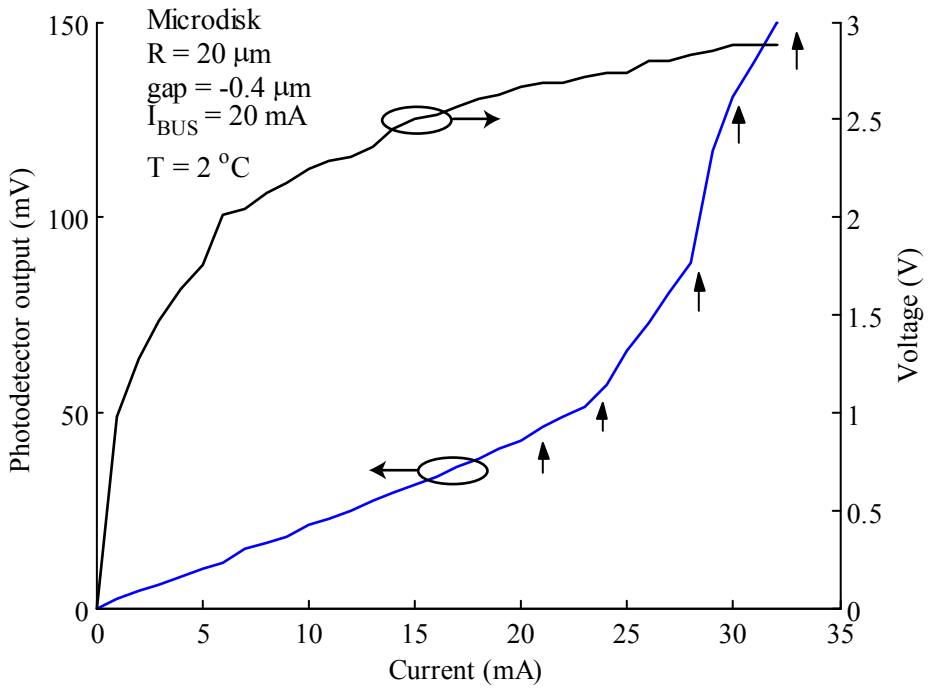

Figure 6.12: L-I characteristic (blue) measured in CW mode for 20 µm radius microdisk. The lasing spectrum was measured at the points indicated by arrows. The photodetector calibration is 16.3 µW/V at λ = 1550 nm. The black curve shows the V-I characteristic.

maintained at about 2 °C during the characterization. The output from the microdisk laser was collected using a lensed fiber and fed to an optical spectrum analyzer. Figure 6.13 shows the spectra at different currents. The corresponding current values on the L-I curve are indicated by arrows in figure 6.12.

The V-I characteristic is indicated by the black curve in figure 6.12. The differential resistance was measured to be about 25 ohms.

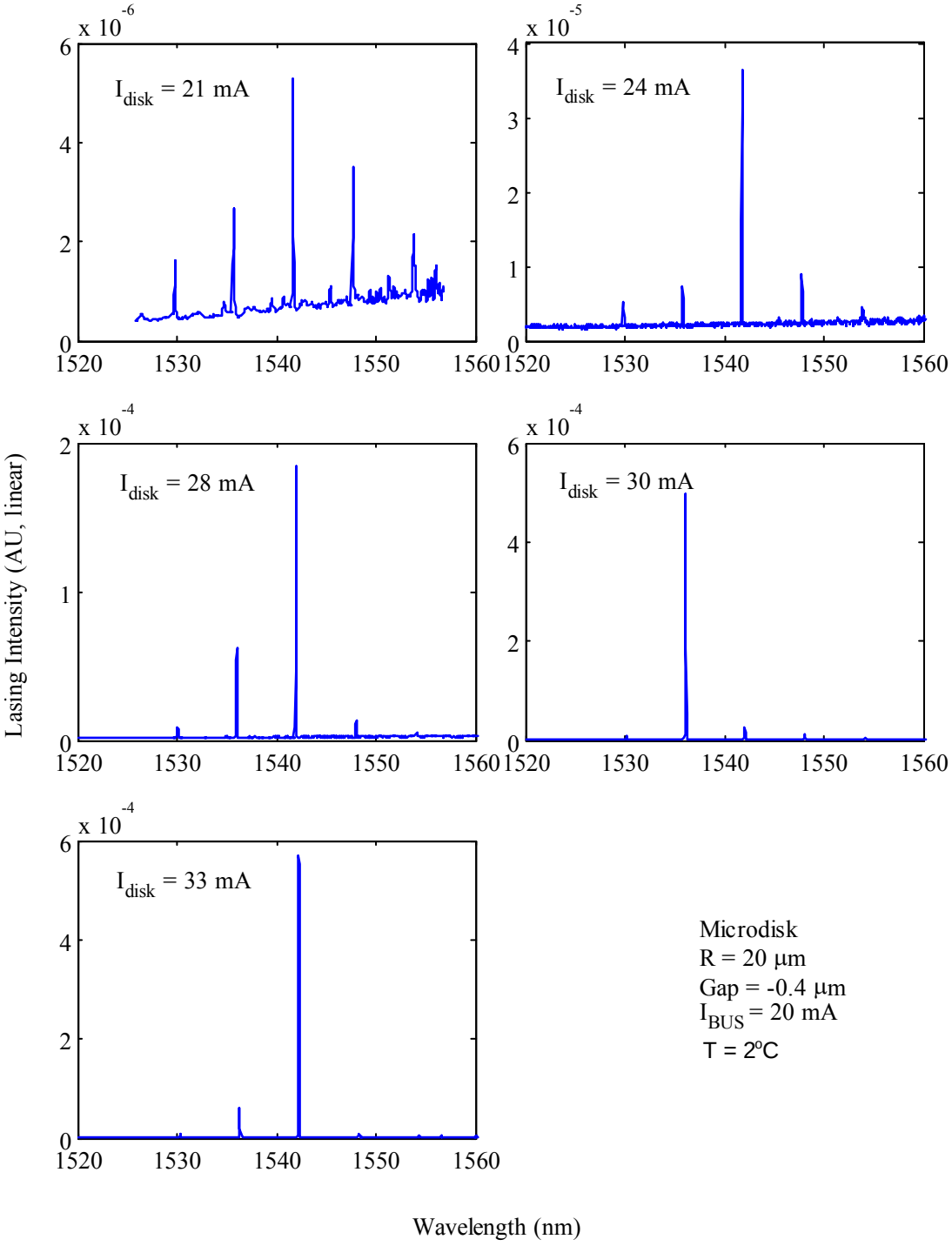

Figure 6.13: Lasing spectrum for a 20 µm radius microdisk resonator measured for various values of the device current indicated by arrows on the L-I curve in the figure 6.12.

6.6 Optical Non-linearity and Bistability

The non-linear transfer function of the devices was measured using the setup shown in figure 6.14. The goal of the experiment was to test for and characterize any optical non-linearity in the devices. For a linear device, the output optical intensity is related to the input as $I_{out} = k_{opt} I_{in}$, where k_{opt} is a constant and independent of the optical intensity. For a non-linear device, the input – output relation is more complex. The method of testing for this non-linearity is a simple experiment: a sinusoidal or triangular optical pulse is fed to the device under test and the output waveform recorded on an oscilloscope. If the output pulse is a scaled version of the input but with identical shape, then the device exhibits linear behavior. However, if the output pulse shape is distorted or different from the input, then the device exhibits non-linear behavior. In figure 6.13, the function generator modulates the out put of a tunable laser to produce a sinusoidal optical waveform. The laser is tuned close to one of the resonances of the micro/pseudo-disk. A polarization controller is used to orient the input polarization horizontally. A small fraction of the input power is tapped just before the input to the device and monitored on an oscilloscope. The output is collected through a lensed fiber and fed to a photo-detector, which is also monitored on an oscilloscope.

The devices were biased in CW mode below lasing threshold and the bus waveguides close to transparency. The measurement was carried out on devices with and without AR coating. The measurements were also done for various device currents to gauge the effect of gain on the non-linear characteristics. The measurement is repeated as the wavelength is stepped to scan across a resonance. Figure 6.15 shows the results from a 20 μm radius pseudodisk (hole-type) without any AR coating on the WG facets. The

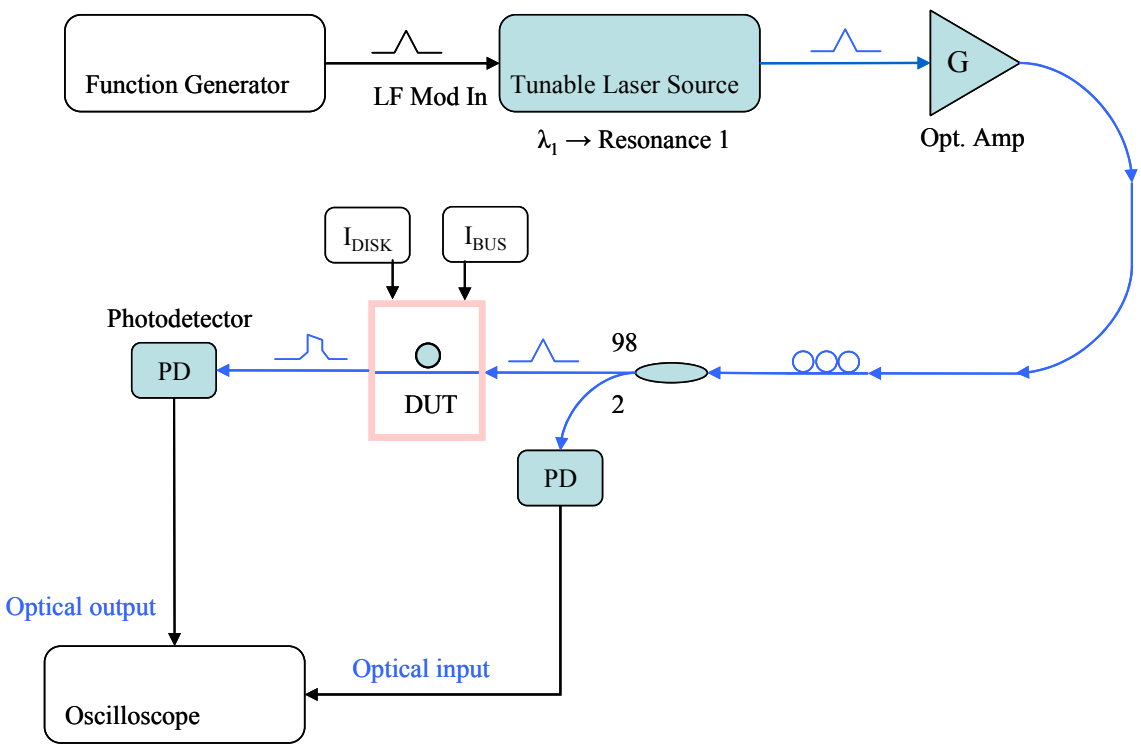

Figure 6.14: Schematic of test-setup used for optical non-linearity testing of pseudo/micro-disk devices. Optical paths are indicated in blue and electrical paths in black.

disk is biased at 25 mA while the bus is at 30 mA (disk / waveguide area ratio ~ 0.5). The heat-sink / TE cooler temperature was maintained close to 2 °C during the experiment. The average optical power is about 3.1 mW at the output of the optical amplifier. The actual power in the waveguide near the disk is estimated to be 8 to 10 dB lower. The graph is a plot of the output waveform at different wavelengths. The resonance wavelength is located close to the start of the wavelength axis on the graph at about 1560.27 nm. Three significant features can be noticed on the graph. As the wavelength approaches the resonance (< 1560.43 nm) and till the resonance peak, the output waveform is seen to distort from the sinusoidal form. The distortion consists of a sharp upward transition in intensity when the intensity reaches a certain threshold point,

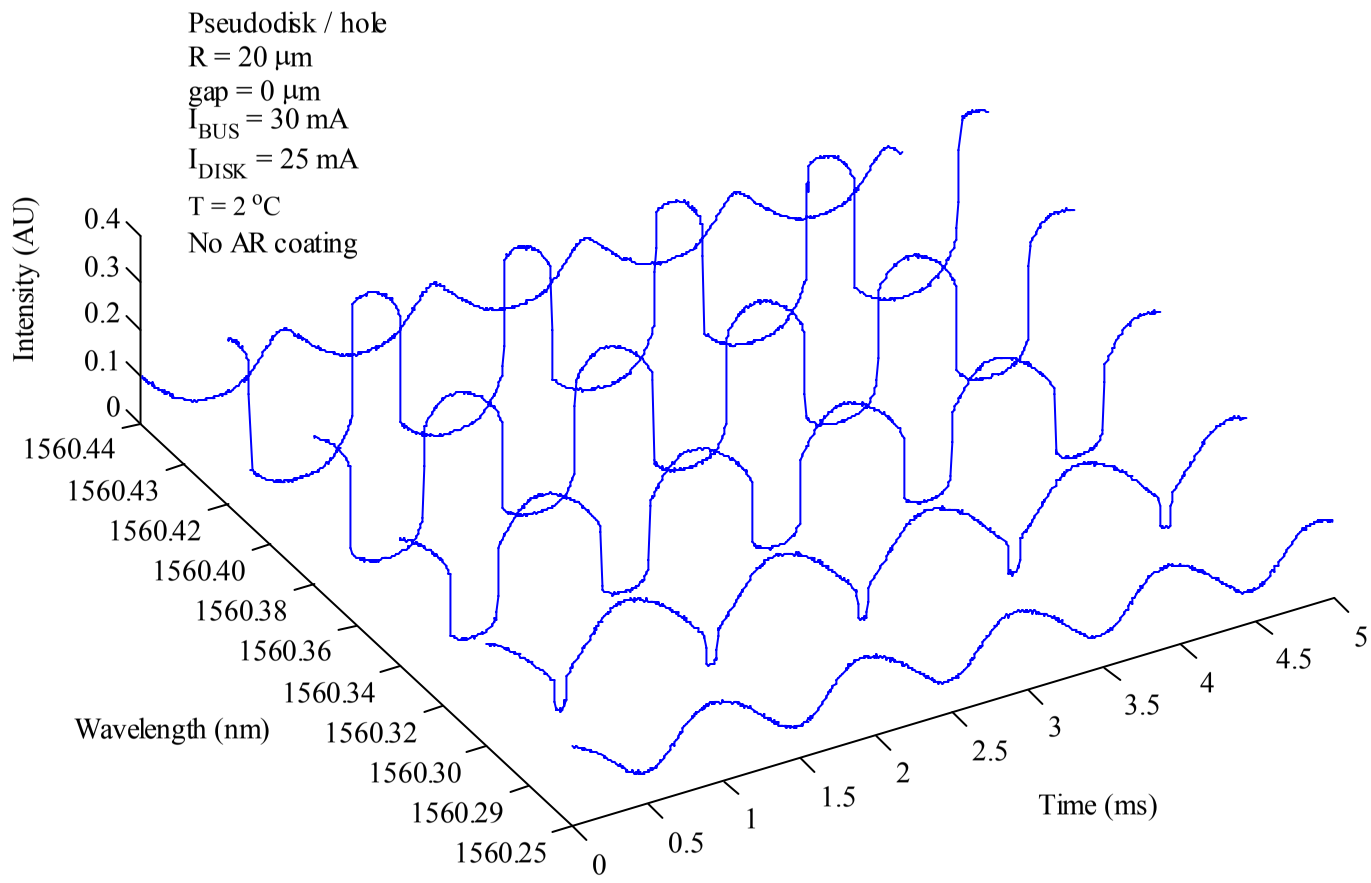

Figure 6.15: Optical output waveform from a 20 µm radius pseudodisk for different wavelengths near the resonance peak. The input is a sine wave. The disk is biased at 25 mA and the bus at 30 mA. The resonance peak is located near 1560.29 nm.

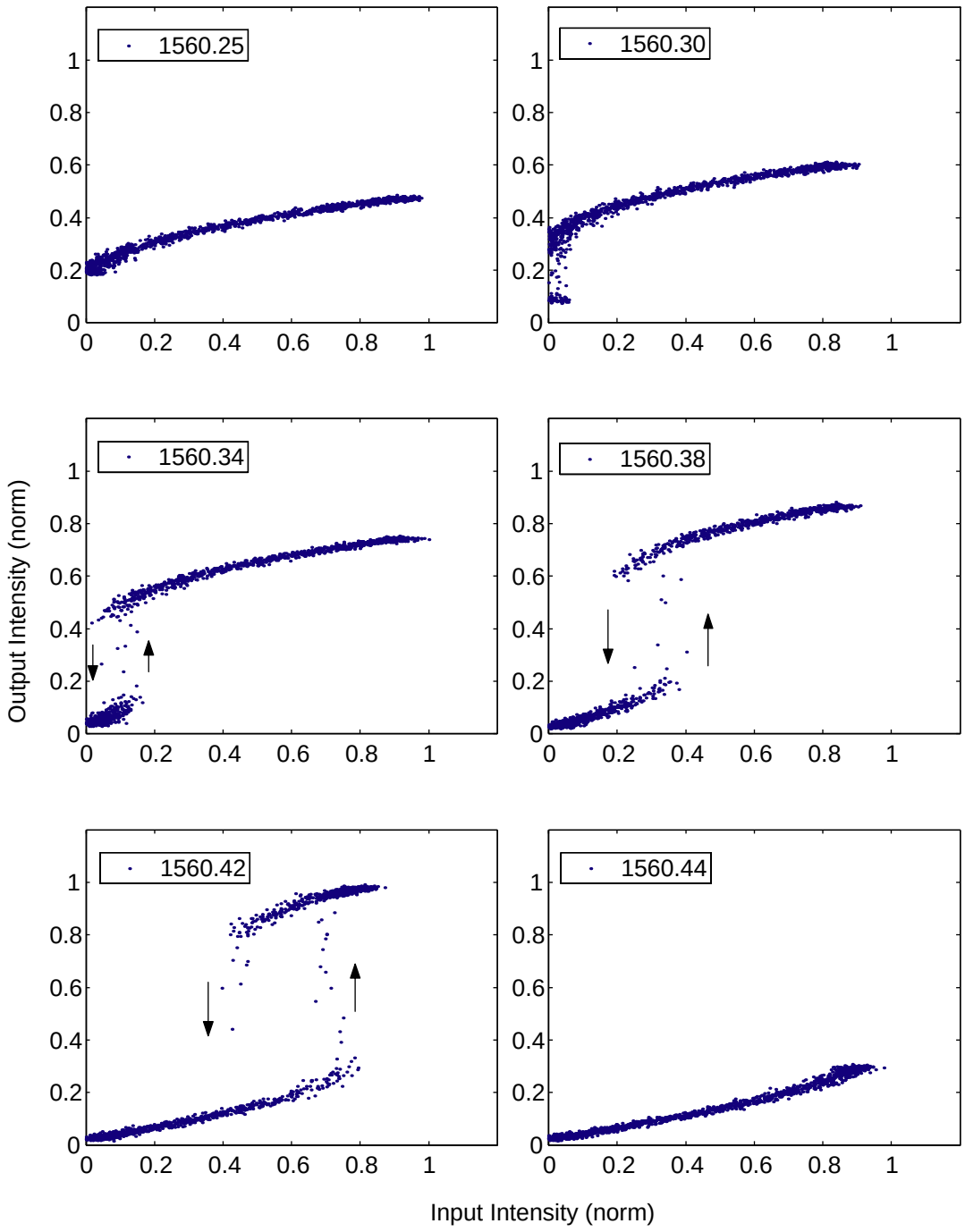

Figure 6.16: Through-port optical intensity response at different wavelengths for a 20 µm radius pseudodisk showing a non-linear through-port response. The data and experiment conditions are the same as in figure 6.15.

followed by sharp downward transition a little later when the intensity drops below a second threshold. The second important feature to be noticed is that the threshold points at which the transitions happen occur at lower intensities as the wavelength approaches the resonance peak. Third, the thresholds for the upward and downward transitions are not the same value. Figure 6.16 is a plot of the output intensity plotted as a function of the input intensity using the data in figure 6.15. Two things are apparent from this graph. One is the non-linearity of the transfer response of the pseudodisk. The other is possible bistable operation.

Decreasing the current through the device has the effect of lowering gain in the microdisk. Figure 6.17 shows a plot of the output waveform when the current is just a little above what is required to make the disk transparent. The disk current is 18 mA and the bus current at 30 mA. As the input wavelength approaches the resonance peak, the output intensity is seen to show strong non-linearity. However, instead of making an upward transition, like that in figure 6.15, the output intensity is seen to drop sharply for input intensity above a certain threshold. After a while, as the input intensity reaches a peak and begins to decrease, the output intensity is seen to make a sharp upward transition when the input intensity falls below a second threshold. As before, the two threshold points are seen to be different thus indicating possible bistable operation. Figure 6.18 shows the same data in a different format. Here the output intensity is plotted as a function of the input intensity for different wavelengths. The direction of the bistable operation is seen to be reversed, i.e. the hysteresis loop is oriented in the clockwise direction as opposed to the counter-clockwise operation in figure 6.16.

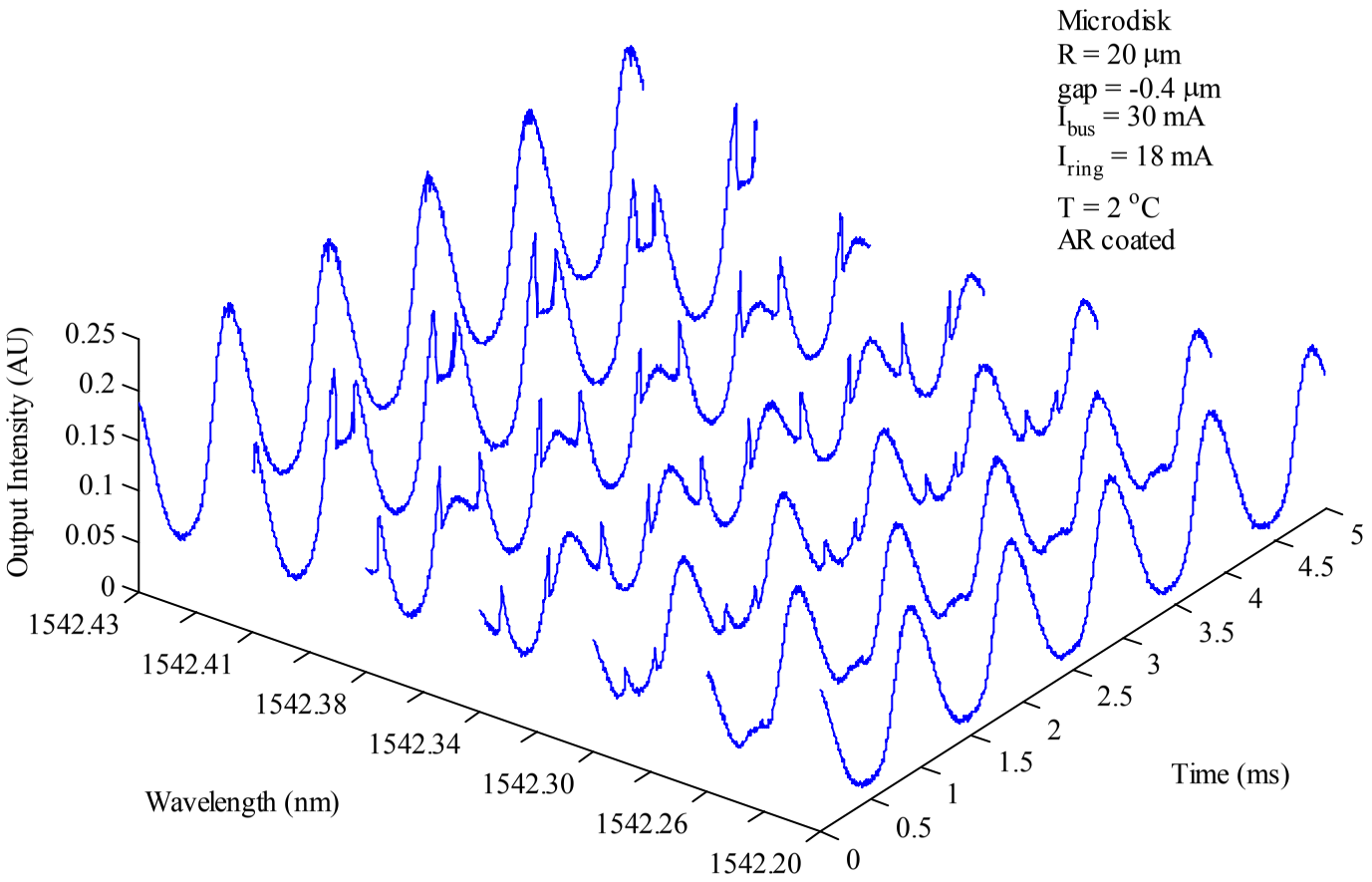

Figure 6.17: Optical output waveform from a 20 µm radius microdisk for different wavelengths near the resonance peak. The input is a sine wave. The disk is biased at 18 mA and the bus at 30 mA. The resonance peak is located near 1542.20 nm.

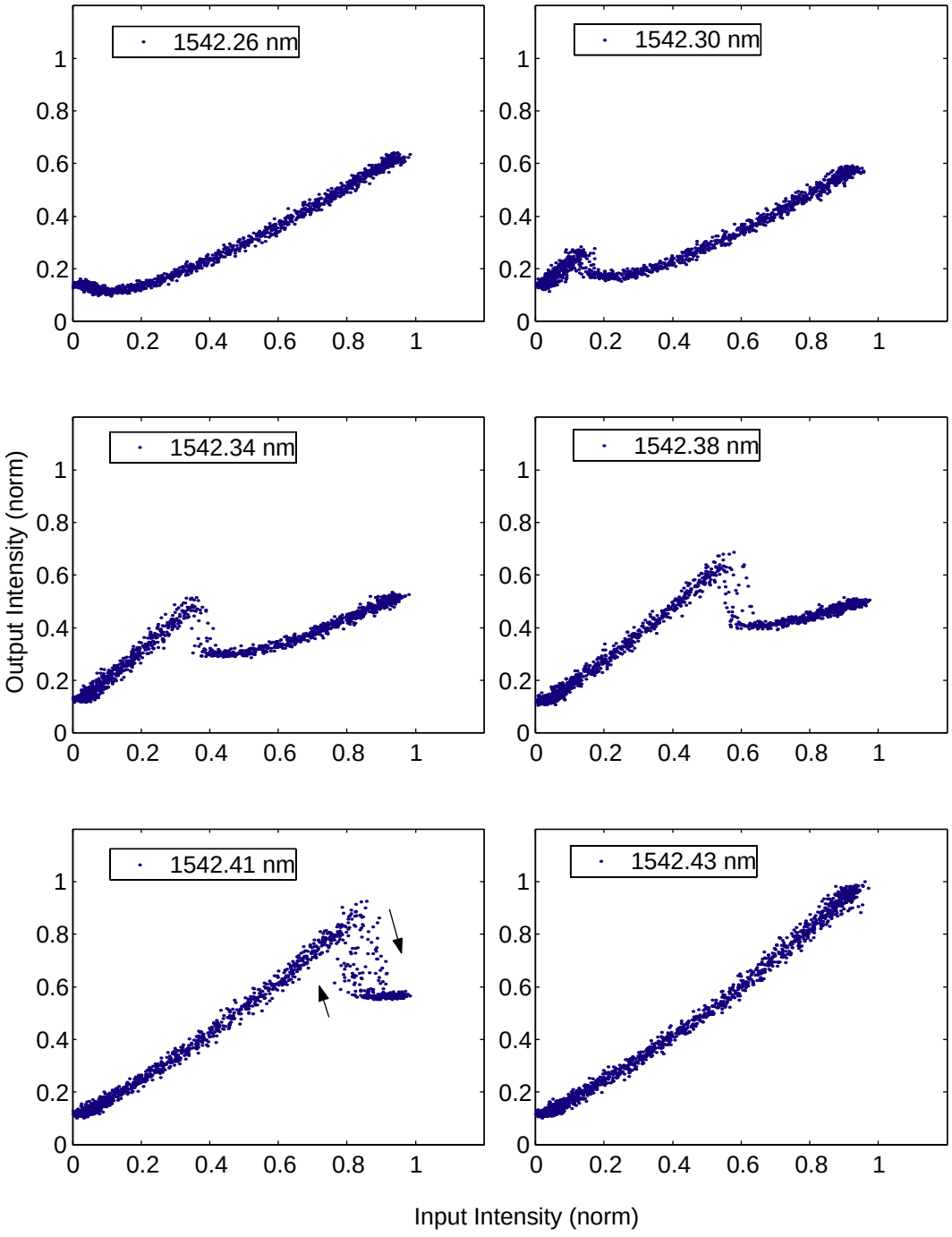

Figure 6.18: Through-port optical intensity response at different wavelengths for a 20 µm radius microdisk showing a non-linear through-port response. The data and experiment conditions are the same as in figure 6.17.

While the transfer characteristics are consistent with bistable operation, further experiments need to be done to conclusively establish bistability and attribute it to gain saturation and not thermal effects. Specifically, the transfer characteristics, shown in figures 6.16 and 6.18, need to be shown to be invariant with frequency of the input sinusoidal optical signal. An alternate experiment to confirm non-thermal bistable operation is by using a CW holding beam with intensity in between the two transition points and varying the output state by brief set – reset inputs.

In the next section, I will analyze the mechanism for non-linear switching seen in these devices and develop a model to simulate the switching behavior.

6.7 Modeling Optical Non-linearity and Bistability

The non-linear response indicated in the previous section is seen only when the wavelength is close to a disk resonance and on the long-wavelength side of the resonance. The response can be understood by considering how the gain saturation mechanism interacts with the disk resonances. Consider the case when the input wavelength is slightly red-shifted from the resonance peak. Since it is close to the resonance, the optical intensity in the disk resonator builds up. The disk is biased such that the quantum wells are in inversion and there is optical gain. Consequently the built-up intensity in the resonator undergoes optical amplification by stimulated recombination as it travels around the disk. The effect of the stimulated recombination is to decrease carrier density in the quantum wells, which in turn affects the refractive index. The refractive index increases due to (a) change in the plasma frequency of the electron/hole gas with carrier density (b) change in imaginary part of the refractive index (absorption/gain) and consequent effect on real part through the Kramers-Kroenig

relation [3]. The rising refractive index causes the disk resonances to shift towards the longer wavelength side or closer to the input wavelength. This in turn means that the intensity in the ring builds up even further and there is a net positive feedback. The positive feedback results in the resonance moving all the way to the input wavelength and past, till the input now lies on the shorter wavelength side of the resonance. Once the resonance moves past the input wavelength any further increase in input intensity only causes the resonance to move further away and the intensity amplification factor in the resonator drops. This 'snapping' of the resonance to the right is what causes the first sharp transition in the transfer response. When the input intensity begins to drop, the resonance peak begins moving back towards the shorter wavelengths and hence closer to the input wavelength. This has the effect of higher intensity amplification within the disk and hence a negative feedback. Consequently, the intensity in the disk remains more or less constant as the input intensity decreases. Below a certain threshold input intensity, when the resonance is exactly aligned with the input wavelength, the negative feedback effect no longer occurs and the resonance 'snaps' back due to positive feedback. This 'snapping' to the left is what causes the second sharp transition in the output waveform. To summarize, the positive feedback occurs when the input wavelength is red-shifted with respect to the resonance and negative feedback occurs when blue-shifted.

The whole phenomenon is inverted when absorption saturation is used as the non-linear effect instead of gain-saturation. Consequently, the non-linear transfer response is seen when the input wavelength is on the shorter wavelength side of the disk resonance.

The rest of this section deals with modeling the steady-state non-linear response from first principles and recreating the non-linear transfer function and bistability seen in

the experiments [113]. The starting point for the model is the disk optical intensity relations reproduced here for convenience.

$$I_t = I_{in} \cdot \frac{\tau^2 + a^2 - 2a\tau\cos(\phi)}{1 + a^2\tau^2 - 2a\tau\cos(\phi)} \tag{6.18}$$

$$I_R = I_{in} \cdot \frac{\kappa^2}{1 + a^2\tau^2 - 2a\tau\cos(\phi)} \tag{6.19}$$

Here, I_R, I_t, and I_{in} are optical intensities in the disk, at the through-port and input respectively. In a linear device, the round-trip gain (a) and phase (φ) are independent of the intensity within the disk. However, for the non-linear system, the round-trip gain is given by:

$$a = \exp(-(\Gamma g L - \alpha_{loss})/2) \tag{6.20}$$

The optical gain in the quantum wells (g) is dependent on the optical intensity in the disk and is given by the relation derived in chapter 2 (eqn. 2.26) and reproduced here:

$$g = \frac{g_0}{1 + I_R / I_{sat}} \tag{6.21}$$

Here, g_0 is the unsaturated gain in the quantum well, when there is zero optical intensity. The round trip phase (φ) is also dependent upon intensity in the ring and is given by:

$$\phi = \phi_0 + \frac{2\pi}{\lambda}\Gamma \cdot \Delta n(I_R) L \tag{6.22}$$

Here φ_0 is the initial detuning from resonance. $\Delta n(I_R)$ is the intensity induced refractive index change in the quantum wells and is given by the relation for gain saturation induced index shift derived in chapter 2 (eqn. 2.29) and reproduced here:

$$\Delta n(I_R) = \frac{\alpha_H \lambda g_0}{4\pi} \frac{\frac{I_R}{I_{sat}}}{1 + \frac{I_R}{I_{sat}}} \tag{6.23}$$

Equations 6.2 through 6.6 form a system of non-linear equations that needs to be solved numerically for a given input optical intensity (I_{in}), disk parameters (κ, φ_0, Γ), material parameters (α_H, g_0) and wavelength (λ). Once the solution for intensity in the disk, round-trip gain and phase is obtained, the output power can be calculated from eqn. 6.1. This was implemented in a MATLAB script (software supplement C) and the various parameters such as intensity in disk, output intensity, phase-change and round-trip gain plotted as a function of the input intensity.

Figure 6.19 shows the results from such a calculation. The various parameters used in the calculation are indicated in table 6.1.

Parameter	Value
Wavelength (λ)	1550 nm
Disk radius (R)	20 μm
Coupling coefficient (κ)	0.6
Loss in ring	15 cm^{-1}
Linewidth enhancement factor (α_H)	3
Unsaturated gain (g_0)	1000 cm^{-1}
Overlap factor (Γ)	0.05
Initial detuning from resonance (φ_0)	-0.2 rad

Table 6.1: Parameters used in the simulation of optical non-linearity and bistability shown in figure 6.19.

All the intensities in the graphs in figure 6.19 are normalized to the saturation intensity (I_{sat}), estimated at about 64 KW/cm^2 using the values in table 2.1. Figure 6.19a shows the

intensity in the ring as a function of the input intensity. Figure 6.19b show the round-trip gain (a) as a function of the input intensity. The lasing threshold is indicated by a dashed line. Figure 6.19c shows the round-trip phase. It indicates the relative position of the resonance w.r.t. the input wavelength. They are coincident when $\varphi = 0$ (indicated by a dashed line). The movement of the resonance is seen to corroborate the physical process described earlier in this section. The last figure (6.19d) shows the output intensity as a function of the input. The non-linear transfer characteristics as well as the counter-clockwise hysteresis / bistable operation are seen to qualitatively match the experimental results shown in figure 6.16. The blue curves denote the path taken when the input intensity is increasing and the red curve denotes the path taken on the way down as indicated by the arrows.

The simulation was repeated with lower gain. The parameters used are indicated in table 6.2. Figure 6.20 shows the plot of the various parameters as a function of input intensity for the case of lower gain. As before, figure 6.20a shows the intensity in the disk. The bistable operation and direction have not changed from before. Figure 6.20b shows the round-trip gain as a function of the input intensity. Notice how the gain drops from above unity to below indicating net loss in the round-trip. Figure 6.20c and 6.20d show the round-trip phase and transmitted intensity respectively. The transmitted intensity is seen to drop with increasing input intensity beyond a threshold due to a corresponding drop in the round-trip gain. Also, the direction of bistability is seen to change to clockwise as was observed in the experiment (fig. 6.18).

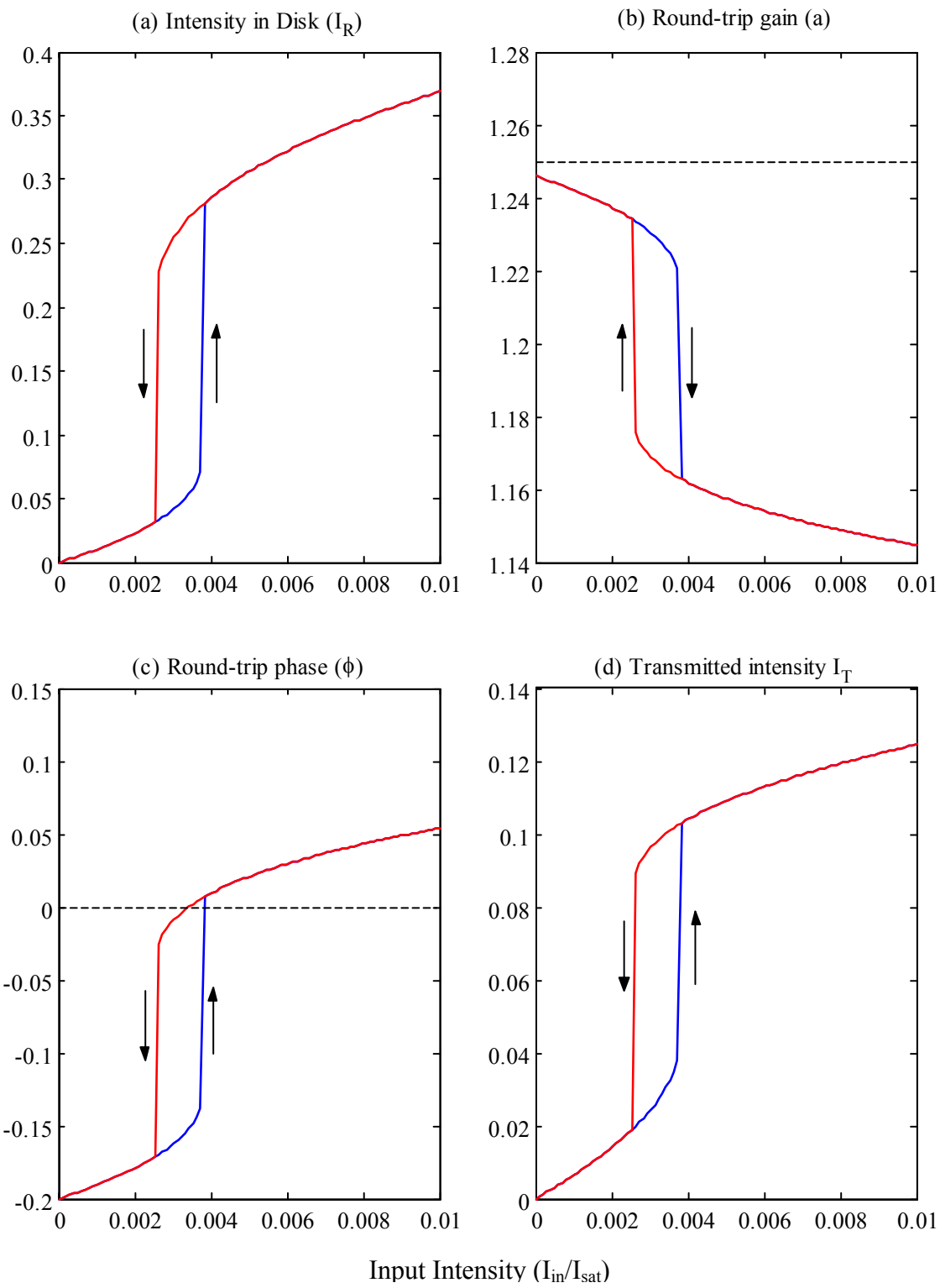

Figure 6.19: Simulated non-linear response in a microdisk using parameters from table 6.1. All intensities are normalized w.r.t to the saturation intensity (I_{sat}). (a) Intensity in disk/ring (b) Round-trip gain (c) Round-trip phase (d) Transmitted intensity.

Parameter	Value
Wavelength (λ)	1550 nm
Disk radius (R)	20 μm
Coupling coefficient (κ)	0.4
Loss in ring	15 cm^{-1}
Linewidth enhancement factor (α_H)	3
Unsaturated gain (g_0)	550 cm^{-1}
Overlap factor (Γ)	0.05
Initial detuning from resonance (φ_0)	-0.3 rad

Table 6.2: Parameters used in the simulation of optical non-linearity and bistability shown in figure 6.20.

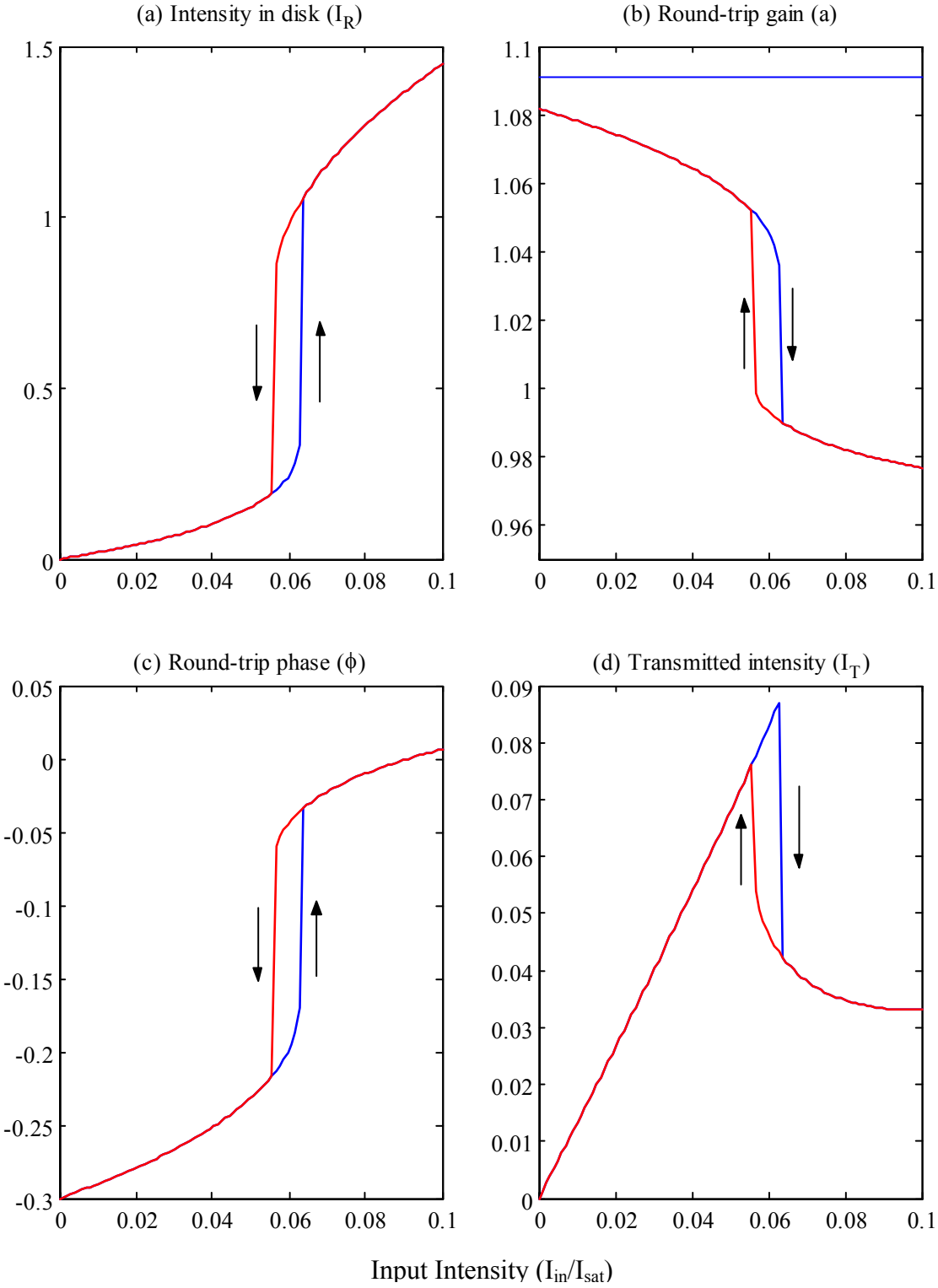

Figure 6.20: Simulated non-linear response in a microdisk using parameters from table 6.2. All intensities are normalized w.r.t. the saturation intensity (I_{sat}). (a) Intensity in disk/ring (b) Round-trip gain (c) Round-trip phase (d) Transmitted intensity

6.8 All-Optical Switching in Pseudo / Microdisks

In this section, I will describe the experiment to switch one beam of light using another by means of the non-linear response in a microdisk resonator. The essential idea is to make use of the rapid shift of resonances with optical intensity to modulate a probe beam tuned close to one of the resonances. The scheme is illustrated in figure 6.21. The microdisk resonator is biased into the gain region. A pump-beam is tuned close one of the resonances, resonance A in the figure, and is slightly red-shifted. A low power probe-beam is tuned to another resonance, resonance B in the figure, and is aligned precisely with the peak of the resonance. When the pump beam is off, the low power probe-beam undergoes amplification in the disk and emerges at the output. However, when the higher-power pump-beam is turned on, the resonances undergo a shift to the longer wavelengths (red-shift) as described in the previous section due to the gain saturation non-linearity. As a result, the probe-beam is no longer aligned with the peak of the resonance. Instead, it lies near the foot of the resonance and hence is not amplified through the disk anymore. Consequently, the probe intensity drops at the output. When the pump intensity is switched off or reduced, the resonances shift back and the probe appears at the output again. The bistability of the switching operation results in a Schmitt trigger like response for the NOT gate.

Figure 6.22 shows the experimental setup used. It is similar to that used in the previous section and shown in figure 6.14. The pump signal is a 4 MHz sinusoidal or triangular wave generated by modulating a tunable laser. The wavelength is tuned to align with one of the resonances (1541.95 nm) but red-shifted slightly (1542.12 nm). The probe signal is a CW beam from another tunable laser and is tuned to the next resonance

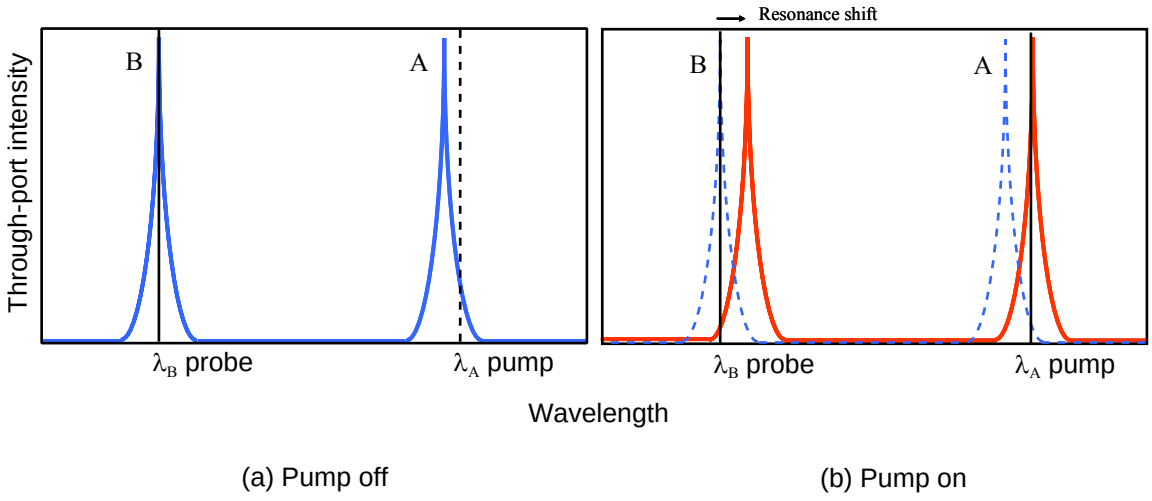

Figure 6.21: Schematic illustrating the pump-probe switch mechanism. (a) Resonance location when the pump beam is off. Probe is tuned to resonance B (b) Resonance shifts to longer wavelengths when the pump is turned on. Probe is no longer aligned with resonance B.

(~1536.11 nm). The microdisk resonator was biased at 20 mA and the bus at 35 mA. The heat sink temperature was maintained at about 2 °C during the experiment. The pump power at the output of the optical amplifier was 5 mW. The probe beam power was 1 mW at the output of the tunable laser. The pump and probe beams are mixed through a coupler and fed to the device under test. A small fraction of the input beam is tapped off to monitor and record on an oscilloscope. The output is collected through a lensed fiber and a fraction (50 %) fed to a photodetector for monitoring the pump waveform. The other fraction passes through a band-pass filter to extract the probe and amplified through an optical amplifier before being measured at a photodetector.

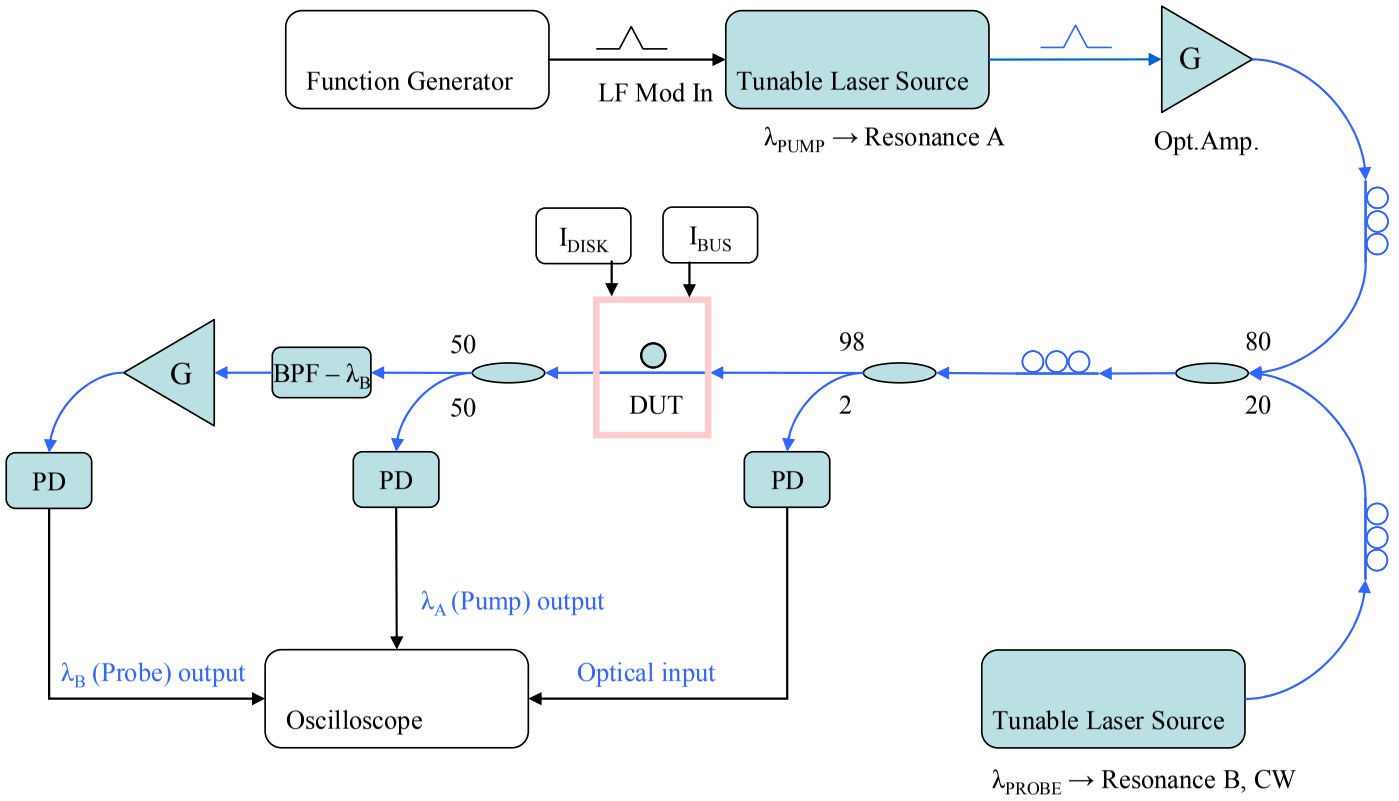

Figure 6.22: Schematic of the pump-probe experiment to demonstrate all-optical switching in active pseudo / microdisk resonators. Optical paths are shown in blue and electrical paths in black.

Figure 6.23 shows the results from the experiment. It is a plot of waveforms for the input pump, output pump and the output probe signals respectively from top to bottom. All powers have been normalized by eliminating the baseline due to amplified spontaneous emission (ASE) from the optical amplifiers by subtracting the DC component and then scaling the range from zero to one. Dotted lines have been added as a guide to the eye to correlate switching transitions between the waveforms. The probe output can be seen to exhibit NOT gate behavior with the pump as the input. Figure 6.24 plots the normalized probe output power as a function of the pump input power. The NOT gate response can be seen to show hysteresis behavior as in a Schmitt gate. The arrows indicate the direction of switching.

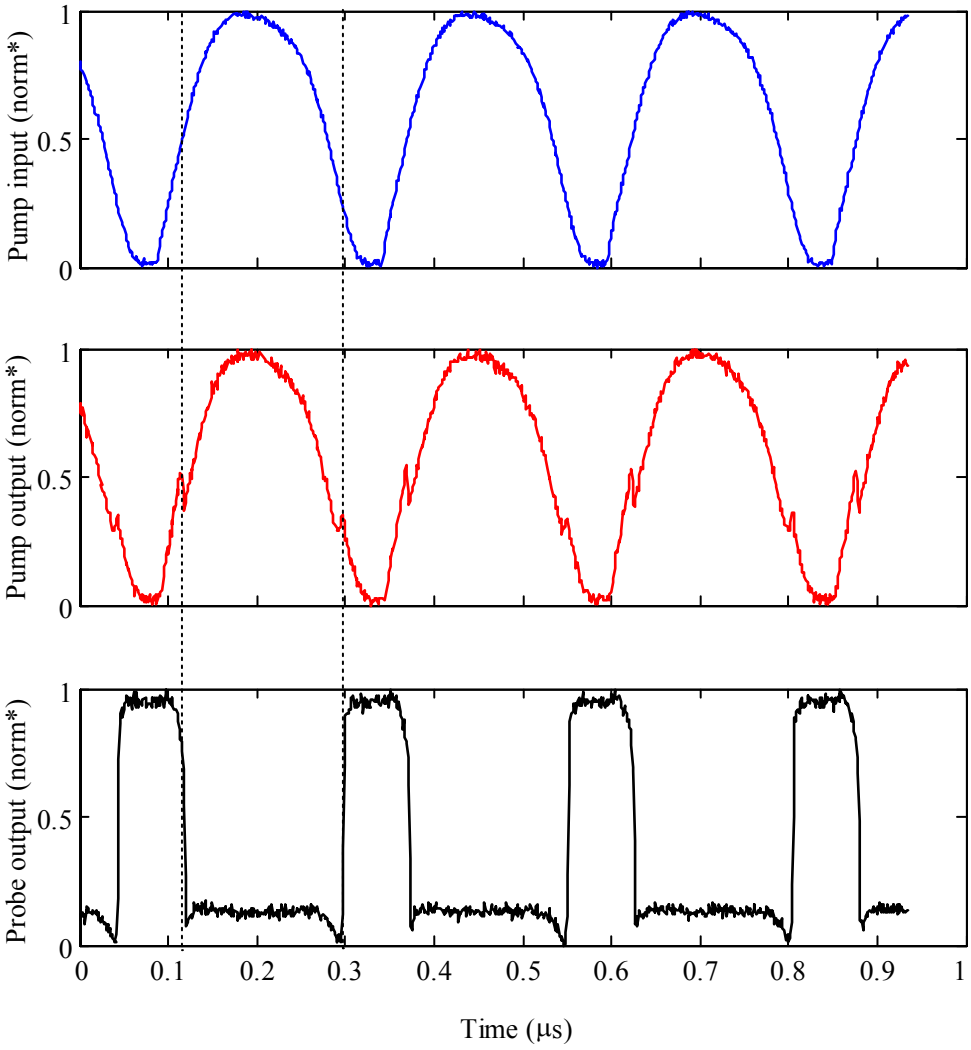

Figure 6.23: Waveforms from the pump-probe experiment showing NOT gate operation in a 20 um radius microdisk. The upper most waveform is the pump input. The middle waveform is the pump at the output. The lower most waveform is the probe beam at the output.

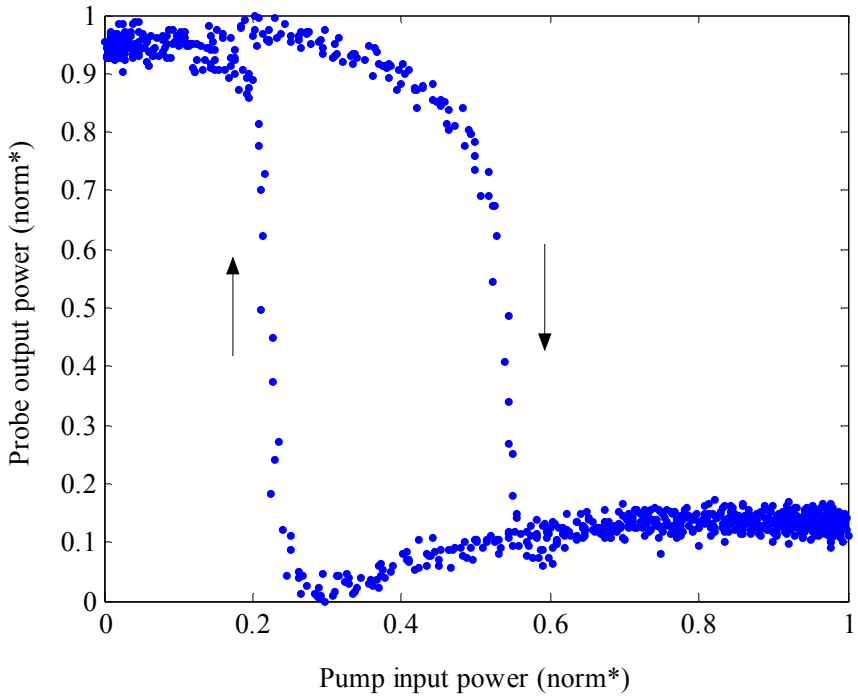

Figure 6.24: Probe output intensity plotted as a function of the pump input intensity using the same data as in figure 6.23 showing NOT gate behavior with a Schmitt trigger type of hysteresis.

Chapter 7

CONCLUSION

The goal of this research was to develop a microring or microdisk based all-optical switch that could operate at low optical intensities and be cascaded easily to form small optical circuits. The gain saturation mechanism in electrically pumped quantum wells was identified as the best means to achieve this. The demonstrated devices were seen to switch at optical powers of a few milliwatts, more than two orders of magnitude lower than that in passive microrings. A novel laterally coupled pseudodisk architecture that made use of negative gap coupling was developed, which eased fabrication requirements considerably as well as combined the best of microdisks and microrings in one device. The design combined the superior heat-sinking and lower surface recombination capabilities of the microdisk with the single mode operation capability of the microring. To the best of my knowledge, this is the first demonstration of all-optical switching on the active microdisk platform.

Also, an optical amplifier based on active microrings was demonstrated, whose properties could be adjusted by controlling the current through the device. Up to 10 dB of gain in pulsed mode was seen for these devices. The response of the amplifier could be changed from under-coupled to critically coupled to transparency to gain and finally lasing by varying the current. These amplifiers can be used for providing inter-gate or inter-switch optical amplification to compensate for any insertion losses as well as

convert probe beams to pump beams between stages.

The control of surface recombination was identified as being critical to device performance. A large fraction of injected carriers (> 30 %) are lost to surface recombination on the sidewalls of the rings. A sulfur based passivation scheme was developed that resulted in the surface recombination velocity dropping nearly an order of magnitude.

Two critical factors: power consumption and speed are expected to play a significant role in determining the performance and applications for these devices. While optical power has been reduced by a large margin, the electrical power consumed by these devices can be reduced further. Typically device currents are 15 mA at 2 V of forward bias. Thus the scale of integration of these devices will be limited by the power budget and heat sinking capabilities. The power consumption can be greatly reduced by reducing scattering losses and using slightly higher Q-factor designs for microdisks. Microdisk lasers with sub-milliampere currents have been demonstrated elsewhere [114], so this seems quite feasible.

Speed in these devices is determined by the slowest of three different processes. They are stimulated recombination efficiency, photon lifetime in cavity and carrier transport in the microdisks. The last of these processes is expected to be the limiting factor. Carriers that recombine by stimulated emission in the gain saturation process along the edge of the disk need to be replenished once the light input is turned off. The replenishment occurs by carriers diffusing from the central reservoir to the periphery. Diffusion is much slower compared to drift and hence this might be a limiting factor ultimately.

Appendix A

PROCESS RECIPES

A.1 Lithography

A.1.1 Positive resist – OiR 906-10 (Olin).

Spin on HMDS (hexamethyldisilazane) adhesion promoter at 3000 rpm, 60 s. Spin on Oir 906-10 at 3000 rpm, 60 s. Pre-bake at 90 °C for 60 s on hot-plate. Expose on projection aligner (GCA 5x). Post-bake at 120 °C for 60 s on hot-plate. Develop in OPD 4262 developer for 60 s. Rinse in DI water for 30s.

A.1.2 Positive resist – OiR 908-35 (Olin).

Spin on HMDS (hexamethyldisilazane) adhesion promoter at 3000 rpm, 60 s. Spin on Oir 908-35 at 4000 rpm, 60 s. Pre-bake at 90 °C for 60 s on hot-plate. Expose on projection aligner (GCA 5x). Post-bake at 105 °C for 60 s in furnace. Develop in OPD 4262 developer for 60 s. Rinse in DI water for 30 s.

A.1.3 Negative resist – NR7-1500PY (Shipley) for lift-off.

Spin on NR7-1500PY at 3000 rpm. Pre-bake at 120 °C for 60 s on hot-plate. Expose on projection aligner (GCA 5x). Post-bake at 120 °C for 60 s on hot-plate. Develop in RD6 developer for 8 s. Rinse in DI water for 30 s.

A.1.4 Negative resist – NR7-1500P (Shipley) for dry-etch.

Spin on NR7-1500P at 3000 rpm. Pre-bake at 120 °C for 60 s on hot-plate. Expose on projection aligner (GCA 5x). Post-bake at 120 °C for 60 s on hot-plate. Develop in RD6 developer for 8 s. Rinse in DI water for 30 s.

A.2 Plasma Deposition (HDPECVD)

Oxford Plasmalab 100 HDPECVD.

A.2.1 Silicon dioxide.

3 min temperature stabilization at 120 °C. Adhesion enhancement: 20 sccm NH_3 at 15 mTorr, 150 W RF power, 0 W ICP power, 1 min. Silicon dioxide: 20 sccm N_2O + 4 sccm SiH_4 at 1 mTorr (2 mTorr actual). 4 W RF power, 500 W ICP power. Deposition rate ~ 300 Å/min.

A.2.2 Silicon nitride – passivation cap

3 min temperature stabilization at 120 °C. Adhesion enhancement: 20 sccm NH_3 at 15 mTorr, 150 W RF power, 0 W ICP power, 1 min. Silicon nitride: 10 sccm SiH_4 + 17 sccm N_2 at 10 mTorr. 4 W RF power, 500 W ICP power for 1 min. Approximate thickness ~ 200 Å.

A.2.3 Silicon nitride – heat sink layer

5 min temperature stabilization at 300 °C. Adhesion enhancement: 20 sccm NH_3 at 15 mTorr, 150 W RF power, 0 W ICP power for 5 min. Silicon nitride: 9 sccm SiH_4 + 18 sccm N_2 at 10 mTorr. 4 W RF power, 500 W ICP power for 30 to 60 min.

A.3 Reactive Ion Etching (RIE)

Plasmatherm 790 series RIE.

A.3.1 Silicon dioxide etch

18 sccm CHF_3 + 2 sccm O_2 at 40 mTorr. 175 W RF power. Etch rate ~ 300 Å/min.

A.3.2 BCB etch back

5 sccm CHF_3 + 19 sccm O_2 at 300 mTorr. 175 W RF power. Etch rate ~ 6000 Å/min.

A.3.3 Indium phosphide etch

Two stage etch. Stage 1: 8 sccm CH_4 + 32 sccm H_2 + 10 sccm Ar at 30 mTorr. 440 V DC self-bias. 5 minutes. Stage 2: 16 sccm O_2 at 200 mTorr. 200 V DC self-bias. 3 minutes. Anodized aluminum plate electrode. Etch rate ~ 500 Å/min.

A.3.4 Oxygen descum for removing photoresist.

19 sccm O_2 at 200 mTorr. 25 W RF power. 15 seconds.

A.4 E-beam Evaporator / Metallization

CHA Inc. Mark-40 e-beam evaporator.

A.4.1 P-contact

20 s dip in 5% H_2SO_4 for oxide removal. 100 Å titanium, 300 Å platinum, 3000 Å gold in e-beam evaporator.

A.4.2 N-contact

20 s dip in 5% H_2SO_4 for oxide removal. 50 Å nickel, 400 Å germanium, 800 Å gold, 300 Å nickel, 3000 Å gold in e-beam evaporator.

A.5 Wet processes

A.5.1 Native oxide removal

5% H_2SO_4 for 20 s followed by 30 s rinse in DI water.

A.5.2 Indium phosphide selective etch

1:1 of HCl and H_3PO_4 at room temperature. Selectively etches InP over InGaAs.

A.5.3 Indium gallium arsenide selective etch

1:1:8 of H_2SO_4, H_2O_2 and H_2O at room temperature. Selectively etches InGaAs over InP.

A.5.4 Silicon dioxide etch

Buffered hydrofluoric acid (1:7 of HF and NH_4F). Selectively etches silicon dioxide and nitride over III-V compounds.

A.6 Rapid thermal annealing

AG Associates HeatPulse.

A.6.1 N-contact alloying

Ramp from RT to 300 °C at 10 °C/s. Stay at 300 °C for 60 s. Ramp from 300 °C to 400 °C at 10 °C/s. Stay at 400 °C for 40 s. Natural cool down. Forming gas (H_2+N_2)

ambient.

A.7 BCB planarization

Spin on AP-3000 (Dow Chemical) adhesion promoter at 3000 rpm for 60 s. Spin on BCB-57 at 4000 rpm for 60 s. Pre-bake on hot-plate at 120 C for 2 minutes. Cure in tube furnace in N_2 ambient. Ramp to 250 °C from room temperature over 60 min, stay at 250 °C for 2 hrs, natural cool-down.

A.8 Mechanical Lapping

Logitech PM2A polisher.

Wafer mounted on polishing chuck (Southbay Technology) using wax (Crystal Bond 509). Cast iron polishing plate. Slurry: 1:6 (v/v) 9 μm alumina in water. Feed rate ~ 1-2 drops /s. Oscillation rate ~ 12-15 osc / min. Lapping rate ~ 10-15 μm / min.

BIBLIOGRAPHY

[1] M. Matsuhara and A. Watanabe, "Coupling of curved transmission lines, and application to optical directional couplers," *Journal of the Optical Society of America*, vol. 65, pp. 163-8, 1975.

[2] K. Nakatsuhara, T. Mizumoto, R. Munakata, Y. Kigure, and Y. Naito, "All-optical set-reset operation in a distributed feedback GaInAsP waveguide," *IEEE Photonics Technology Letters*, vol. 10, pp. 78-80, 1998.

[3] B. R. Bennett, R. A. Soref, and J. A. Del Alamo, "Carrier-induced change in refractive index of InP, GaAs and InGaAsP," *IEEE Journal of Quantum Electronics*, vol. 26, pp. 113-22, 1990.

[4] D. Marshall, A. Miller, and C. C. Button, "In-well ambipolar diffusion in room-temperature InGaAsP multiple quantum wells," *IEEE Journal of Quantum Electronics*, vol. 36, pp. 1013-15, 2000.

[5] G. P. Agrawal and N. K. Dutta, "Semiconductor Lasers," 1993.

[6] C. J. Sandroff, R. N. Nottenburg, J. C. Bischoff, and R. Bhat, "Dramatic enhancement in the gain of a GaAs/AlGaAs heterostructure bipolar transistor by surface chemical passivation," *Applied Physics Letters*, vol. 51, pp. 33-5, 1987.

[7] H. K. Tsang, R. V. Penty, I. H. White, R. S. Grant, W. Sibbett, J. B. D. Soole, H. P. LeBlanc, N. C. Andreadakis, R. Bhat, and M. A. Koza, "Two-photon absorption and self-phase modulation in InGaAsP/InP multi-quantum-well waveguides," *Journal of Applied Physics*, vol. 70, pp. 3992-4, 1991.

[8] P. M. Paul, E. S. Toma, P. Breger, G. Mullot, F. Auge, P. Balcou, H. G. Muller, and P. Agostini, "Observation of a train of attosecond pulses from high harmonic generation," *Science*, vol. 292, pp. 1689-92, 2001.

[9] W. Hafez and M. Feng, "Experimental demonstration of pseudomorphic heterojunction bipolar transistors with cutoff frequencies above 600 GHz," *Appl. Phys. Lett.*, vol. 86, pp. 152101, 2005.

[10] E. A. J. Marcatili, "Bends in optical dielectric guides," *Bell System Technical Journal*, vol. 48, pp. 2103-32, 1969.

[11] S. T. Chu, B. E. Little, W. Pan, and Y. Kokubun, "A cross-grid array of microresonators for very large scale integrated photonic circuits," presented at Conference on Lasers and Electro-Optics, San Francisco, CA, 1999.

[12] B. E. Little and S. T. Chu, "Microring resonators for very large scale integrated photonics," presented at IEEE Lasers and Electro-Optics Society, 12th Annual Meeting, Baltimore, MD, 1999.

[13] B. E. Little and S. T. Chu, "The application of microresonators in large scale

optical signal processing circuits," *Laser Resonators III*, 2000.
[14] B. E. Little, S. T. Chu, and H. A. Haus, "Micro-ring resonator channel dropping filters," presented at IEEE Lasers and Electro-Optics Society, 8th Annual Meeting, 1995.
[15] S. T. Chu, B. E. Little, W. Pan, T. Kaneko, S. Sato, and Y. Kokubun, "An eight-channel add-drop filter using vertically coupled microring resonators over a cross grid," *IEEE Photonics Technology Letters*, vol. 11, pp. 691-693, 1999.
[16] S. J. Choi, P. Zhen, Y. Qi, C. Sang Jun, and P. D. Dapkus, "8-channel tunable MUX/DEMUX using vertically coupled active microdisk resonators," *2003 IEEE LEOS Annual Meeting Conference Proceedings (IEEE Cat. No.03CH37460)*, 2003.
[17] R. Orta, P. Savi, R. Tascone, and D. Trinchero, "Synthesis of multiple-ring-resonator filters for optical systems," *IEEE Photonics Technology Letters*, vol. 7, pp. 1447-1449, 1995.
[18] S. T. Chu, B. E. Little, W. Pan, T. Kaneko, and Y. Kokubun, "Second order filter response from parallel coupled glass microring resonators," *IEEE Photonics Technology Letters*, vol. 11, pp. 1426-1428, 1999.
[19] B. E. Little, S. T. Chu, J. V. Hryniewicz, and P. P. Absil, "Filter synthesis for periodically coupled microring resonators," *Optics Letters*, vol. 25, pp. 344-346, 2000.
[20] R. Grover, V. Van, T. A. Ibrahim, P. P. Absil, L. C. Calhoun, F. G. Johnson, J. V. Hryniewicz, and P.-T. Ho, "Parallel-cascaded semiconductor microring resonators for high-order and wide-FSR filters," *Journal of Lightwave Technology*, vol. 20, pp. 900-905, 2002.
[21] B. E. Little, S. T. Chu, P. P. Absil, J. V. Hryniewicz, F. G. Johnson, F. Seiferth, D. Gill, V. Van, O. King, and M. Trakalo, "Very high-order microring resonator filters for WDM applications," *IEEE Photonics Technology Letters*, vol. 16, pp. 2263-5, 2004.
[22] P. P. Absil, J. V. Hryniewicz, B. E. Little, F. G. Johnson, and P. T. Ho, "Wavelength selective mirror using notched microring resonators," *LEOS 2001. 14th Annual Meeting of the IEEE Lasers and Electro-Optics Society (Cat. No.01CH37242)*, 2001.
[23] J. K. S. Poon, J. Scheuer, and A. Yariv, "Wavelength-selective reflector based on a circular array of coupled microring resonators," *IEEE Photonics Technology Letters*, vol. 16, pp. 1331-3, 2004.
[24] G. T. Paloczi, J. Scheuer, and A. Yariv, "Compact microring-based wavelength-selective inline optical reflector," *IEEE Photonics Technology Letters*, vol. 17, pp. 390-2, 2005.
[25] S. L. McCall, A. F. J. Levi, R. E. Slusher, S. J. Pearton, and R. A. Logan, "Whispering-gallery mode microdisk lasers," *Applied Physics Letters*, vol. 60, pp. 289-91, 1992.
[26] S. M. K. Thiyagarajan, D. A. Cohen, A. F. J. Levi, S. Ryu, R. Li, and P. D. Dapkus, "Continuous room-temperature operation of microdisk laser diodes," *Electronics Letters*, vol. 35, pp. 1252-4, 1999.
[27] C. Seung June, P. Zhen, Y. Qi, C. Sang Jun, and P. D. Dapkus, "Eight-channel microdisk CW laser arrays vertically coupled to common output bus waveguides,"

IEEE Photonics Technology Letters, vol. 16, pp. 356-8, 2004.

[28] K. Djordjev, C. Seung-June, C. Sang-Jun, and P. D. Dapkus, "Vertically coupled InP microdisk switching devices with electroabsorptive active regions," *IEEE Photonics Technology Letters*, vol. 14, pp. 1115-17, 2002.

[29] P. Rabiei, W. H. Steier, Z. Cheng, W. Chuan-guang, and H. J. Lee, "Polymer micro-ring modulator with 1 THz FSR," *Postdeadline Papers. Summaries of papers presented at the Conference on Lasers and Electro-Optics. Conference Edition (IEEE Cat. No.02CH37337)*, 2002.

[30] S. Pradhan, B. Schmidt, L. Martinez, Q. Xu, V. R. Almeida, C. Barrios, and M. Lipson, "Electro-optic modulator on silicon-on-insulator substrates using ring resonators," *2005 Conference on Lasers and Electro-Optics (CLEO) (IEEE Cat. No. 05TH8796)*, 2005.

[31] R. G. Walker and C. D. W. Wilkinson, "Integrated optical ring resonators made by silver ion-exchange in glass," *Applied Optics*, vol. 22, pp. 1029-1035, 1983.

[32] B. E. Little, S. T. Chu, W. Pan, D. Ripin, T. Kaneko, Y. Kokubun, and E. P. Ippen, "Vertically coupled glass microring resonator channel dropping filters," *IEEE Photonics Technology Letters*, vol. 11, pp. 215-217, 1999.

[33] M. Kuwata-Gonokami, A. Dodabalapur, R. H. Jordan, H. E. Katz, M. L. Schilling, R. E. Slusher, and S. Ozawa, "Polymer microdisk and microcylinder lasers," presented at Quantum Electronics and Laser Science, Baltimore, MD, 1995.

[34] P. Rabiei, W. H. Steier, C. Zhang, and L. R. Dalton, "Polymer micro-ring filters and modulators," *Journal of Lightwave Technology*, vol. 20, pp. 1968-1975, 2002.

[35] J. Bismuth, P. Gidon, F. Revol, and S. Valette, "Low-loss ring resonators fabricated from silicon based integrated optics technologies," *Electronics Letters*, vol. 27, pp. 722-724, 1991.

[36] A. Tate, M. Yanagisawa, Y. Ohmori, T. Miya, and M. Kobayashi, "GaAs/AlGaAs guided-wave optical ring resonator," *Proceedings of the SPIE - The International Society for Optical Engineering*, vol. 1177, pp. 162-8, 1990.

[37] R. Grover, P. P. Absil, V. Van, J. V. Hryniewicz, B. E. Little, O. S. King, F. G. Johnson, L. C. Calhoun, and P.-T. Ho, "Vertically coupled GaAs-AlGaAs and GaInAsP-InP microring resonators," presented at Optical Fiber Communication, Anaheim, CA, 2001.

[38] T. A. Ibrahim, V. Van, K. Ritter, P. P. Absil, F. G. Johnson, R. Grover, J. Goldhar, and P. T. Ho, "Fast nonlinear all-optical switching in a compact semiconductor microring resonator," *LEOS 2001. 14th Annual Meeting of the IEEE Lasers and Electro-Optics Society (Cat. No.01CH37242)*, 2001.

[39] T. A. Ibrahim, W. Cao, Y. Kim, J. Li, J. Goldhar, P. T. Ho, and C. H. Lee, "Lightwave switching in semiconductor microring devices by free carrier injection," *Journal of Lightwave Technology*, vol. 21, pp. 2997-3003, 2003.

[40] V. Van, T. A. Ibrahim, P. P. Absil, F. G. Johnson, R. Grover, and P. T. Ho, "Optical signal processing using nonlinear semiconductor microring resonators," *IEEE Journal of Selected Topics in Quantum Electronics*, vol. 8, pp. 705-13, 2002.

[41] T. A. Ibrahim, L. C. Kuo, K. Amarnath, R. Grover, V. Van, and P. T. Ho, "Photonic logic NOR gate using two symmetric microring resonators,"

Conference on Lasers and Electro-Optics (CLEO), 2004.
[42] F. Zernike, E. L. Sloan, J. C. Webster, R. W. Bialack, and W. L. Knecht, "Coupling between optical waveguides," *1972 Annual Meeting of the Optical Society of America. Abstracts only*, pp. 19,88, 1972.
[43] K. Okamoto, *Fundamentals of Optical Waveguides*, 1st ed: Academic Press, 2000.
[44] H. Haus, *Waves and Fields in Optoelectronics*: Prentice-Hall, 1983.
[45] V. Van, P. P. Absil, J. V. Hryniewicz, and P. T. Ho, "Propagation loss in single-mode GaAs-AlGaAs microring resonators: measurement and model," *Journal of Lightwave Technology*, vol. 19, pp. 1734-9, 2001.
[46] M. Heiblum and J. H. Harris, "Analysis of curved optical waveguides by conformal transformation," *IEEE Journal of Quantum Electronics*, vol. QE-11, pp. 75-83, 1975.
[47] W. Berglund and A. Gopinath, "WKB analysis of bend losses in optical waveguides," *Journal of Lightwave Technology*, vol. 18, pp. 1161-6, 2000.
[48] D. Marcuse, "Bend loss of slab and fiber modes computed with diffraction theory," *IEEE Journal of Quantum Electronics*, vol. 29, pp. 2957-61, 1993.
[49] P. K. Tien, "Light waves in thin films and integrated optics," *Applied Optics*, vol. 10, pp. 2395-13, 1971.
[50] J. P. R. Lacey and F. P. Payne, "Radiation loss from planar waveguides with random wall imperfections," *IEE Proceedings J (Optoelectronics)*, vol. 137, pp. 282-8, 1990.
[51] D. Marcuse, "Mode conversion caused by surface imperfections of a dielectric slab waveguide," *Bell System Technical Journal*, vol. 48, pp. 3187-215, 1969.
[52] W. P. Dumke, M. R. Lorenz, and G. D. Pettit, "Intra- and interband free-carrier absorption and the fundamental absorption edge in n-type InP," *Physical Review B (Solid State)*, vol. 1, pp. 4668-73, 1970.
[53] L. Xu, D. Garbuzov, S. Forrest, R. Menna, R. Martinelli, and J. Connolly, "Very low internal loss, 1.5 μm wavelength SCH-MQW InGaAsP/InP laser diodes with broadened-waveguides," *Conference Proceedings. LEOS '96 9th Annual Meeting. IEEE Lasers and Electro-Optics Society 1996 Annual Meeting (Cat. No.96CH35895)*, 1996.
[54] M. Bugajski and W. Lewandowski, "Concentration-dependent absorption and photoluminescence of n-type InP," *Journal of Applied Physics*, vol. 57, pp. 521-30, 1985.
[55] J. S. Foresi, B. E. Little, G. Steinmeyer, E. Thoen, S. T. Chu, H. A. Haus, E. P. Ippen, L. C. Kimerling, and W. Greene, "Si/SiO$_2$ micro-ring resonator optical add/drop filters," presented at Conference on Lasers and Electro-Optics, Baltimore, MD, 1997.
[56] D. Rafizadeh, J. P. Zhang, S. C. Hagness, A. Taflove, K. A. Stair, S. T. Ho, and R. C. Tiberio, "Waveguide-coupled AlGaAs/GaAs microcavity ring and disk resonators with high finesse and 21.6-nm free spectral range," *Optics Letters*, vol. 22, pp. 1244-6, 1997.
[57] M. K. Chin and S. T. Ho, "Design and modeling of waveguide-coupled single-mode microring resonators," *Journal of Lightwave Technology*, vol. 16, pp. 1433-46, 1998.

[58] R. Grover, P. P. Absil, V. Van, J. V. Hryniewicz, B. E. Little, O. S. King, L. C. Calhoun, F. G. Johnson, and P.-T. Ho, "Vertically coupled GaInAsP-InP microring resonators," *Optics Letters*, vol. 26, pp. 506-508, 2001.
[59] R. W. Boyd, *Nonlinear Optics*: Academic Press, 1992.
[60] M. Bass, P. A. Franken, J. F. Ward, and G. Weinreich, "Optical Rectification," *Phys. Rev. Lett.*, vol. 9, pp. 446–448, 1962.
[61] P. A. Franken, A. E. Hill, C. W. Peters, and G. Weinreich, "Generation of Optical Harmonics," *Phys. Rev. Lett.*, vol. 7, pp. 118–119, 1961.
[62] J. A. Giordmaine and R. C. Miller, "Optical Parametric Oscillation in the Visible Spectrum," *Appl. Phys. Lett.*, vol. 9, pp. 298, 1966.
[63] W. Kaiser and C. G. B. Garrett, "Two-Photon Excitation in CaF2: Eu2+," *Phys. Rev. Lett.*, vol. 7, pp. 229-231, 1961.
[64] J. H. Bechtel and W. L. Smith, "Two-photon absorption in semiconductors with picosecond laser pulses," *Physical Review B (Solid State)*, vol. 13, pp. 3515-22, 1976.
[65] F. R. Laughton, J. H. Marsh, and A. H. Kean, "Very sensitive two-photon absorption GaAs/AlGaAs waveguide detector for an autocorrelator," *Electronics Letters*, vol. 28, pp. 1663-5, 1992.
[66] V. Van, T. A. Ibrahim, K. Ritter, P. P. Absil, F. G. Johnson, R. Grover, J. Goldhar, and P. T. Ho, "All-optical nonlinear switching in GaAs-AlGaAs microring resonators," *IEEE Photonics Technology Letters*, vol. 14, pp. 74-6, 2002.
[67] C. H. Henry, "Theory of the linewidth of semiconductor lasers," *IEEE Journal of Quantum Electronics*, vol. QE-18, pp. 259-64, 1982.
[68] C. Harder, K. Vahala, and A. Yariv, "Measurement of the linewidth enhancement factor α of semiconductor lasers," *Applied Physics Letters*, vol. 42, pp. 328-30, 1983.
[69] C. A. Green, N. K. Dutta, and W. Watson, "Linewidth enhancement factor in InGaAsP/InP multiple quantum well lasers," *Applied Physics Letters*, vol. 50, pp. 1409-10, 1987.
[70] N. Ogasawara, R. Ito, and R. Morita, "Linewidth enhancement factor in GaAs/AlGaAs multi-quantum-well lasers," *Japanese Journal of Applied Physics, Part 2 (Letters)*, vol. 24, pp. L519-21, 1985.
[71] M. G. Burt, "Linewidth enhancement factor for quantum-well lasers," *Electronics Letters*, vol. 20, pp. 27-9, 1984.
[72] T. A. Ibrahim, "Nonlinear Optical Semiconductor Micro-Ring Resonators," in *Electrical and Computer Engineering*, vol. PhD. College Park: University of Maryland, 2003.
[73] Optical Waveguide Mode Solver (OWMS), 1.21, Apollo Photonics Inc., www.apollophotonics.com
[74] W. W. Lui, T. Hirono, K. Yokoyama, and H. Wei-Ping, "Polarization rotation in semiconductor bending waveguides: a coupled-mode theory formulation," *Journal of Lightwave Technology*, vol. 16, pp. 929-36, 1998.
[75] MATLAB, 6.5, MathWorks Inc., www.mathworks.com
[76] E. Kuphal, "Phase diagrams of InGaAsP, InGaAs and InP lattice-matched to (100)InP," *Journal of Crystal Growth*, vol. 67, pp. 441-57, 1984.

[77] R. Grover, J. V. Hryniewicz, O. S. Oliver Simon King, and V. Vien, "Process development of methane-hydrogen-argon-based deep dry etching of InP for high aspect-ratio structures with vertical facet-quality sidewalls," *Journal of Vacuum Science & Technology B (Microelectronics and Nanometer Structures)*, vol. 19, pp. 1694-8, 2001.

[78] C. Seung June, K. Djordjev, C. Sang Jun, and P. D. Dapkus, "CH/sub 4/-based dry etching of high Q InP microdisks," *Journal of Vacuum Science & Technology B (Microelectronics and Nanometer Structures)*, vol. 20, pp. 301-5, 2002.

[79] F. Niklaus, P. Enoksson, E. Kalvesten, and G. Stemme, "Low-temperature full wafer adhesive bonding," *Journal of Micromechanics and Microengineering*, vol. 11, pp. 100-7, 2001.

[80] F. Niklaus, H. Andersson, P. Enoksson, and G. Stemme, "Low temperature full wafer adhesive bonding of structured wafers," *Sensors and Actuators A (Physical)*, vol. A92, pp. 235-41, 2001.

[81] P. P. Absil, J. V. Hryniewicz, B. E. Little, F. G. Johnson, and P.-T. Ho, "Vertically coupled microring resonators using polymer wafer bonding," *IEEE Photonics Technology Letters*, vol. 13, pp. 49-51, 2001.

[82] Dow, "Processing Procedures for CYCLOTENE 3000 Series Dry Etch Resins," Dow Chemical Inc. 2005.

[83] V. N. Bessolov, E. V. Konenkova, and M. V. Lebedev, "A comparison of the effectiveness of GaAs surface passivation with sodium and ammonium sulfide solutions," *Physics of the Solid State*, vol. 39, pp. 54-7, 1997.

[84] W. S. Hobson, U. Mohideen, S. J. Pearton, R. E. Slusher, and F. Ren, "SiN/sub x//sulphide passivated GaAs-AlGaAs microdisk lasers," *Electronics Letters*, vol. 29, pp. 2199-200, 1993.

[85] W. S. Hobson, F. Ren, U. Mohideen, R. E. Slusher, M. Lamont Schnoes, and S. J. Pearton, "Silicon nitride encapsulation of sulfide passivated GaAs/AlGaAs microdisk lasers," *Journal of Vacuum Science & Technology A (Vacuum, Surfaces, and Films)*, vol. 13, pp. 642-5, 1995.

[86] V. N. Bessolov and M. V. Lebedev, "Chalcogenide passivation of III-V semiconductor surfaces," *Semiconductors*, vol. 32, pp. 1141-56, 1998.

[87] F. Jia-Fa, H. Oigawa, and Y. Nannichi, "The effect of (NH/sub 4/)/sub 2/S treatment on the interface characteristics of GaAs MIS structures," *Japanese Journal of Applied Physics, Part 2 (Letters)*, vol. 27, pp. 1331-3, 1988.

[88] D. Liu, T. Zhang, R. A. LaRue, J. S. Harris, Jr., and T. W. Sigmon, "Deep level transient spectroscopy study of GaAs surface states treated with inorganic sulfides," *Applied Physics Letters*, vol. 53, pp. 1059-61, 1988.

[89] T. Ohno and K. Shiraishi, "First-principles study of sulfur passivation of GaAs(001) surfaces," *Physical Review B (Condensed Matter)*, vol. 42, pp. 11194-7, 1990.

[90] R. Shang-Fen and C. Yia-Chung, "Electronic properties of sulfur-treated GaAs (001) surfaces," *Physical Review B (Condensed Matter)*, vol. 41, pp. 7705-12, 1990.

[91] I. K. Han, D. H. Woo, H. J. Kim, E. K. Kim, J. I. Lee, S. H. Kim, K. N. Kang, H. Lim, and H. L. Park, "Thermal stability of sulfur-treated InP investigated by photoluminescence," *Journal of Applied Physics*, vol. 80, pp. 4052-7, 1996.

[92] W. D. Chen, X. Q. Li, L. H. Duan, X. L. Xie, and Y. D. Cui, "Photoluminescence enhancement of (NH/sub 4/)/sub 2/S/sub x/ passivated InP surface by rapid thermal annealing," *Applied Surface Science*, vol. 100-101, 1996.

[93] S. R. Lunt, G. N. Ryba, P. G. Santangelo, and N. S. Lewis, "Chemical studies of the passivation of GaAs surface recombination using sulfides and thiols," *Journal of Applied Physics*, vol. 70, pp. 7449-67, 1991.

[94] V. Swaminathan, J. M. Freund, L. M. F. Chirovsky, T. D. Harris, N. A. Kuebler, and L. A. D'Asaro, "Evidence for surface recombination at mesa sidewalls of self-electro-optic effect devices," *Journal of Applied Physics*, vol. 68, pp. 4116-18, 1990.

[95] L. Jastrzebski, J. Lagowski, and H. C. Gatos, "Application of scanning electron microscopy to determination of surface recombination velocity: GaAs," *Applied Physics Letters*, vol. 27, pp. 537-9, 1975.

[96] T. Baba, K. Inoshita, H. Tanaka, J. Yonekura, M. Ariga, A. Matsutani, T. Miyamoto, F. Koyama, and K. Iga, "Strong enhancement of light extraction efficiency in GaInAsP 2-D-arranged microcolumns," *Journal of Lightwave Technology*, vol. 17, pp. 2113-20, 1999.

[97] S. Y. Hu, S. W. Corzine, K. K. Law, D. B. Young, A. C. Gossard, L. A. Coldren, and J. L. Merz, "Lateral carrier diffusion and surface recombination in InGaAs/AlGaAs quantum-well ridge-waveguide lasers," *Journal of Applied Physics*, vol. 76, pp. 4479-87, 1994.

[98] T. A. Ibrahim, K. Amarnath, L. C. Kuo, R. Grover, V. Van, and P.-T. Ho, "Photonic logic NOR gate based on two symmetric microring resonators," *Optics Letters*, vol. 29, pp. 2779-81, 2004.

[99] S. W. Corzine, R.-H. Yan, and L. A. Coldren, "Optical Gain in III-V Bulk and Quantum Well Semiconductors," in *Quantum Well Lasers*, *Quantum Electronics - Principles and Applications*, P. S. Zory, Ed.: Academic Press, 1993.

[100] W. Pascher and R. Pregla, "Vectorial analysis of bends in optical strip waveguides by the method of lines," *Radio Science*, vol. 28, pp. 1229-33, 1993.

[101] D. C. Hutchings, M. Sheik-Bahae, D. J. Hagan, and E. W. van Stryland, "Kramers-Kronig relations in nonlinear optics," *Optical and Quantum Electronics*, vol. 24, pp. 1-30, 1992.

[102] J. P. Weber, "Optimization of the carrier-induced effective index change in InGaAsP waveguides-application to tunable Bragg filters," *IEEE Journal of Quantum Electronics*, vol. 30, pp. 1801-16, 1994.

[103] F. G. Della Corte, G. Cocorullo, M. Iodice, and I. Rendina, "Temperature dependence of the thermo-optic coefficient of InP, GaAs, and SiC from room temperature to 600 K at the wavelength of 1.5 μm," *Applied Physics Letters*, vol. 77, pp. 1614-16, 2000.

[104] H. Chuan, M. Kiene, and P. S. Ho, "Thermal conductivity and interfacial thermal resistance of polymeric low k films," *Applied Physics Letters*, vol. 79, pp. 4121-3, 2001.

[105] E. Gini and H. Melchior, "Thermal dependence of the refractive index of InP measured with integrated optical demultiplexer," *Journal of Applied Physics*, vol. 79, pp. 4335-7, 1996.

[106] M. A. Schmidt, "Wafer-to-wafer bonding for microstructure formation,"

Proceedings of the IEEE, vol. 86, pp. 1575-85, 1998.
[107] J. F. Shackelford and W. Alexander, *CRC Material Science and Engineering Handbook*, 3rd ed: CRC Press, 2001.
[108] C. C. Lee, C. Y. Wang, and G. S. Matijasevic, "A new bonding technology using gold and tin multilayer composite structures," *IEEE Transactions on Components, Hybrids, and Manufacturing Technology*, vol. 14, pp. 407-12, 1991.
[109] H. Z. Wu, X. M. Fang, R. Salas, D. McAlister, and P. J. McCann, "Transfer of PbSe/PbEuSe epilayers grown by MBE on BaF/sub 2/-coated Si(111)," *Thin Solid Films*, vol. 352, pp. 278-82, 1999.
[110] W.-Y. Chen, V. Van, T. N. Ding, M. Du, W. N. Herman, and P.-T. Ho, "Benzocyclobutene Negative-Gap Micro-Ring Notch Filters," presented at Frontiers in Optics 2005 / Laser Science XXI, Tucson, AZ, 2005.
[111] L. B. Soldano, F. B. Veerman, M. K. Smit, B. H. Verbeek, A. H. Dubost, and E. C. M. Pennings, "Planar monomode optical couplers based on multimode interference effects," *Journal of Lightwave Technology*, vol. 10, pp. 1843-50, 1992.
[112] Apollo Photonics Solutions Suite, Apollo Photonics, www.apollophotonics.com
[113] M. J. Adams, H. J. Westlake, M. J. O'Mahony, and I. D. Henning, "A comparison of active and passive optical bistability in semiconductors," *IEEE Journal of Quantum Electronics*, vol. QE-21, pp. 1498-504, 1985.
[114] A. F. J. Levi, R. E. Slusher, S. L. McCall, T. Tanbun-Ek, D. L. Coblentz, and S. J. Pearton, "Electrically pumped, room-temperature microdisk semiconductor lasers with submilliampere threshold currents," *IEEE Transactions on Electron Devices*, vol. 39, pp. 2651, 1992.